Investigations of InAsP/InP Semiconductor Devices for Quantum Communication Technologies

by

Alexander Bogan

A thesis
presented to the University of Waterloo
in fulfillment of the
thesis requirement for the degree of
Master of Science
in
Physics

Waterloo, Ontario, Canada, 2014

This thesis consists of material all of which I authored or co-authored: see Statement of Contributions included in the thesis.

This is a true copy of the thesis, including any required final revisions, as accepted by my examiners.

I understand that my thesis may be made electronically available to the public.

Statement of Contributions

The research described in this thesis was conducted under the co-supervision of Professors Sergei Studenikin and Jan Kycia. The facilities and equipment necessary for the low-temperature research were contributed by the National Research Council of Canada (NRC).

Chapters 2 through 6 of this thesis primarily constitute a literature review of relevant theory of semiconductor quantum dots, electron spin qubits, and techniques which have been proposed or proven in concept for quantum communication. They should not be mistaken for original research. Chapter 2 does, however, include a model of a chain of quantum repeaters, which I developed myself. The simulation codes of quantum well structures used to generate the results of chapter 7 were written by Geof Aers of the NRC, though I ran the programs with my own inputs to generate the results in that chapter. The CBE nanotemplated nanowire technology has been a work in progress at the NRC since before my arrival, but all of the iterative testing discussed in section 8 was performed by myself. The experiments of section 9 and onward were performed by myself, with assistance from Sergei Studenikin, Andy Sachrajda, and Piotr Zawadzki of NRC. The MIRO data of chapter 13 was collected by myself and analysed both by myself and by Anthony Hatke and Professor Michael Zudov of the University of Minnesota. The results presented in chapter 13 have since been published elsewhere[5, 6], as has a technique for enhanced spin qubit readout in double quantum dots which emerged from experiments in which I participated[55].

Abstract

This thesis presents a set of magnetotransport experiments which explore the advantages of InAsP/InP quantum well material and quantum dot structures for spin/photon devices, with a view towards quantum communication. The primary motivation is the development of a solid state quantum repeater, which will enable a secure worldwide quantum internet.

Sections 1-6 review theoretical background relevant to an understanding of the experiments and the hybrid spin-photon devices which may enable the realization of scalable quantum communication over global distances. They provide simple introductory reviews of quantum dot and spin qubit physics, as well as specialized techniques such as Bell measurement and g-factor engineering, highlighting what is relevant to motivating and understanding the experiments described in later sections. The necessary properties of a hybrid spin/photon device are discussed.

Section 7 predicts the effectiveness of several techniques for the engineering of g-factors for the spin-qubit part of these devices. Section 8 presents the novel device structure which was developed and evaluated as a platform for supporting scalable and optically active spin qubit arrays. The required properties of a hybrid device can be met, in theory.

Sections 9-13 present the experiments which were performed to evaluate the InAsP material system for quantum dot applications, the nanowire ridge devices described in section 8, and the side-effects of magnetic fields typically applied to a 2DEG as part of any spin qubit experiment. Magnetic fields are found to noticeably influence scattering effects in a high mobility 2DEG, even at modest fields. The formation of quantum dots in both InGaAs and InAsP nanowires is observed.

Acknowledgement

I have had the privilege to work with many excellent people in my time at the University of Waterloo and the National Research Council of Canada. Many have made a contribution to my edification and well being, and all have directly or indirectly assisted me in the research described in this thesis. All are a credit to the species.

First, I would like to express gratitude to my supervising professors: Sergei Studenikin and Jan Kycia. Both of you consistently impress with the wealth of practical knowledge you have accumulated. In particular, I must thank Jan for introducing me to the exciting world of low-temperature physics and quantum information.

Sergei, I thank you for the guidance and the trust you place in me with your expensive ~~toys~~ scientific equipment. I hope we can continue to ~~play~~ conduct serious scientific research in the future.

Ghislain Granger, Louis Gaudreau, Joelle Thorgrimson, and Gabriel Poulin-Lamarre, I thank you for your frequent help and for the social atmosphere you contributed to the lab in your own ways. Ghislain, in particular, I must thank for showing me the ropes in the early days.

I would like to warmly thank Piotr Zawadzki. I'm sure it would not have been possible to accomplish anything at all without you. Your mechanical and cryogenic acumen are a tremendous asset to the lab, as are your dedication to doing things right the first time. Our constant debate and discussion of current events is not just entertaining, but encourages me to question everything that seems obvious within the lab (and without). This, I think, is how one should learn the subtleties of a craft.

Further thanks go to Guy Austing, Marek Korkusinki, Geoff Aers, Robin Williams, and Andrew Sachrajda for stimulating discussion of papers, without which I would have a diminished perspective on the field of quantum information and spin qubits. Andy, you are one of those people that other people want to pretend that they are: intelligent, polite, humble, honest, and fair. You bring balance to the force.

In the device fabrication group, three individuals have been critical to the success of this research: Alicia Kam, Pedro Barrios, and Phillip Poole. I thank you all for your respective parts in the fabrication of the samples of I have been using these past few years.

Dan Dalucu also generously donated some of his time and energy to introduce me to the basics of photoluminescence measurements. These sessions were “illuminating”, and it seems likely that I will use these techniques in the future. Many thanks!

The financial support of NSERC and NRC was essential in keeping me well fed, warm, and in good health while conducting this research. Without access to the NRC’s facilities, this work would not have been possible.

Honourable mentions go out to my parents, Sandra and Michael Bogan, who made the minor contribution of creating, raising, and supporting me.

Dedicated to Kira Sfiligoi and my parents, Sandra and Michael.

Contents

List of Figures

List of Publications and Presentations

[1] Bogan, A., Aers, G., Studenikin, S. A., and Sachrajda, A. (2013a). Electrical manipulation of electron g-factor in solid state spin qubits for quantum repeater applications. Presented at the 10th annual Canadian Quantum Information Students' Conference in Calgary, Alberta.

[2] Bogan, A., Hatke, A. T., Studenikin, S. A., Sachrajda, A., and Zudov, M. A. (2012a). Damped microwave induced resistivity oscillations in a tilted magnetic field. Presented at the 20th International Conference on High Magnetic Fields in Semiconductor Physics in Chamonix Mont-Blanc, France.

[3] Bogan, A., Hatke, A. T., Studenikin, S. A., Sachrajda, A., Zudov, M. A., Pfeiffer, L. N., and West, K. W. (2012b). Microwave-induced resistance oscillations in tilted magnetic fields. Phys. Rev. B, 86:235305.

[4] Bogan, A., Hatke, A. T., Studenikin, S. A., Sachrajda, A., Zudov, M. A., Pfeiffer, L. N., and West, K. W. (2013b). Effect of an in-plane magnetic field on microwave photoresistance and shubnikov-de haas effect in high-mobility gaas/algaas quantum wells. Journal of Physics: Conference Series, 456(1):012004.

[5] Studenikin, S. A., Thorgrimson, J., Aers, G. C., Kam, A., Zawadzki, P., Wasilewski, Z. R., Bogan, A., and Sachrajda, A. S. (2012). Enhanced charge detection of spin qubit readout via an intermediate state. Applied Physics Letters, 101(23):233101.

Chapter 1

Introduction

Quantum information science is a modern field of research, combining elements of computer science and quantum physics to solve problems relevant in today's world. While the notions of simulating molecular interactions, searching huge databases, or breaking popular classical encryption schemes are attractive applications, there is comparatively impactful low-hanging fruit to be picked.

Quantum Key Distribution (QKD) is a technology that has been demonstrated over short distances, but has yet to achieve mainstream adoption due to restricted effective distances. The technology provides provable physical security, rather than relying on the unproven but practically reliable hardness of certain numerical calculations, such as discrete logarithms or the factorization of large numbers. Since these calculations can be performed economically with a quantum computer, QKD and symmetric key algorithms (such as the provably secure one-time pad algorithm) are especially attractive to those who seek long-term security for their data.

In order to extend the range of QKD networks and quantum communication in general, low-loss long-distance quantum communication channels must be created. Such channels can be created by making use of a device called a quantum repeater, which concatenates multiple somewhat reliable short range links to create a single arbitrarily reliable long-range link. The basics of the quantum repeater will be reviewed here in the first section, and it will be broken up into component challenges which are physically interesting.

Matter-based qubits, and in particular spin qubits in quantum dots, offer significant advantages over the all-optical quantum communication schemes.

With the help of a simple performance model, we shall see that a hybrid spin and photon-based system, with heralded memory and memory-integrated Bell measurement, offers a dramatic improvement to the scaling of the transmission rate as a function of distance. The pursuit of either spin-based memory and Bell measurement hardware or else a system with equivalent properties will be shown to be very important for the establishment of a useful global-scale quantum internet.

A scheme has been proven in principle to convert quantum information from photonic qubits into spin qubits[34], and another has been proposed to perform full Bell measurement[61] on them once converted, both of which are essential aspects of the hybrid spin and photon quantum repeater. In order to realize each of these schemes, spin qubits must be engineered with particular g-factor values. Specifically, finely tuned electron g-factors near zero must be attainable. Why and how these conditions can be engineered will be discussed, and theoretical predictions for a potential solution will be presented.

Arbitrarily scalable quantum dot arrays can in principle be constructed from nanowires with a relatively small number of gate electrodes, with comparison to lateral quantum dots. Evaluation of the fabrication of templated nanowires fabricated at NRC via Chemical Beam Epitaxy (CBE) have informed refinements to increase device yield. These devices may one day find use as arrays of receivers for photonic qubits in a quantum repeater, or as registers in a quantum processor.

In addition to these refinements, quantum dots were formed in such a nano-templated nanowire (made of InGaAs) and in a laterally gated 2DEG sample (InAsP quantum well). In both cases, it appeared that unexpected random potential fluctuations in space support tightly confined quantum dots, responsible for transport features that are visible well above 1 Kelvin.

Lastly, Microwave Induced Resistivity Oscillations were employed as a probe of scattering effects in a high-mobility GaAs 2DEG, revealing that a dominant increase in the single particle scattering time, τ_q, can result from the application of in-plane magnetic fields well within the range typically employed for the operation of spin qubits.

Chapter 2

Quantum Key Distribution (QKD) with Heralded Memory and Integrated Bell Measurement

2.1 Bell Entanglement: Quantum Correlations

The Bell states are a set of four mutually-orthogonal states which are defined for two-qubits. In terms of a qubit basis of orthonormal states $|0>$ and $|1>$, the states are written as below:

$$
\begin{array}{ll}
|\Phi^+> = \frac{1}{\sqrt{2}}(|00> + |11>) & |\Phi^-> = \frac{1}{\sqrt{2}}(|00> - |11>) \\
|\Psi^+> = \frac{1}{\sqrt{2}}(|01> + |10>) & |\Psi^-> = \frac{1}{\sqrt{2}}(|01> - |10>)
\end{array}
$$

The Bell states have a number of interesting properties. They differ from one another by single Pauli operators applied to either qubit. This makes the preparation of a particular Bell state a simple matter given any other Bell state and the ability to perform local manipulations on qubits. For example:

State	X_1 vs X_2	Z_1 vs Z_2	X_1 vs Z_2
$\|\Psi^+>$	Opposite	Same	Unrelated
$\|\Psi^->$	Opposite	Opposite	Unrelated
$\|\Phi^+>$	Same	Same	Unrelated
$\|\Psi^->$	Same	Opposite	Unrelated

Table 2.1: Correlations between measurements on different qubits of various Bell states.

$$\begin{aligned}
\tfrac{1}{\sqrt{2}}(|01> - |10>) &= \quad (I \otimes I)\tfrac{1}{\sqrt{2}}(|01> - |10>) \\
\tfrac{1}{\sqrt{2}}(|01> - |10>) &= \quad (I \otimes X)\tfrac{1}{\sqrt{2}}(|00> - |11>) \\
\tfrac{1}{\sqrt{2}}(|01> - |10>) &= \; -(I \otimes Z)\tfrac{1}{\sqrt{2}}(|01> + |10>) \\
\tfrac{1}{\sqrt{2}}(|01> - |10>) &= \; (I \otimes ZX)\tfrac{1}{\sqrt{2}}(|00> + |11>) = i(I \otimes Y)\tfrac{1}{\sqrt{2}}(|00> + |11>)
\end{aligned}$$

The rest of the relationships can be easily derived by the product rules for pauli operators ($iX = YZ$, $iY = ZX$, $iZ = XY$).

The outcome of any projective single-qubit measurement U on either qubit of the $|\Psi^->$ state must leave the other qubit in the opposite state. In particular, this will be true of single-qubit Pauli measurements in the X and Z directions. The proof of this can be found in appendix B.

Combining the above relationship with this basic property of the $|\Psi^->$ state, correlations can be found in the outcomes of all pairs of Pauli measurements performed on each qubit. Important cases are shown in table 2.1. For example, measurement of both qubits in the X or Z basis will always yield the two opposite outcomes (though which qubit yields which state is uncertain). On the other hand, measuring one qubit in X and the other in Z will yield two completely random results.

On the other hand, orthogonal Pauli measurements performed on different qubits will always give fully uncorrelated outcomes.

These properties are framed in terms of measurements, but of course ideal measurements produce pure states as outputs. Each individual qubit of the system is maximally uncertain (mixed) on its own, but its state is fully correlated with the other state after a fully projective measurement of either qubit. Precisely, the reduced density operator of each qubit is the maximally mixed state $\frac{1}{2}I$ before measurement, but a single qubit measurement on just half of the state always produces a (random) separable pure state of two qubits.

A Bell state can therefore be intuitively understood as a state of maximum information about the difference between two qubits after a single-qubit measurement, contrasted with a separable state which encodes maximum information about the outcomes of two particular single-qubit measurements (one on each qubit).

2.2 Quantum Key Distribution: Using Correlations to Produce Cryptographic Keys

A classically correlated system such as a pair of coins can be used to transmit information securely between two parties, for example Alice and Bob. Suppose Alice flips two coins and compares them. They are either the same (heads/heads, tails/tails) or different (heads/tails, tails/heads). If Alice can securely transfer one of these coins to Bob, then Alice can publicly tell Bob whether his coin is the same or different compared with hers. Since Bob knows the face of his coin, he can deduce the face of Alice's coin. Information is transmitted. Lacking Bob's coin, however, any eavesdropper would be lost. There is no way to deduce the value of either coin knowing only that they are the same or different.

Of course, in this classical algorithm, the information transfered is only as secure as the coins. The coins play the role of a "cryptographic key", and must be kept secure.

In principle, the quantum correlations which we call entanglement are stronger than any classical correlations. John Bell quantified these classically forbidden correlations in a landmark paper[2]. The possibility of stronger-than-classical correlations unlocks a number of interesting features of quantum communication. The process known as Quantum Key Distribution (QKD) establishes mutual secret keys like the classical coins. Fundamentally, QKD is simply the conversion of quantum correlations into classical ones and finally into secret keys. Quantum correlations are preferable to the classical variety, because quantum states are protected from being copied by the no-cloning theorem[59].

In this frame of thought, the Ekert protocol for QKD is simpler to understand[18]. Ekert's original protocol involved three basis states and used Bell's theorem to confirm the security of the channel. A simplified two-basis algorithm is shown below:

1. Alice prepares an entangled state of two qubits which is in one of the Bell states.
2. Alice sends one of these qubits over a quantum channel to Bob. Bob knows which Bell state he is receiving (Alice tells him publicly).
3. Alice chooses randomly between the X and Z basis, and performs a measurement of her qubit in that basis.
4. Bob similarly chooses a random basis and performs a measurement.
5. Alice and Bob discuss their chosen bases over a (public) classical channel. The bases are randomly chosen before measurement, and necessarily reveal nothing about the outcomes of the measurements.
6. If Alice and Bob randomly chose the same basis (50% of the time), their measurement results were correlated.
7. Alice uses her measurement as a bit of key. Bob predicts Alice's measurement based on his own, and uses that as a bit of key. If no errors occur, they produce identical bits of key by this process.
8. Alice and Bob repeat until they have a sufficiently long key for their purposes, which may be to encrypt a message for transmission.
9. The key can then be used for classical encryption, including the provably secure one time pad algorithm.

As the classical channel is only used to discuss random basis choices, it contains no information. The quantum channel always transmits the same Bell state, and so holds no information. If the quantum channel is intercepted by an eavesdropper (Eve), she cannot make use of the entanglement without (detectably) degrading the quality of the state Bob receives. Specifically, attempts to copy or weakly measure the state of the channel will detectably corrupt the generated key. Alice and Bob can use a technique called classical privacy amplification to remove corruptions due to errors and eavesdropping and simultaneously dilute any partial information Eve may have obtained

Alice's Basis	Alice's Measurement	Bob's Basis	Bob's Measurement	Key
Z	1	X	1	
Z	1	Z	0	1
X	0	X	1	0
X	0	Z	1	
Z	0	Z	1	0
X	1	Z	1	
X	1	X	0	1

Table 2.2: Alice and Bob share many copies of $|\Psi^{-}>$*. Over many rounds of the Ekert protocol, they establish a shared random key.*

about the key[4]. For the interested, appendix C gives details and an example of a privacy amplification algorithm. Part of the privacy amplification process involves detecting whether two keys are the same without directly comparing them, and so Alice and Bob can build confidence that their keys are not corrupt if privacy amplification succeeds[4]. Two non-identical keys cannot correctly encrypt and decrypt messages. Therefore, in the case that the keys are corrupted, Alice and Bob will be able to detect the corruption by their failure to communicate.

2.3 QKD Over Imperfect Quantum Channels

Communication takes place through channels. In the previous section, we assumed Alice and Bob had access to a perfect quantum channel and that they could reliably distribute pure entangled states. In reality there is always a certain amount of error and imperfection, even in classical communication.

Generally, the state transmitted through an imperfect channel will be a mixed state of lesser purity than the input state. The effect of attempting the QKD protocol with imperfect states is that errors will be introduced into the secret key. If Alice and Bob have different encryption keys, a message encoded by Alice will be indecipherable to Bob. Alice and Bob can, however, use privacy amplification techniques to create shorter identical keys from longer keys with errors[10].

The effects of errors in the quantum channel are therefore to reduce the rate at which keys are generated. Unfortunately, there is a limit up to which this technique will work. Above this threshold, the certainty that an evesdropper has insufficient information to reconstruct the key is lost. The QKD schemes with the highest theoretical thresholds are in the 20% bit error range, with the highest error tolerance threshold known at the time of writing being 27.6%[10].

Errors in communication channels come in two forms. The first are in the form of corruptions, where bits and qubits are modified from their intended values. In transit, 0 becomes 1 or $|0\rangle + |1\rangle$ becomes $|0\rangle - |1\rangle$ for example. The detection and correction of these types of errors is the domain of quantum error correction research. As discussed earlier, corruption errors can be safely dealt with up to to large threshold in the context of quantum key distribution.

The second type of error is an insertion error. This affects sequences of bits and qubits. In principle a detector can trigger when no signal is present, resulting in a phantom bit of information arriving when none was sent. These errors are relatively simple to defend against using timing information. If no qubit was expected, the qubit can be discarded. If the qubit replaces the intended qubit, it can be interpreted as a corruption and dealt with as such.

Deletion errors are also easy to detect. Bits and qubits which were sent simply do not arrive, and are not processed.

Unfortunately, the ability to detect and correct errors is only so useful. In particular, when sending quantum information over long distances encoded in photon states, photon loss can result in deletion errors. These errors are easy to detect, but if they dominate, the rate at which qubits are transmitted will shrink rapidly. Furthermore, since quantum information cannot be copied, qubits are precious. A qubit can be said to "cost" exactly as much as the computation it took to create it. Losing qubits that are part of a distributed quantum computation, for example, is not desirable.

The problem of losing precious qubits can be mitigated if necessary by quantum teleportation. The algorithm makes use of classical communication and pre-established shared entanglement between two nodes to transfer a quantum state without risking qubit loss. While the payload qubit is considered "precious", the entangled qubits are assumed to be simple to prepare (i.e. not the result of lengthy calculations). Their loss is therefore tolerable. By sacrificing many entangled qubits, the payload qubit can be transmitted with confidence. This allows two parties to effectively establish a lossless quantum channel from a lossy one with the help of a classical communication channel[3].

The problem of creating a lossless long-range quantum channel therefore reduces to the problem of quickly transmitting many qubits over long distances and with high fidelity, which is the purpose of the quantum repeater.

2.4 The Quantum Repeater

In quantum communication experiments, entanglement has been established over a distance of 143 km at rates of about 100 qubits per hour[41]. In order to establish a global secure quantum internet with reasonable throughput, quantum keys must be distributable over a distance of 20000 kilometers: the half-circumference of the Earth. However, there exists a conceptual device[8, 66], proved in experiment[62], which combines many short links into one long link.

The goal of a quantum repeater is to establish long-distance entanglement using short-distance entanglement that is more easily established.

The probability that a particular photon will be transmitted through an optical fiber is exponential in the length of the fiber:

$$P(\text{transmission}) = exp(-L/L_0) \tag{2.1}$$

where L_0 is the absorption length of the fiber, typically 10 km or so for telecom optical fibers at 1550 nm wavelength. For links of order L_0 length, the probability that transmission will succeed is high.

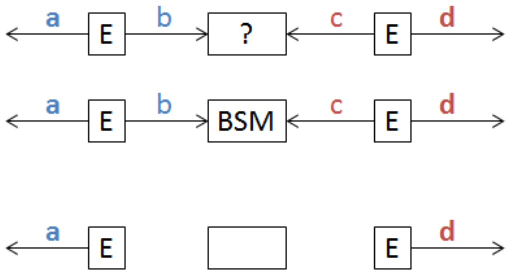

(a) $(|00> + |11>)(|00> + |11>)$

(b) $|0000> + |0011> + |1100> + |1111>$

(c) Outcome $|xy> \pm |\bar{x}\bar{y}>$ *for the b and c qubits yields* $|xy> \pm |\bar{x}\bar{y}>$ *for the a and d qubits. a and d are now entangled.*

Figure 2.1: The entanglement swapping algorithm. The bolding and colour of the qubits matches between the diagram and the captions, like so: $|\mathbf{a}bc\mathbf{d}>$. *Two pairs of entangled qubits are generated and separated at the emitter (E). Two qubits, one from each pair, are compared in a Bell analyzer (BSM, center node), revealing the entanglement between the two remaining qubits.* $\bar{x}$ *is the complement of* x *(*$\bar{0} = 1$ *and* $\bar{1} = 0$*).*

The operation of the quantum repeater is shown in figure 2.1. Four photonic qubits are prepared in the form of two entangled pairs, with each pair initially some distance apart. Bell state Emitters (E) generate the entangled photon pairs. One photon from each pair is physically transported to the Bell State Measurement (BSM) node, where a projective Bell measurement of the two qubits reveals their respective entanglement. After the measurement of the two qubits localized at the BSM node, the peripheral qubits (a and d in figure 2.1) are entangled. There are many ways of understanding this outcome, such as by interpreting an entangled state as a state of maximum information about the differences between qubits (seesection 2.1) and the Bell measurement as a projective measurement of the non-local state into one of four possible differences.

Role of Quantum Memory

As we have seen in figure 2.1, short entanglement links can be concatenated into a single long link. Unfortunately, the probability that N short links of length L can be established simultaneously is equal to the probability that one long link of length NL can be established. This is due to the fact that the probabilities of individual successes are exponential in L (equation 2.1), as well as the fact that the total probability is the product of N individual probabilities (exponential, therefore, in NL). Therefore, naively attempting to concatenate N links together will not increase the probability of transmitting a single qubit.

Fortunately, any given short link is increasingly likely to transmit successfully over many attempts. If qubits can be stored for some time in a quantum memory, several rounds of transmission attempts can be made until every link has been established. This translates into better than exponential decay in transmission rate with distance and therefore a more scaleable quantum network.

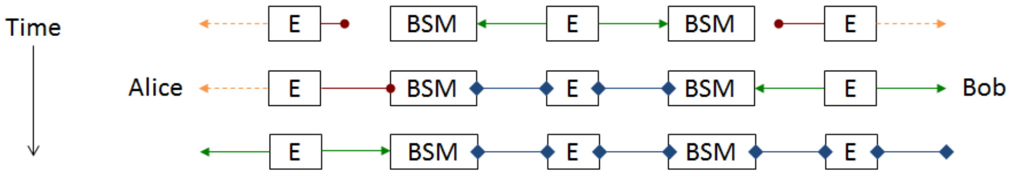

Figure 2.2: Establishing entanglement. (E)mitter nodes generate entangled pairs and send one photon to each neighboring Bell State Measurement (BSM) node. When a photon fails to arrive or fails to enter the quantum memory (red, circle) its partner photon (orange, dashed) is discarded. Successfully transmitted qubits (green, arrow) are saved for the next round in quantum memory at the BSM nodes (blue, diamond). Eventually, all emitter nodes have spread entanglement to their neighbours and entanglement swapping can begin.

2.5 Optical Repeaters

Optical quantum repeater experiments have been successfully demonstrated, proving the concept of the quantum repeater[63]. Unfortunately, entangling photonic qubits is difficult. In the linear optical regime, full Bell basis measurement is provably impossible[33, 40]. This is true not only because photons are difficult to entangle, but also because projective detections of photons are generally destructive with current technology.

A scheme making use of interference of two photons in beam splitters allows partial Bell measurement that can distinguish up to two of the four Bell states, destroying both photons in the process and leaving the measurement ambiguous between the remaining two Bell states. When measuring arbitrary or fully mixed qubits with passive linear optical components, the measurement must succeed at most 50% of the time[65].

An alternative scheme exists whereby arbitrarily high Bell measurement success rates can be achieved, approaching unity as infinite resources become available, in the form of beam splitters and single photon detectors[24]. Additional detectors and precisely timed sources of entangled photons are needed. However, to achieve a success rate of $1 - 1/2^N$, $2^N - 1$ pairs of entangled photons must be made to interact in an increasingly complex system of beam splitters and polarizing beam splitters with many detectors. The complicated setup increases both the cost and the frequency of errors in the measurement, as well as space requirements.

A second obstacle for all-optical quantum repeaters is the challenge of non-destructively detecting the arrival of qubits at the BSM nodes. A critical aspect of the entanglement distribution step of the entanglement swapping protocol (figure 2.1) is that photons must be detected to have arrived and been loaded into the quantum memories before the swapping can begin. Some quantum memories, such as atomic ensemble quantum memories, do not offer this "heralding". They silently attempt to store photons whether they arrive or not, occasionally failing to absorb or re-emit the photons. While high-efficiency memories might be feasible, lower efficiencies (¡90%) are tolerable if heralding is present (see section 2.7).

Consider the general quantum repeater scheme:

1. Emitters generate entangled photons in pairs.
2. Photons travel long distances from their points of origin to neighboring Bell measurement nodes.
3. Quantum memories at the measurement nodes store the information contained in the arriving photons and report their arrival.
4. If a photon failed to arrive on either side, the measurement node reports failure and waits for another photon.
5. At this point, which corresponds to final conditions of figure 2.2, a full complement of input photons has been received by each node (one from each neighbor). Each BSM node now performs a Bell measurement and makes the result known to the end-points of the channel (Alice and Bob).
6. Alice and Bob's qubits are entangled in a known fashion depending on the results of local measurements at each of the Bell measurement nodes.

All-optical quantum repeaters suffer in step 3, because it is challenging to build quantum memories that can efficiently store, emit, and herald the arrival of photons without collapsing the qubit state. Atomic ensemble memories, for example, are optimized for storage and retrieval efficiency. Heralding, on the other hand, is all but impossible[52] in these systems.

In the next section we model a general optical quantum repeater and predict its performance, showing that the optical quantum repeater's throughput

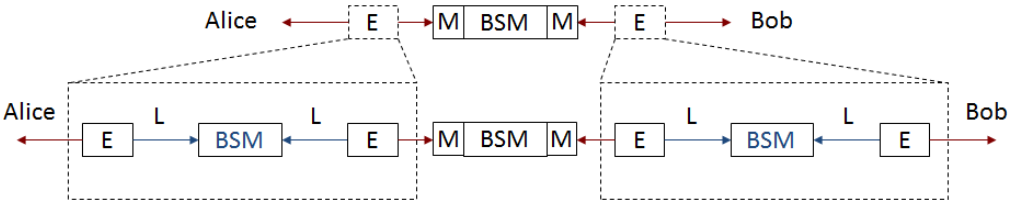

Figure 2.3: Quantum repeater scheme (top) with pseudo-heralded distribution of photons (bottom). The scheme makes use of two types of Bell State Measurement node (BSM): one with and one without quantum memories (M). Each emitter distributes one photon along a short link (which is unlikely to absorb the photon) to a quantum memory, and the other to the memory-less BSM along a long link of length L. Upon a successful Bell measurement of two photons at each memory-less BSM, the other photons are assumed to have reached the quantum memories and been stored. This is equivalent to the top scheme, which is a quantum repeater with heralded entanglement sources, except that each emitter also contributes a length 2L to the total communication length.

scales too poorly with distance to be useful for the formation of a quantum internet, even with nearly optimal storage and retrieval efficiency in quantum memories and the pseudo-heralding scheme of figure 2.3.

2.6 Optical Repeater Performance Model

The performance of an all-optical quantum repeater depends on the rate at which entangled pairs can be generated, but also various measures of imperfection in the device (memory efficiency, Bell measurement node efficiency, link efficiency, etc.). We have used a simple model, which assumes that all of the Bell emitters generate entangled pairs at the same rate, to predict the ultimate performance of a quantum repeater chain of a given total length, with an optimal number of nodes. The transmission probability over each link and the efficiency of both memory operations and Bell measurement is taken into account.

Let's identify the following quantities:

R_e: Rate of Bell pair generation
E_M: Efficiency of Bell basis measurement
E_i: Efficiency of memory (input)
E_o: Efficiency of memory (output)
L_0: Quantum channel's characteristic absorption length
R_t: Rate of transmission
N: The number of direct entanglement distribution links (each of length L)
I: Number of round-trip communication cycles per memory coherence time

The transmission rate over the total distance NL is:

$$R_t = R_e \cdot E_i^{2N} \cdot E_o^{2N} \cdot {E_M}^{2N} \cdot F(N, L/L_0, I) \tag{2.2}$$

So long as the rate of Bell pair generation is less than the rates at which they can be stored, retrieved, and processed, the rate of transmission is proportional to the rate of pair generation (R_e). If a photon is lost from any of the 2N memories, the outcome is failure. The photon inputs to each Bell measurement node are lost, and the process must begin again. For this reason, the rate decays exponentially with the number of memories ($2N$) with a base equal to the memory output efficiency (M_o). Since the all-optical setup lacks heralded memory, a similar term exists with base equal to the memory input efficiency (M_i). Memory efficiency is therefore a critical limitation when heralded memories are unavailable or when memories must emit photons, such as in the all-optical quantum repeater.

Additionally, the distribution of entanglement will fail if even a single Bell module fails to identify the Bell state of its inputs. This is the origin of the factor ${E_M}^{2N}$. The number $2N$ originates from the fact that twice as many measurement nodes are needed to provide the pseudo-heralding from figure 2.3.

Finally, there is a factor, $F(N, L/L_0, I)$, which is a function of the number of links, the length of each link, and the number of attempts the system is permitted to make to establish each link. One method of numerically evaluating this function is presented in appendix A. The transmission rate's dependence on the link length, L, is encapsulated entirely within the function F, which is sub-exponential in L/L_0, compared to the exponential decay behaviour of equation 2.1. This is why the quantum repeater can be an improvement on a direct link between Alice and Bob, in terms of ultimate transmission rate.

The weakness of the all-optical quantum repeater is that if E_M, E_i and E_o are not all unity, the exponential decay in transmission rate as a function of N prevents scaling of the technology to arbitrary distances. Based on a numerical computation, the performance of a family of all-optical quantum repeaters is presented in figure 2.4. Notably, the overall trend in transmission rate as a function of total distance is still exponential falloff, though it may perform better than a direct link. The distance at which it becomes more profitable to use a quantum repeater chain depends on the particular values of the various efficiencies (E_i, E_o, E_m) and the absorption length (L_0), but it is clear from figure 2.4 that a high-performance global direct link is implausible without shattering the wildest expectations of optical fiber technology.

This model assumes a single channel, and multi-channel optical quantum repeaters do fare better. For a model which assumes up to 10000 transmission modes, multi-mode memories, and the ability to combine any two modes in a BSM node, compare with [53]. However, even in this scheme the need to minimize the number of measurement nodes, N, is present due to the limiting failure rate of 50% for every Bell measurement. This leads to an inescapable exponential falloff in transmission rate as a function of N, as well as L. Eliminating this limiting failure rate, we will see, drastically improves the possible transmission rates.

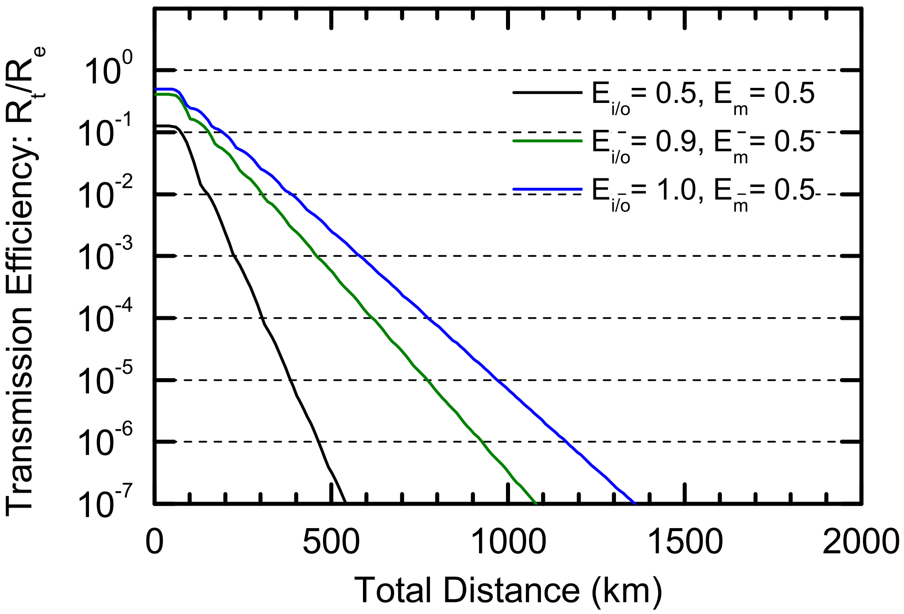

Figure 2.4: Transmission efficiency for all-optical quantum repeater, for various assumed efficiencies of the optical memories ($E_{i/o}$) and 50% efficient Bell measurement (E_m). The model dynamically optimizes the number of links (N) for each value of the total distance, which is the origin of the cusps in the line shape. It is assumed that optical fibers with -0.2dB/km of attenuation are being used to establish the links, and that 50 communication cycles are permitted before the memory's coherence becomes suspect. No heralding is assumed.

2.7 Augmented Repeater with Heralded Memories and Integrated Bell Measurement

The all-optical quantum repeater scheme presented previously dealt with the lack of true heralding in ensemble quantum memories by compensating with highly efficient input and output efficiencies and some clever design which yields some heralding information for the photons which travel the longest distances. However, using quantum dot spin qubits both as memories and as a Bell measurement platform, one can drastically improve the scheme. Coupled quantum dot spin qubits, which will be discussed in sections 3 and 4, can be read out in the Bell basis (section 5), and in principle this can be done without ambiguity between multiple Bell states (as in the optical case). Furthermore, performing Bell basis measurements with the memories directly eliminates the need for the lossy process of converting the memory state back into photons. Spin qubit based quantum memories can even provide heralding by exposing the charge of the qubit (indicating the presence of information) while protecting the information itself (encoded in spin). One can probe the charge of the memory using, for example, standard QPC charge detection techniques to detect the presence of spin information without disturbing it or reading it out.

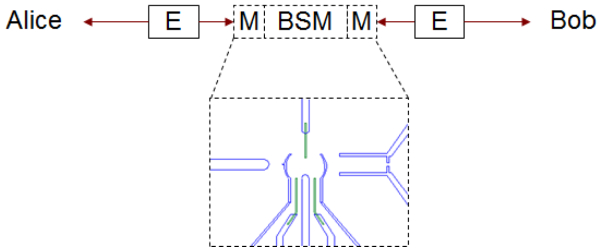

Figure 2.5: A hybrid entanglement swapping scheme, where a particular quantum dot nanostructure serves both as quantum memory and Bell measurement. Memory-integrated measurement eliminates the need for memories to release photons. The inset is a two-dimensional gate layout for a double quantum dot and associated charge detectors, serving in this case as a stand-in for a nano-structure with all of the required capabilities.

Figure 2.5 illustrates how the suggested scheme works. The heralded memories dispense with the need for pseudo-heralded transmission as in the all-optical repeater scheme. Instead, a pair of quantum dots are used as a combination quantum memory and Bell measurement node.

The transmission rate model is similar, but not identical to the all optical scheme:

$$R_t = R_e \cdot {E_M}^N \cdot G(E_i, N, L/L_0, I) \tag{2.3}$$

Since the spin qubit memories need never re-emit photons, their emission efficiency (E_o) is meaningless in this scheme. Furthermore, since the spin qubit memories themselves are heralded, the input efficiency E_i is a parameter to the function "G", which is sub-exponential in all of its arguments (see appendix A).

The only source of exponential decay is from the total Bell measurement efficiency: ${E_M}^N$. Figure 2.6 shows a family of hybrid optical/electronic repeaters, and their performance as a function of distance. The improved scaling translates into the , in principle, access longer distances more comparable with the size of the Earth.

We have seen that the BSM success probability is the principle determining factor of throughput efficiency, especially outside of the all-optical scheme presented here. Unity BSM success probability can be achieved with spin qubits by performing either a single Bell measurement or a series of partial Bell measurements, with the latter becoming possible because spin qubits can be measured without totally destroying the qubits. This is in stark contrast with single-photon detection techniques which destroy the photons.

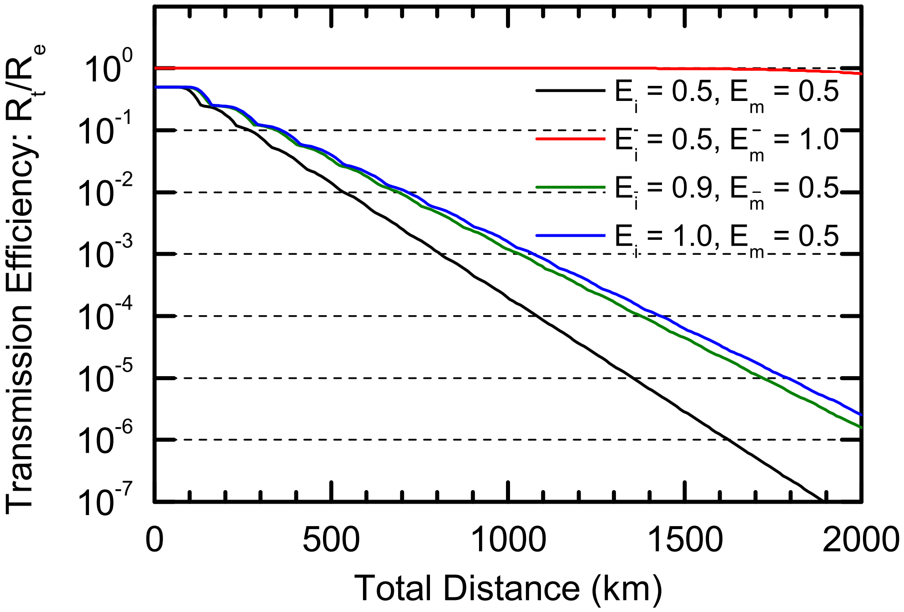

Figure 2.6: Solid state performance model with integrated Bell measurement and heralded memory, for various values of the memory input (E_i) efficiency. With the exception of the orange line at the top, Bell measurement efficiency (E_m was assumed to be 50% to match the assumed efficiencies of figure 2.6 for comparison. The nearly horizontal orange line, corresponding to the additional assumption of ideal Bell measurement ($E_m = 1.0$) is not possible in the all-optical case. An arbitrary limit of $N < 30$ links was eventually reached, which is the origin of the noticable decrease exhibited by the red line once the choice of N is no longer theoretically optimal. The real-world limit to the number of links will depend on the number of logical errors introduced by operations at each node, and is uncertain at this time. -0.2dB/km fiber attenuation, a maximum of 50 communication cycles, and true heralded memories are assumed. N is dynamically optimized for each distance value. It is necessary to allow sufficiently many communication cycles that the establishment of every link occurs with high probability, and this depends on the memory efficiency.

2.8 Summary

- Unlike the all-optical scheme, where Bell measurement must necessarily be done with optical components, a spin-qubit approach permits Bell measurement with a theoretically perfect limiting efficiency.
- As evidenced by figures 2.4 and 2.6, this efficiency is the limiting factor in the development of a quantum network on a global scale.
- Calculations show that whereas the all-optical repeater schemes must rely on very efficient memories, a repeater with heralded memories can tolerate inefficient memories.
- This tolerance can be further enhanced by using memories with longer and longer coherence times, permitting any given repeater node to wait longer for a successful photon transmission from a given neighbor.

The development of a high-efficiency Bell measurement scheme with integrated quantum memory will unlock longer-distance quantum communication, and will enable commercially viable long-distance QKD. The following sections discuss the theory of quantum dots and spin qubits, and will motivate the use of spin qubit devices to supply that functionality.

Chapter 3

Introduction to Quantum Dots

A quantum dot is a confined charge with well-defined orbital quantization. A wide variety of such devices exist in different materials and geometries[11, 29, 57] which can confine both electrons[21] and holes[39]. This section will focus on some of the theory behind quantum dots, with a view towards measuring the size of the quantum dots in question, as well as the effective g-factor of trapped electrons which might be used as part of spin qubits.

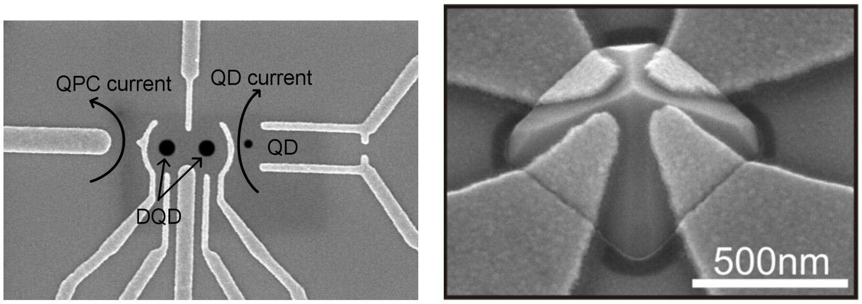

(a) Gated quantum dot in a GaAs 2 Dimensional Electron Gas (2DEG).

(b) Pyramidal quantum dot with four side gates.

Figure 3.1: Scanning electron microscope images of two real-world quantum dot devices.

By introducing leads on either side of a quantum dot, and by engineering tunnelling barriers to those leads from the dot, one can study the charge transport characteristics of the dot (see figure 3.3).

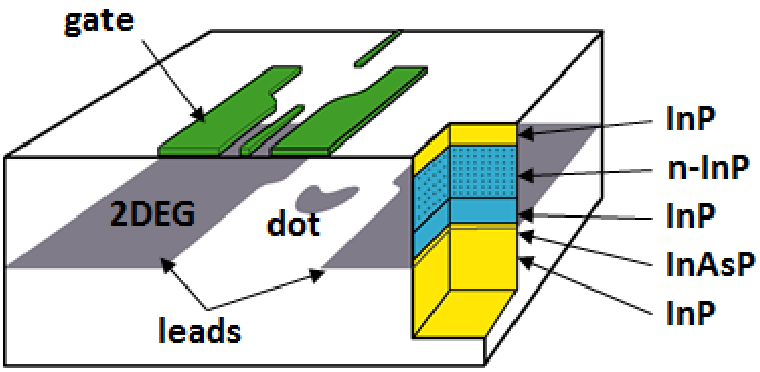

Figure 3.2: Sketch of a lateral gated quantum dot device similar to that of figure 3.1a, showing the gate layer and the depleted regions of 2DEG under the gates. The un-depleted regions are shown in grey, and make up the dot and leads.

Quantum dots can be fabricated in many different material systems and in many different ways. Self-assembled quantum dots form spontaneously during growth and tend to be of high optical quality, but no two self-assembled quantum dots are alike [58]. Gate-defined quantum dots are formed by the action of variable gate voltages, which offers a degree of dynamic control over the confining potential during experiments. Dots can be formed as a cluster of atoms, a single impurity, a semiconductor nanowire, or as two-dimensional etched or gate-defined regions of a quantum well or heterojunction. In the latter case, the quantum dots are called "lateral" quantum dots. Common materials include InAs, GaAs, and InP, as well as ternary alloys such as InGaAs and InAsP.

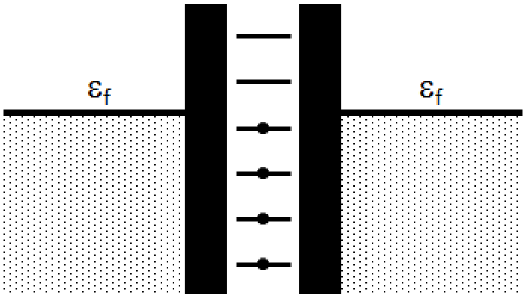

Figure 3.3: Conceptual energy/space diagram of a quantum dot. A confinement potential defines energy levels that can be occupied by electrons. This quantum dot is tunnel-coupled to two leads, one on either side. At sufficienly low temperature, energy levels which are below the Fermi levels of both leads are filled with electrons from both leads, while those which are above both Fermi levels are empty.

3.1 Quantum Dot Constant Interaction Model

Two major forces are especially relevant in quantum dot physics. First, electric repulsion between charges creates an energy spacing between the different charge states of a quantum dot. In small quantum dots, the charging energy (energy associated with adding or removing a single electron) can be significant for single elementary charges. Second, the spatial confinement of charges leads to orbital energy quantization not unlike the energy quantization of atomic orbitals, though the confining potential is defined by geometric and material parameters of the system. It is for this reason that quantum dot structures are often called “artificial atoms”.

Models of the system must take into account these aspects. The simplest model of a quantum dot is the so-called constant interaction model[37], whereby the Hamiltonian of the system is given by

$$H = \frac{(-|e|(N - N_0) + C_S V_S + C_D V_D + C_G V_G)^2}{2C} \tag{3.1}$$

Here, N is the charge counting operator of the quantum dot, and N_0 is the charge induced by dopants and other background charges. C_S and V_S are the capacitance and voltage of the source contact respectively, and similarly with the drain (D) and gate (G) contacts. Finally, C is the total capacitance $C_S + C_D + C_G + ...$ of the system.

The constant interaction model is so named because the electrons are described by single particle eigenstates and a single fixed charging energy for each additional electron in the system. The quantum dot is described by a single constant capacitance C which does not change with gate voltage or charge state. The quantum dot is modelled as a metal disk, the energy of which follows the typical equation for a capacitor: $E = Q/C$. The utility of this model is that, among other things, the size of the quantum dot can be estimated from the capacitance (measured using the techniques ofsection 3.4).

3.2 Coulomb Blockade and Charge Counting

Looking at equation 3.1, notice that it is parabolic in $N - C_G V_G$. Since N is an integer and V_G is a continuous variable, however, an interesting effect emerges. We can see that: $H(N, V_G) = H(N+1, V_G)$ periodically in V_G, for different integer values of N. This condition, where the ground state is degenerate and composed of two different charge states, permits electrons to enter and exit the dot without absorbing or giving up extra energy. This is the condition for the quantum dot to permit the flow of current (see figure 3.4).

This effect, specifically the suppression of current through the dot except at specific periodic values of gate voltage, is called Coulomb blockade. It allows the experimentalist to map out the values of gate voltage at which a new charge state replaces the current ground state, and thus controllably add or remove electrons. Because the gaps between the peaks are caused by Coulomb interactions, and a more tightly confined charge is more strongly interactive, a smaller quantum dot features a larger charging energy.

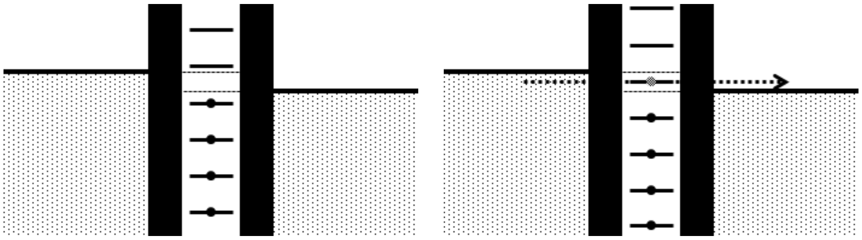

(a) Under bias, one lead has electrons of higher energy than the other. Transport is prevented because the quantum dot cannot accept additional electrons.

(b) When a quantum dot energy level lies within the bias window, electrons can tunnel into and then out of the dot, passing net current and lifting Coulomb blockade.

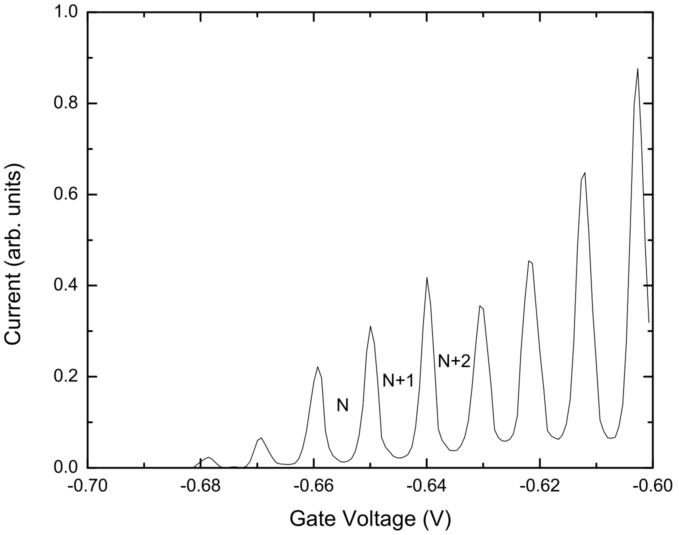

(c) Coulomb blockade data from a GaAs lateral quantum dot, measured at 250mK. Current may flow when the gate voltage is tuned so as to position an energy level within the bias window. The ground state charge number has been indicated between the current peaks, which correspond to the degeneracy conditions. See section 9 for experimental methods.

Figure 3.4: Quantum dot in Coulomb blockade regime.

3.3 Indirect Single Electron Charge Detection

Sometimes, passing a direct current through a quantum dot is either impossible or not desirable. It is not desirable to continuously replace electrons in the quantum dot because maintaining their spin state over long periods is required for many experiments. Additionally, sometimes a non-equilibrium situation must be maintained as part of the experiment and a quantum state with a long life-time is important.

To achieve meaningful results in these regimes, an indirect sensor of charge must be employed. Several nanoscale devices exist which are sufficiently sensitive to nearby charges. An auxiliary capacitively coupled quantum dot can be employed to non-invasively probe the state of a nearby dot[46]. A current is passed through the auxiliary dot in the Coulomb blockade regime, with the dot positioned slightly off-resonance. A small change in the electric field generated by nearby charges can move the auxiliary dot further on or off resonance, resulting in a detectable change of current.

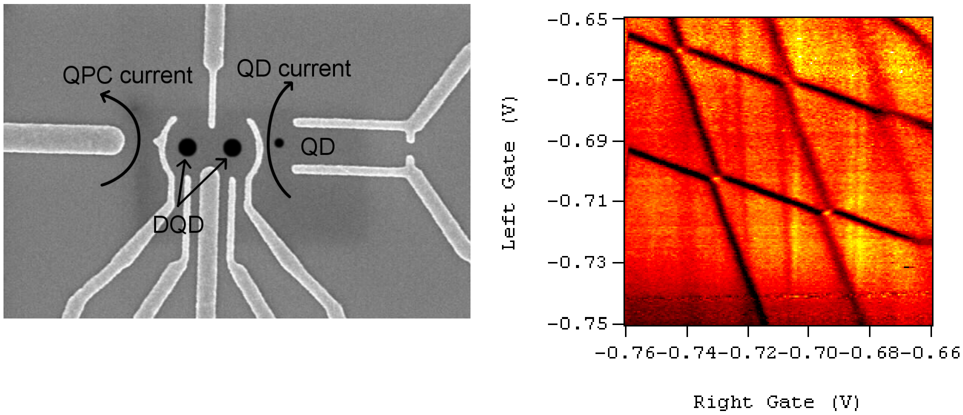

Figure 3.5: A scanning electron microscope image of a gate-defined double quantum dot structure with adjacent QPC and QD, and charge stability diagram. Quantum dots are formed near the circles, including the two dots of interest in the center structure. On the right, the vertically differentiated signal from the QPC highlights abrupt current changes as a function of gate voltage. This kind of measurement is discussed insection 3.6.

A second, simpler, and generally less sensitive device is the Quantum

Point Contact (QPC). The QPC is a restricted channel through which electrons may tunnel. By varying the width of the channel, defined as the size of the undepleted region forming the channel, its conductivity increases or decreases by quanta of $2e^2/h$ due to discontinuous changes in the number of conductive states in the contact which admit electrons through. In the case of an electrostatically defined QPC in a 2DEG, the width of the channel depends on the gate voltage V_G. A QPC tuned between two steps in its I-V_G curve will pass a current that depends sharply on the electrostatic potential at the contact point. A correctly tuned QPC is therefore a very effective charge sensor, since nearby charges will affect the voltage at the QPC.

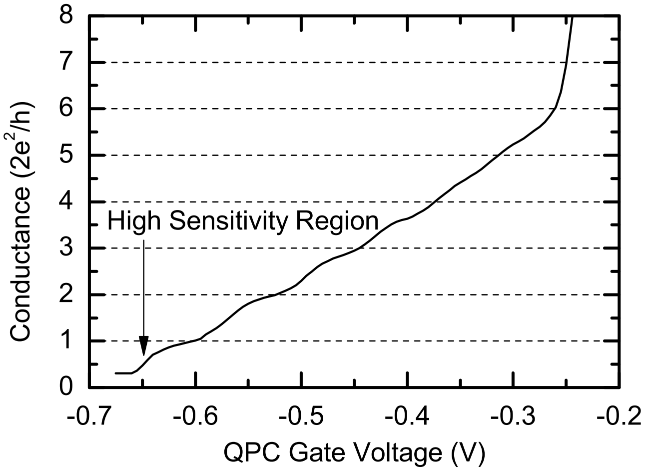

Figure 3.6: QPC conductivity measured at 1.5 Kelvin. Since the conductivity is most sensitive to voltage where the slope is large, the steps between the conductance plateaus are the regions of highest sensitivity when operated as a charge sensor.

The QPC in the step regime and the quantum dot in the Coulomb blockade regime have different advantages and disadvantages. The QPC may be less sensitive in similar conditions, but is is far simpler to set up due to the limited number of gates. It also remains sensitive over a wider range of gate voltages applied to control the quantum dot. It is also less susceptible to charge noise than a quantum dot based sensor. A quantum dot sensor is more sensitive, but more difficult to keep tuned into the correct regime. It may require active feedback to maintain sensitivity. Both devices will lose sensitivity due to intentional or naturally occurring changes in the configuration of charge nearby, or the voltage of nearby gates. For the same reason that the quantum dot is more sensitive, sensitivity is lost more easily during an experiment when the configuration changes. This is a factor to consider in the decision to use a quantum dot or QPC as a charge detector.

3.4 Estimating the Charging Energy of a Quantum Dot

Coulomb blockade experiments permit the measurement of the charging energy of the quantum dot. The electrochemical potential of the quantum dot is:

$$\mu(N) \equiv U(N) - U(N-1) = E_c(N - N_0 - \tfrac{1}{2}) - \frac{E_c}{2|e|}(C_s V_s + C_g V_g + C_d V_d) \quad (3.2)$$

where $E_c = e^2/C$ is the charging energy of the quantum dot.

This is an important quantity because the difference in electrochemical potentials from one charge state to another is:

$$E_c \equiv \mu(N+1) - \mu(N) \quad (3.3)$$

Measuring the charging energy amounts to measuring the total capacitance C, and vise versa.

Measuring the voltages at which current can pass through the dot is straightforward. A small bias voltage is applied between source and drain, $|\mu_s - \mu_d| << E_c$. V_g is varied, and the voltages at which Coulomb blockade peaks occur are recorded (see figure 3.4c). The period of the peaks is proportional to the energy required to add a charge to the quantum dot. However, the actual voltage applied to the quantum dot depends on the circuit capacitances C_g and C. The energy applied to the quantum dot, $(\frac{C_g V_g}{C})$, is not directly measurable. V_g is the directly measured quantity.

A more complex measurement, known as Coulomb diamonds, reveals the required information. By applying a larger bias voltage, one effectively widens the window of voltages which will allow the passage of current. A larger bias voltage therefore leads to proportionally wider Coulomb blockade peaks. When plotting the current through the dot as a function of both the bias voltage and the gate voltage, the result is called the Coulomb diamond pattern.

In contrast to the gate voltage, the source-drain bias voltage is an absolute energy scale. If 10mV of bias is applied, the chemical potential on one side of the dot is 10meV higher than on the other side. This absolute scale can be used to calibrate a lever arm translating between the applied gate voltage (in mV) and the electron energy (in meV).

The slopes of the Coulomb diamonds provide that calibration. If 10mV of bias expands each Coulomb blockade peak by 60mV, then the real charging energy is $\frac{1}{6}$ of the voltage measured in the Coulomb blockade experiment. Simple tricks can be employed to simplify the calculation. If the experimentalist can observe an entire Coulomb diamond, then the width of each diamond (in mV of gate voltage) is twice the charging energy (in meV).

In reality, charge is not the only quantum number that appears in the Hamiltonian, even in the constant interaction model. The energies of the single-particle energy levels should be added to the electrochemical potential:

$$\mu N \equiv E_c(N - N_0 - \tfrac{1}{2}) - \frac{E_c}{2|e|}(C_s V_s + C_g V_g + C_d V_d) + \mathbf{E_n} \tag{3.4}$$

$$\mu(N+1) - \mu(N) = \mathbf{E_{add}} = E_c + \mathbf{\Delta E_n} \tag{3.5}$$

This means that the Coulomb diamond method measures the charging energy only when ΔE_n is zero inside the diamond defined by the intersection of two states of different n. However, this is the case any time electrons are added to the same single-particle energy level. For example, in the absence of magnetic field, a second electron is added which matches an existing electron's orbital quantum numbers, except for opposite spin.

In order to obtain length and area scales for the features which form quantum dots, once can assume that the quantum dot is a disk-shaped capacitor with some unknown radius. The radius of this (fictional) capacitor can then be calculated from the charging energy, being the energy of one electron stored in the capacitor.

The self-capacitance of a conductive disk in a dielectric material with dielectric constant ϵ is: $C = 8\epsilon r$. The dot capacitance is equal to: $C = e^2 E_c$, and E_c can be obtained from a Coulomb diamond measurement (see figure 3.7).

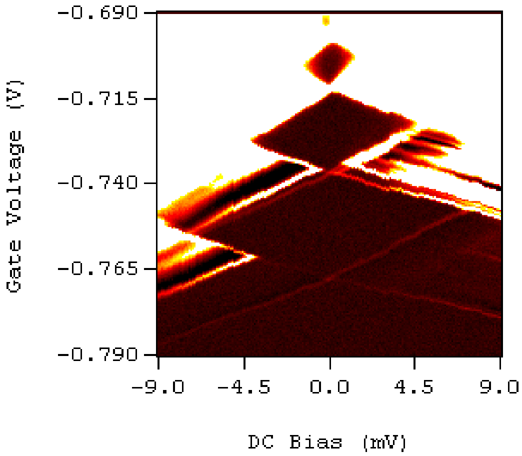

Figure 3.7: A Coulomb diamond measurement of a single quantum dot. Coulomb blockade is visible as current peaks (bright white) along the DC bias = 0mV cut of the figure. Introducing DC bias widens each peak as it is increased in either polarity. The difference in gate voltage between the first and second electron charging events is directly proportional to the charging energy E_c, because these electrons are added to the same spin-degenerate level and thus $E_n = 0$.

3.5 The Double Quantum Dot

The Double Quantum Dot (DQD) is formed by simply combining two single quantum dots in series, such that each is paired with a lead and they share a tunneling barrier between them.

Two "plunger" gates are typically employed which each help raise and lower the potential in one of the two dots. The result is that electrons can be controllably added to each dot somewhat independently, though the plungers will affect both dots to some degree. In the example of figure 3.5, the plunger gates are second left and right-most gates on the bottom.

The ground state of the DQD is not characterized by a single charge number N, but rather a pair of charge numbers (N, M), but it is still possible to map the ground charge state as a function of two gate voltages.

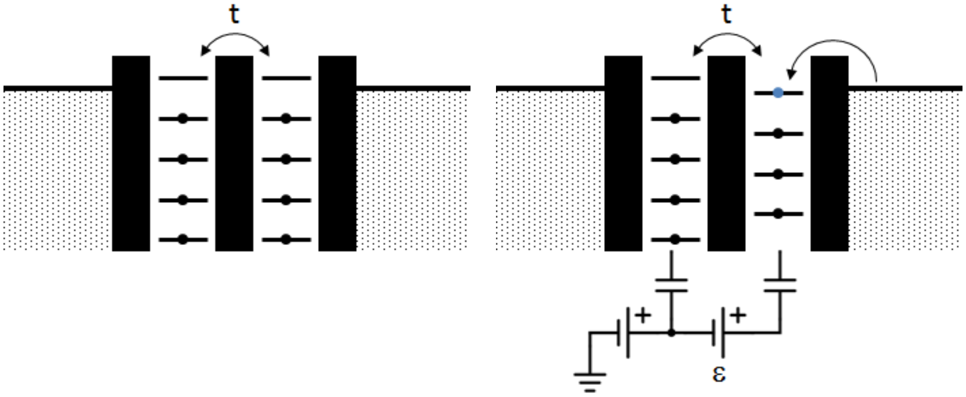

(a) Conceptual diagram of the double quantum dot with two leads. The dots are tunnel coupled through a barrier.

(b) Conceptual diagram of the DQD in the detuned regime. The right dot has a lower potential. The chemical potential difference ϵ between the two quantum dots, in this case promoting the addition of an electron to the right dot from the right lead.

Figure 3.8: The double quantum dot (DQD)

3.6 The Stability Diagram

Coulomb blockade will also occur in the DQD. In fact, current can only pass through the DQD if there is a three-fold degeneracy in the ground state between the charge states (N, M), $(N + 1, M)$, and $(N, M + 1)$. This allows electrons to move into the DQD from the source to the left dot, move across the tunnelling barrier to the right dot, and ultimately into the drain, without ever receiving or giving up any energy.

The triple degeneracy points, or "triple points", can be observed in the low bias regime in the same way that Coulomb blockade peaks can be observed for the single quantum dot. However, two gate voltages (V_{g1} and V_{g2}) must be varied in order to observe all of the possible triple points. At each triple point (V_{g1}, V_{g2}), the current is measured. The result is generally nearly uniform zero current, except at the triple points, where current may pass (see figure 3.10).

The triple points reveal interesting behaviour. In the low bias regime, they are simply points. In the high bias regime, triangular regions of current extend from the points. In some of these triangles, for example extending from the (0, 1), (1, 1), (0, 2) triple degeneracy point, evidence of Pauli blockade can sometimes be observed[26].

However, studying only the triple points neglects a wealth of hidden information. Double degeneracies are invisible in the transport measurement, and it is difficult to know for certain the charge state of a DQD at any given set of gate voltages simply by measuring the positions of the triple points. Fortunately, this information is revealed in a charge stability diagram, which is a measurement of the current through a nearby charge detector as a function of two DQD gate voltages.

By measuring transport through a charge detector as a function of the gate voltages of the quantum dot, changes in the charge distribution of the DQD can be probed directly. The resulting intensity plot as a function of two gate voltages is called a charge stability diagram (often simply “stability diagram”). The name refers to the fact that the diagram reveals which charge states are stable (ground states) for each pair of gate voltages. See figure 3.9 for an example.

Consider a particular scenario. On a given DQD, two gates which are each localized to a particular dot are varied independently. The charge detector is expected to pick up both the change in charge of the gates, as well as the discontinuous change in charge distribution of the DQD. The result is that several regions of gradual slope are separated by discontinuous jumps where the ground state changes from one charge state to another. By differentiating this data along any axis, but typically along the sweep direction, the gradual slopes disappear and the discontinuities become contrasted lines (black, in this colour scheme). These mark the borders between charge states.

The faint bright line at the center of figure 3.9b corresponds to a movement of charge from one dot to another, conserving the total electron number. These are tipping points in the balance of two forces. On the one hand, the most energetic electron is more stable if it occupies the quantum dot with the lowest available single-particle quantum state. However, the extra electrons in this quantum dot will repel the very same electron. On either side of the charge transfer line, the balance of these two forces comes out in favor of the valence electron occupying one or the other quantum dot[36].

Examine 3.9. Notice that two sets of parallel dark lines exist, characterized by a distinct slope. In this colour scheme, dark lines correspond to a change in the total number of electrons (of one elementary charge). They are also called “addition lines”, because when crossing such a line the total

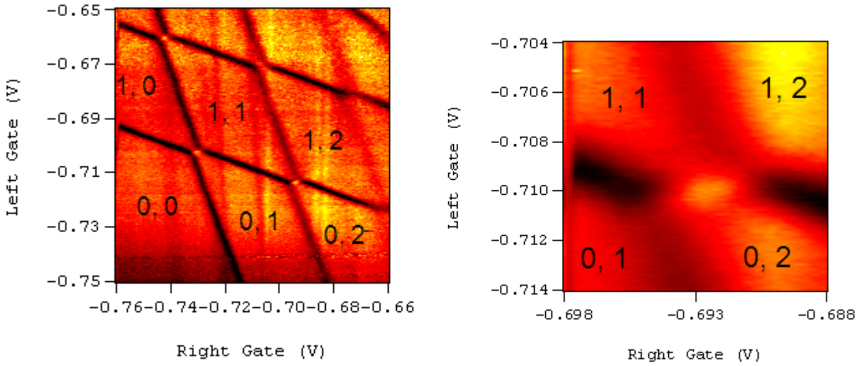

(a) Multiple regions with different ground state charge configurations.

(b) Close zoom of the area where two addition lines cross. The light line, which appears almost point like here, is the charge transfer line.

Figure 3.9: Differentiated current through a nearby QPC produces the charge stability diagram of a DQD. This data is discussed in detail in section 10.

charge number increases (or decreases) by one, depending on the direction of motion in voltage space. The slope of the lines indicates which quantum dot the new charges occupy. While both gates may have some effect on both quantum dots, each dot is more sensitive to one gate than the other. This is the cause of the different slopes[36].

Several features are noteworthy in the stability diagram. First, notice in 3.9 that the addition lines come in two parallel sets, but that each line appears to deflect away from the other as it nears an intersection. This is due to two simultaneous effects. First, there is capacitive coupling between the quantum dots. When an electron is added to one dot, the energy cost of adding a second electron to the other dot becomes greater. This causes addition lines to appear to "jump"[36] (see figure 3.9b). Near the triple points, the states (N+1, M) and (N, M+1) become nearly degenerate. Tunnel coupling between the quantum dots causes these two states to hybridize, resulting in a curved shape that is most pronounced when the tunnel coupling is large[26]. These effects can therefore be used to estimate the Coulomb and tunnel coupling of the DQD[26].

Spin effects can express themselves in the vicinity of the charge transfer line, especially between fully odd and fully even charge states (ex: (3, 3) and

(4, 2)). In the nextsection, we will examine one such effect.

3.7 Pauli Spin Blockade

Another transport experiment involves the Pauli exclusion principle. Two quantum dots are each coupled to a lead, and to each other, by tunnel barriers. One dot is detuned so that an electron is trapped in the dot, while the other is tuned so that any electron may enter it. There is a potential difference between the two leads such that an electron in the upper dot lead may enter the second dot and attempt escape into the lower lead through the lower dot (see figure 3.10).

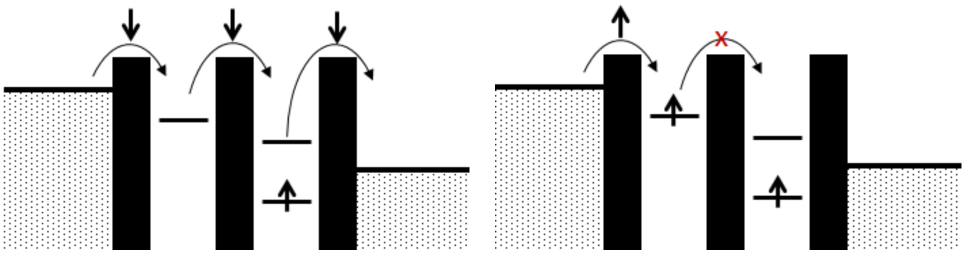

(a) Schematic of a double quantum dot under bias. The right dot already contains an electron of a particular spin. If an electron of the opposite spin enters from the left lead, it will tunnel through each dot to the opposite lead.

(b) An electron of the same spin, entering from the left lead, is unable to tunnel from the left dot to the right because of the Pauli exclusion principle. The electron is trapped and current is blocked until either electron spin is somehow inverted. This is called Pauli blockade.

Figure 3.10: Left: Transport through a multiple quantum dot under bias. In the absence of magnetic field, hyperfine interaction randomizes the spin states and Pauli blockade is lifted, permitting free flow of current at the base of the yellow-green triangular region. Note the triple points and the bias triangles extending from them. Right: With the addition of a static magnetic field (in this case 0.2 T), current is suppressed in the interior of the bias triangle due to Pauli blockade[9].

According to the Pauli exclusion principle, no two electrons of like spin may occupy the same total quantum state, so that the moment an electron of

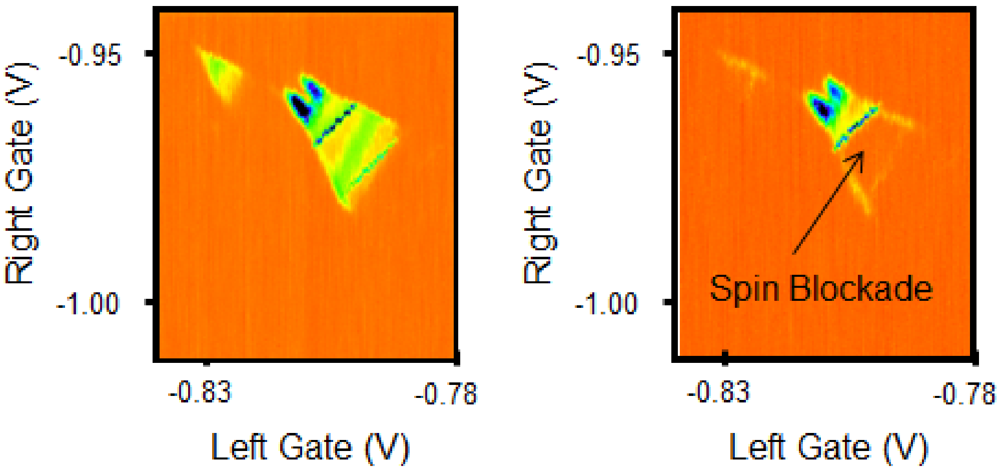

Figure 3.11: Left: Transport through a quantum dot under bias. In the absence of a magnetic field, hyperfine interactions randomize the spin states and Pauli blockade is lifted, permitting free flow of current at the base of the yellow-green triangular region. Note the triple points and the bias triangles extending from them. Right: With the addition of a static magnetic field (in this case 0.2 T), current is suppressed in the interior of the bias triangle due to Pauli blockade[9].

like spin enters the upper dot, it is trapped. Current will therefore not pass through the dot. This effect is called Pauli blockade after the Pauli exclusion principle, and it can be used to measure the g-factor of each dot in a DQD with the assistance of spin resonance, as described in the nextsection.

3.8 Measuring g-factor in Single and Double Quantum Dots

Because the wavefunction and energy spectrum of the charges are different in quantum dots as compared to bulk material, their effective g-factor may be different. Contributions to this difference originate from the width of the quantum well, the composition of the material, strain, and the action of an external electric field. It is possible to measure the value of the effective g-factor in several different ways, by employing a magnetic field.

In a single quantum dot, measurement of electron g factor can be accomplished as follows. By applying a sufficiently large magnetic field, once spin-degenerate energy levels will begin to split via the Zeeman effect. The Zeeman energy imparted must exceed the thermal broadening of the energy levels, or roughly $k_B T$. Thanks to their differing energies, the two levels will each lift Coulomb blockade at different gate voltages. Assuming one has used the Coulomb diamond method (section 3.4) to calibrate the gate energy scales, one can use the difference in energy of these two Coulomb blockade peaks at a particular value of magnetic field to calculate the g-factor by assuming that the Zeeman term is equal to the splitting[27, 56]. The Zeeman energy must be greater than the thermal broadening of the fermi level ($g\mu B > kT$) or the peaks will overlap. For an achievable electron temperature of 150mK and typical g-factor of GaAs (0.4), fields in excess of several T are required to achieve visibility. Higher electron temperatures or smaller g-factors may require proportionally higher magnetic fields for good visibility, up to 5 T in practice[27]. However, this method is not compatible with the very small electron g-factors required for quantum repeater applications, since the magnetic fields required are prohibitive.

In a DQD system, one can measure g-factor in a different manner. A DQD configured so that the (0, 1), (1, 1) and (0, 2) charge states are nearly degenerate and in the presence of a magnetic field, is said to be in the Pauli blockade regime, and current in one direction is suppressed in a region adjacent to the triple point. In this regime, the (1, 1) spin triplet states ($|\uparrow\uparrow>$, $|\downarrow\downarrow>$, $\frac{1}{\sqrt{2}}(|\uparrow\downarrow> + |\downarrow\uparrow>)$) cannot relax into the corresponding (0, 2) spin states because the total wavefunction would be symmetric. If the system enters any of these states, the quantum dot is Pauli blockaded and will not pass current through the usual (0, 1) $\rightarrow$ (1, 1) $\rightarrow$ (0, 2) $\rightarrow$ (0, 1) cycle. This condition can be lifted if the triplet state decoheres into the spin singlet through hyperfine interaction with the abundant nuclear magnetic moments of a material such as GaAs, since this state is permitted to tunnel. However, the next electrons to enter the quantum dot has a high probability of forming one of the three triplet states, again blocking current. Without the applied magnetic field, however, the increased efficiency of random hyperfine interactions with the spin state lifts the Pauli blockade condition and allows a small current to pass (on the order of fA for a T_2 spin coherence time in GaAs of about 20ns.

An electron spin resonance experiment with high frequency magnetic (or electric fields, if one makes use of spin-orbit effects) can be used to artificially lift the Pauli blockade[48]. Through an applied field of the appropriate frequency, electrons in the dots can be resonantly driven to Rabi type oscillations. Changing the spin of either electron will lift the Pauli blockade condition, allowing current to flow. By measuring the frequency that maximally excites these resonant spin transitions at a particular magnetic field, the g-factor in each dot can be measured by using the well-known relationship $f = g\mu_B B/\hbar$, where μ_B is the Bohr magneton and B is the external magnetic field. In general the g-factors in each dot may not necessarily be the same, and two different resonances will be detectable.

3.9 Summary

- Within the constant interaction model for a quantum dot, it is possible to estimate the size of a quantum dot using Coulomb diamond measurements.
- The phenomenon of Pauli blockade suppresses current through a double quantum dot in the presence of magnetic field, unless forces disturb the spin state of the electrons in the dot.
- Using Coulomb and Pauli blockade, it is possible to measure the effective g-factor of a single quantum dot or both dots in a double quantum dot (respectively).

In the next section, we shall see that the Pauli exclusion principle in a double quantum dot can be used to read out the spin state without requiring transport through the double quantum dot, as the Pauli blockade experiment requires.

Chapter 4

Introduction to Spin Qubits

4.1 Motivation for spin qubits

Research interest into spin qubits is motivated by the fact that electron spins are true two-level systems, and that solid-state spin qubits in semiconductor nanostructures have the support of decades of heavy development in the semiconductor industry. As a result, spin qubit systems are in principle scalable to arbitrarily many qubits. Furthermore, being magnetic rather than electrical phenomena, spin qubits are more weakly coupled to their environment. Still, it has been shown that spin qubits can be effectively controlled with electric fields while remaining insensitive to background noise[46].

4.2 The computational basis

A spin qubit is defined by identifying two orthonormal states of a spin system. Usually one chooses these such that one of them is a state which can be easily prepared, or the eigenstate of a projective measurement that can be performed on the system. This state is labelled |0>, and its orthogonal compliment is |1>. These states form the so called computational basis of the system.

4.3 Spin qubits and the DiVincenzo criteria

A general implementation of a quantum computer must satisfy certain criteria. While many different equivalent sets of criteria exist, the most popular is known as the DiVincenzo criteria, named for David P. DiVincenzo[15].

The DiVincenzo criteria for a qubit platform to be useful as a general quantum computing platform are:

1. *A scalable physical system with well characterized qubits.* Spin qubits are expected to be quite scalable, though systems of millions of interconnected qubits have yet to be demonstrated.

2. *The ability to initialize the state of the qubits to a simple fiducial state, such as* $|000...>$. Spin qubit initialization can be achieved, for example, by allowing the spin system to decohere into the ground state. Alternatively, any ideal projective measurement of the qubit leaves it in a known state, which can be corrected to the desired initialization state or, perhaps, used immediately.

3. *Memory qubits with long decoherence times.* Memory qubits used for entanglement swapping must survive longer than the communication time between adjacent nodes in a repeater chain. For links of length 50 km, this corresponds to about 150 µs. A quantum memory with much greater than 1 ms coherence time should therefore be sufficient, assuming the memory can be read out in that time. Coherence times have been demonstrated for spin qubits as long as 39 minutes in isotopically purified Silicon[51].

4. *A universal set of quantum gates. That is, a set of gates which, in combination, can generate all possible computable functions.* A “universal” gate set is one which can easily generate all other possible logical gates. An example is the Z gate, which corresponds to Larmor precession of single spins in a static magnetic field, and the X gate, which corresponds to Rabi oscillation of a single spin in an oscillating magnetic field. These two rotation operators can be used to approximate any single-qubit unitary operation using the Solovay-Kitaev algorithm[14]. Entangling operations can also be performed between single spins, and these have been demonstrated[yacobirootswap].

5. *A qubit-specific measurement capability.* Read out of spins can be achieved by attempting to overlap the wavefunction of the unknown spin of interest with some known reference spin[20]. The exchange interaction will result in a different distribution of charge in the case of like spins compared to the case of unlike spins. [1] Measurement of this charge, as in section 3.3, reveals the spin state of the qubit to be either parallel to the known spin or anti-parallel. This is called "spin to charge conversion", and can be conducted in double quantum dots in the un-biased regime using a charge detector[19].

6. *The ability to interconvert stationary and photonic qubits.* Photon to spin conversion is discussed in section 6.

7. *The ability to faithfully transmit photonic qubits between specified locations.* Transmission of photons over long distances has already been achieved[41].

4.4 Basis states of DQD spin system

The spin state of a Double Quantum Dot (DQD) with two electrons can be characterized by four spin states: $|\uparrow\uparrow>$, $|\downarrow\downarrow>$, $|\downarrow\uparrow>$, and $|\uparrow\downarrow>$. However, these are not the eigen-states of a DQD when tunnel coupling between the two dots is significant and each dot is occupied by one electron. Instead, we can use the orthonormal basis of total spin component eigenstates for a system of two spin $\frac{1}{2}$ particles:

- $|J=1, m=+1> = |T^{+}> = |\uparrow\uparrow>$
- $|J=1, m=-1> = |T^{-}> = |\downarrow\downarrow>$
- $|J=1, m=0> = |T^{0}> = \frac{1}{\sqrt{2}}(|\downarrow\uparrow> + |\uparrow\downarrow>)$
- $|J=0, m=0> = |S> = \frac{1}{\sqrt{2}}(|\downarrow\uparrow> - |\uparrow\downarrow>)$

The $|S>$ and $|T>$ identification stands for "singlet" and "triplet" respectively, in reference to the grouping of states by their total spin.

---

[1] Exchange, for our purposes, is that phenomena which ties different orbital eigenfunctions (and eigenenergies) to different spin states on the basis of fermions of like spin repelling one another.

This basis turns out to be the correct eigenbasis for DQD's. The reason is best understood by symmetry. The $|S>$ state is antisymmetric in spin, and thus symmetric in wavefunction (because fermions are antisymmetric overall). Its symmetric wavefunction allows the singlet state to overcome the Pauli exclusion principle that restrains the antisymmetric triplet states, allowing the electrons to settle into a lower energy ground state wavefunction.

As demonstrated in figure 3.8b, this effect is most pronounced when the DQD is detuned such that one quantum dot is at a significantly lower potential than the other. Both electrons of the singlet state can occupy this lower quantum dot together, while the triplet state is constrained to leave one electron in the higher potential quantum dot. The energy term of the Hamiltonian that expresses this reorganization of orbital wavefunctions due to Pauli's principle is sometimes called "exchange" in reference to its origins in the classic Heisenberg model[25], and lifts the degeneracy between the singlet and the triplet states.

Independent of exchange, the presence of a uniform magnetic field will lift the degeneracy within the spin triplet. The Zeeman energy, proportional to the quantum number m, adds and subtracts equal energy from the $|T^+>$ and $|T^->$ states respectively (if we assume positive effective g-factor). The $|T^0>$ and $|S>$ states are not affected, and as such it is quite possible that either $|T^->$ or $|T^+>$ will be lower than $|S>$ as a result, depending on the detuning of the double quantum dot, the sign of the field, and the gyromagnetic ratio of electrons in the dots.

4.5 Hamiltonian of DQD spin system

Taking all of this information and encoding it in a Hamiltonian, we arrive at the spin Hamiltonian of a double quantum dot:

$$H = -J|S><S| + \frac{g\mu_B B}{2\hbar}|T^+><T^+| - \frac{g\mu_B B}{2\hbar}|T^-><T^-| \tag{4.1}$$

where J is the exchange energy, μ_B is the Bohr magneton, and g is the effective g-factor of the quantum dot (which may be negative, and is dependent on the material system). The energy of the $|T^0>$ eigenstate is taken as the reference energy in this representation, and therefore is assigned the eigenvalue zero. See figure 4.1.

The resulting time-evolution operator for evolution to a time 't' in the future is:

$$U(t) = exp(\tfrac{iJt}{\hbar})|S><S| + exp(\frac{-ig\mu_B Bt}{2\hbar^2})|T^+><T^+| + exp(\frac{ig\mu_B Bt}{2\hbar^2})|T^-><T^-| \tag{4.2}$$

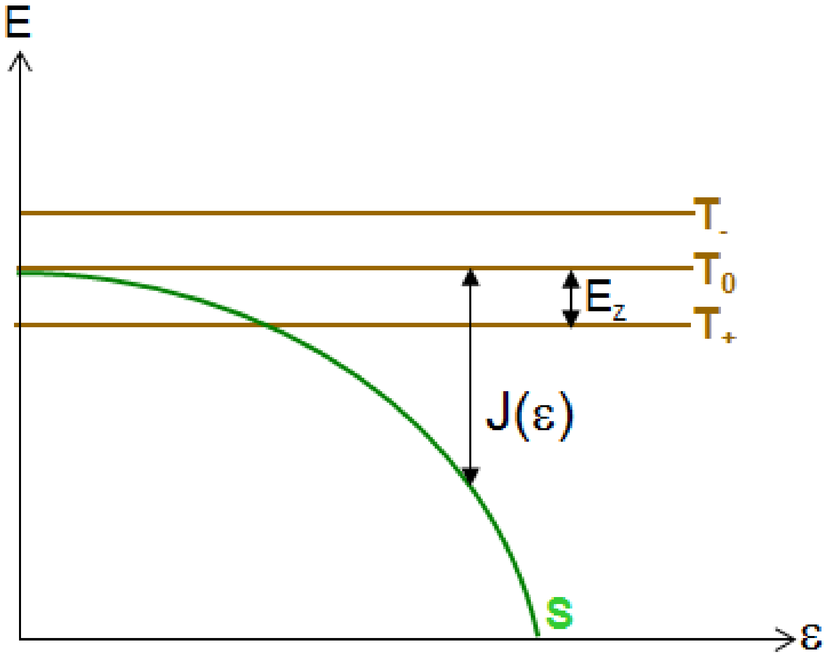

Figure 4.1: Sketch of the energies (relative to the T_0 state) of the lowest energy spin eigenstates of the double quantum dot. The lack of Pauli exclusion restrictions on the spin singlet allows it to split off from the T_0 state by the exchange term ($J(\epsilon)$) as detuning increases, while the spin triplet states are split apart by the Zeeman energy (E_z) in the presence of a static magnetic field.

4.6 Projective singlet/triplet measurement

It is through the exchange parameter J that Bell measurement is possible, and this will be described in detail in section 5.

In the double quantum dot, two forms of measurement are possible. Previously, we discussed comparing a single spin qubit to a reference spin qubit. If we say that the reference spin is certainly spin up, the possible initial states are $|T^{+}\rangle = |\uparrow\uparrow\rangle$ and $|\downarrow\uparrow\rangle$. Upon detuning the DQD into the (0,2) or (2,0) regimes, the charge distributions for the two states will differ. Because $|\uparrow\uparrow\rangle$ is Pauli blocked, it will remain in the (1,1) charge distribution. The $|\downarrow\uparrow\rangle$ state has non-trivial $|S\rangle$ component, and will display a different charge configration. A nearby charge detector will report the difference.

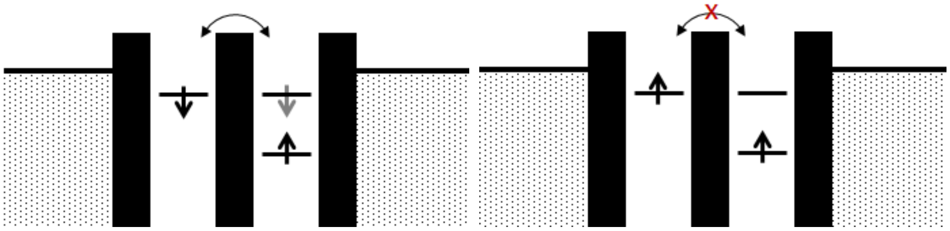

(a) If the spin of interest is opposite from the reference spin, the spin may tunnel from one dot to another.

(b) If the spin of interest is the same as the reference spin, it is forbidden from tunnelling from one dot to the other.

Figure 4.2: The two orthonormal basis states of the single spin qubit, $|\uparrow\rangle$ and $|\downarrow\rangle$, can be differentiated by preparing the (1, 1) charge state. One electron is the spin of interest, while the other is a known reference spin. The DQD is then detuned such that (0, 2) becomes the ground state. If the two spins are the same, the ground state is accessible and the charge state will change. If not, the charge state remains the same. This is the conversion of spin information into more easily detectable charge information.

Detuning the DQD into the (0,2) or (2,0) regime functions as a projective measurement into the singlet ($|S\rangle$) subspace, or into the triplet ($|T\rangle$) subspace. It is the fact that the singlet is an entangled state (actually a Bell state) that enables efficient Bell analysis of spin qubits with this device.

4.7 Summary

- Spin qubits are attractive for scalable general quantum computation, either having been demonstrated theoretically or practically to satisfy all of the DiVincenzo criteria.

- For the particular application of entanglement swapping, spin qubits offer competitive decoherence times.
- The particulars of spin qubits in DQD's with strong tunnel coupling enables direct Bell measurement without the need for coherent entangling gate operations.

Chapter 5

Bell Basis Measurement with g-Factor Engineered Spin Qubits

We wish to perform full Bell measurement of two photonic qubits so as to realize a quantum repeater. Directly performing Bell analysis of photonic qubits is undesireable due to the destructive nature of photon detectors and the difficulty in fully entangling and disentangling photon polarizations in a coherent manner using linear optics (see section 2). However, first converting the photonic qubits into stationary qubits such as electron spins enables full Bell measurement and all the benefits thereof. Conversion of photonic qubits into spin qubits will be reviewed in section 6.

5.1 Implementation

As described in section 4, two spin qubits in a double quantum dot can hybridize in such a way that the singlet and triplet states are split off by an exchange energy term, while the triplet itself is split by the Zeeman energy. The relevant equation is 4.1.

Notably, the singlet state $|S>$ and the triplet state $|T^0>$ are both Bell states, while the remaining eigenstates ($|T^+>$ and $|T^->$) are separable. Because the singlet is one of the possible unambiguous results of a projective measurement by spin to charge conversion[19], it functions as a partial Bell measurement. If the measurement result is a singlet, Bell measurement has succeeded and given a valid result. Otherwise, the state is projected into the subspace spanned by the remaining eigenstates.

Unlike partial Bell measurement of photons, Bell measurement of spins can be repeated since it is non-destructive. A control sequence which swaps the $|T^0>$ and $|S>$ states, followed by another projective measurement into the singlet, provides discrimination of another Bell state. Qubit manipulations which exchange each Bell state with the singlet in turn will eventually provide full Bell measurement (see figure 5.1).

The process of control and measurement both take time, however, during which the qubit will evolve. The $|S>$ and $|T^0>$ are eigenstates of both the Hamiltonian and of the spin to charge readout operation. The phases accumulated by the $|S>$ and $|T^0>$ states are therefore incapable of influencing the outcome of the Bell measurement, and these states can be read out easily. On the other hand, the evolution of the two remaining Bell states, $|\Phi^+> = \frac{1}{\sqrt{2}}(|T^+>+|T^->)$ and $|\Phi^-> = \frac{1}{\sqrt{2}}(|T^+>-|T^->)$, must be accounted for.

Recalling equation 4.2, the relative phase accumulated between the $|T^+>$ and $|T^->$ eigen-states is ωt, where $\omega = \frac{\bar{g}\mu_B B}{\hbar^2}$ and $\bar{g}$ is the average g-factor of the DQD. The oscillation could be cancelled by waiting until $2\pi N$ rotations had occured for any positive integer N, assuming the oscillations are slow. The oscillation rate can be minimized by setting the average g-factor between the two quantum dots to zero.

Control pulses can make use of non-zero g-factors on each individual quantum dot to actively manipulate the spins, even if the average g-factor is near zero to prevent passive oscillation between $|\Phi^+>$ and $|\Phi^->$. This experiment has been proposed[61], but has not yet been performed because no material systems have yet been developed which support the the near-zero g-factor condition in quantum dots.

Figure 5.1 attempts to summarize the proposed experiment visually. Note that while the figure simplifies the process by assuming pauli operations can be applied to just one qubit, this is in fact not necessary. Instead, one might use a $\pi/2$ rotation about the Z axis of each qubit to achieve the equivalent of a π Z rotation of one qubit, since the Z axes of each qubit are anti-parallel. Separable two-qubit operations of this type can be used to replace all of the pauli operators for this purpose[61].

The complete algorithm is as follows:

1. Immediately perform spin to charge conversion to confirm or rule out

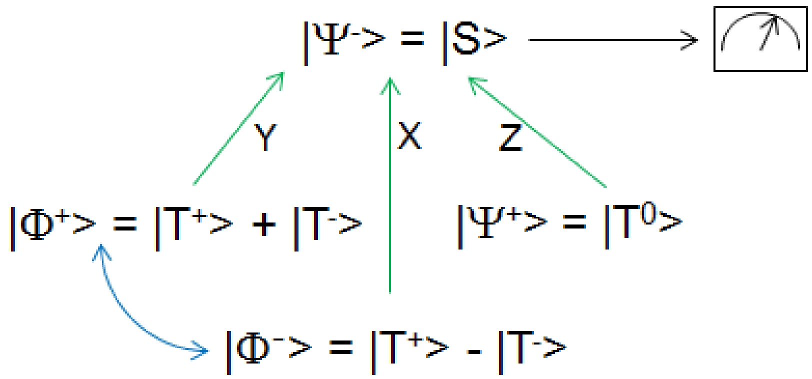

Figure 5.1: Using spin to charge conversion in a double quantum dot (black arrow) to project into the singlet and triplet subspaces, one achieves partial Bell measurement. Single qubit operations of different types (X, Y, and Z Pauli operators) performed on just one qubit swap each Bell state with the singlet, allowing spin to charge conversion to test for these too (in sequence). Passive oscillations (blue, curved arrow) between the two states of even parity can be suppressed in a DQD with near zero average g factor.

the $|S>$ state. If the result is not $|S>$, the system remains in a superposition of the other three states.

2. Swap the $|S>$ and $|T^0>$ states with either a single π rotation of one qubit about Z or a $\pi/2$ rotation of each qubit about its respective Z axis (they are oppositely oriented due to the asymmetric g-factor).

3. Repeat spin to charge conversion. A result of $|S>$ now implies the initial state was $|T^0>$.

4. Swap the $|S>$ and $|\Phi^->$ with a single π rotation or two $\pi/2$ rotations about X.

5. Repeat spin to charge conversion. A result of $|S>$ now implies the initial state was $|\Phi^->$.

6. Either similarly swap and read out the $|\Phi^+>$ state, or infer it as an outcome as it is the only remaining state.

We shall see in the next section that the zero electron g-factor condition also offers the possibility of transferring quantum information between a photonic qubit and a stationary (spin) qubit.

5.2 Summary

- In this section, we reviewed why zero average g-factor in a double quantum dot is an enabling condition for Bell measurement.
- In double quantum dots with zero average g factor, the Bell states are steady states.
- If the individual g-factors are also non-zero (and therefore asymmetric), the Bell states can still be swapped for one another using electric or magnetic fields for control.
- Repeated projection into the singlet state, combined with qubit manipulations, can yield an ideal Bell measurement in the DQD system.

Chapter 6

Photon to Spin Interfaces in g-factor Engineered Nanostructures

6.1 Advantages and Limitations of Photonic Qubits

We have seen in the previous section that spin qubit devices in principle may natively support Bell measurement, the key primitive for quantum teleportation and entanglement swapping algorithms in quantum communication and QKD. However, as useful as this might be, spin qubits are not particularly mobile and are ill-suited for long-distance communication of quantum information.

Though matter-based qubits have been investigated for the purposes of transporting spin information, including by way of superfluid Helium[7], surface accoustic waves[30], or superconducting cavities[49], nothing suggests that long-distance telecommunication links on the scale of kilometers are possible with these technologies.

The photon, on the other hand, is a nearly ideal qubit for long-distance communication of quantum information. Various photonic qubits have been studied, including time-bin encoded qubits[45], and polarization qubits[31, 38]. Interconversion between these different qubits is possible[32], so that any technology which is compatible with one type of qubit is potentially compatible with any of them.

Whatever the qubit, photons are remarkable because incoherent interactions with matter are weak. The telecommunication industry has developed robust optical fiber technology which is compatible with the transmission of quantum information using photons as the transmission qubits[22]. Experiments in free space and optical fibers have successfully transmitted quantum information over hundreds of kilometers over optical fiber and free space links[22, 42].

Unfortunately, while photons are ideal for transmission, they suffer greatly when it comes time to do arbitrary quantum computation with them. We have seen in section 2 that Bell measurement of photons is generally not sufficient to achieve long-distance high-throughput quantum communication channels.

Furthermore, the measurement of a photonic qubit is typically done by using the energy of the photon to initiate a cascade reaction in a detector, thereby destroying the photon[13, 47]. The destructive nature of these detectors limits what can be done with photonic qubits.

6.2 Spin Qubit Quantum Memories

We have seen in section 5 that Bell states can be disambiguated perfectly within the quantum dot spin qubit platform. When the $\bar{g} = 0$, $g_1 = -g_2$ condition is met, Bell states are steady states of a double quantum dot. With ESR and spin to charge conversion, discussed in sections 4 and 5, one can implement Bell measurement on two arbitrary spins. In principle, there is no known limit to the fidelity and success probability of Bell measurement in a spin qubit system, which is what is needed to enable arbitrarily long distance quantum links with the aid of a quantum repeater.

Solid state spin qubits composed of charged electrons in quantum dots also have the advantage of having an exposed charge which is decoupled from their spin. Whereas quantum memories for photonic qubits generally cannot report how many photons they have stored, and direct detection of photons necessarily destroys them, the detection of a charged spinor in a quantum dot is not destructive of the qubit. Therefore, it is possible to build “heralded” quantum memories from spin qubits. The fact that one can detect whether the memory is filled significantly relaxes requirements that quantum memories be highly efficient in terms of capturing photons.

6.3 Transfer of Quantum Information from Photon to Spin

To convert a photonic qubit into a spin qubit, one can take advantage of angular momentum selection rules for photons absorbed by electrons in a solid.

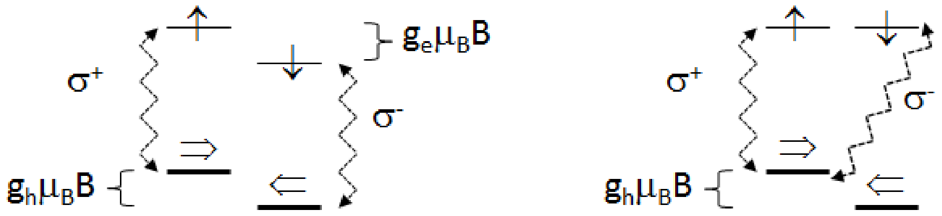

(a) In one scenario, two different valence and conduction band states are coupled, each by a different polarization of electric field. The quantum information resides in the resulting (entangled) electron/hole system. $g_e = g_h$ in this scenario so that the same electric field frequency need not be correlated with the polarization.

(b) In another case, two different conduction band states are coupled to the same valence state, each by a different polarization. The quantum information resides solely in the electron. The electronic g-factor g_e must be zero for this to work.

Figure 6.1: Two scenarios in which quantum information from a photon can be transferred to a spin system in a quantum well, either an electron/hole pair (a) or simply an electron (b). In both cases, a static magnetic field has been applied in the plane of the well.

Suppose we have an optically active quantum well, and a source of single photons. Electron-hole pairs can be created by coupling valence and conduction band states in a variety of ways, for example the two scenarios of figure 6.1. An ideal situation is that of figure 6.1b, where the hole that is created ultimately contains no useful information and can be discarded safely, either by allowing it to tunnel out of the quantum dot or by pulsing a nearby gate to actively remove it. With the hole gone, the electron spin contains the information of the original photon state and the charge of the electron heralds the successful transfer of information[34].

To achieve the coupling of two conduction band states to a single valence band states, one must make use of the quantization conditions and optical selection rules for light holes and electrons in a quantum well under the influence of a static magnetic field. Assume a magnetic field is applied in the plane of the quantum well. The zeeman splitting of the electrons will be zero if the g-factor is zero, so there will be no preferred quantization axis for the electrons. However, the light holes are quantized along the magnetic field. Light incident perpendicular to the surface of the quantum well induces transitions between spin states quantized along the perpendicular axis of the quantum well, and the target state (for example, say) $|\Rightarrow> = \frac{1}{\sqrt{2}}(|\Uparrow>+|\Downarrow>)$ is an even superposition of each of those two states. Therefore, photons incoming perpendicular to the surface of the sample will (at best) have a 50% probability of absorption according to the following rules:

$$\begin{gathered}
|\sigma^{+}> \rightarrow |\uparrow\Rightarrow> \\
|\sigma^{-}> \rightarrow |\downarrow\Rightarrow> \\
\frac{1}{\sqrt{2}}(\alpha|H> + \beta|V>) \rightarrow \frac{1}{\sqrt{2}}(\alpha|\uparrow> + \beta|\downarrow>) \Rightarrow
\end{gathered}$$

The principle of quantum state transfer has been demonstrated in bulk GaAs quantum well structures[34, 35], but has not yet been conducted in quantum dots. The importance of quantum media conversion from photon to spin has motivated our investigation of InAsP/InP nanostructures. The InAsP material shows promise as a material platform for small electron g-factor quantum dots, as we will soon see. The next two sections present (respectively) theoretical and experimental investigations into techniques for engineering small g-factor quantum well structures suitable for quantum dots, and Indium alloy few-electron quantum dot nanowire structures.

6.4 Summary

1. In principle, it is possible to convert photon polarization information into electron spin information.
2. Photons create electron-hole pairs when absorbed in semiconductor, and both particles may contain information from the photon.
3. In the zero electron g-factor regime, the information contained in the hole can be minimized. The hole can therefore be discarded.

Chapter 7

Approaches to g-Factor Engineering

The electron g-factor, which is the constant of proportionality between the electron spin to its magnetic moment, is an important consideration in the design of spin qubits. Qubits with large g-factors are strongly influenced by magnetic fields, resulting in fast operations times and sensitivity to magnetic environmental noise. We have seen that quantum dot devices with specific g-factors are important for realizing a particular implementation of the quantum repeater.

The quasi-particles commonly referred to as "electrons" in solid state physics are abstractions, having some of the properties of their free particle counterparts. Generally, they do not have scalar masses, except in the effective mass approximation. Their spins and angular momenta can couple to one another far more strongly than atomic or free electrons. It is no surprise, therefore, that their magnetic moments are not necessarily the same as for free electrons.

In general, the overall g-factor of a solid state electron can be greater, lesser, or opposite in sign from the $g_0 \approx -2$ of free electrons. In fact, solid state electrons can even exhibit zero magnetic moment altogether [64]. Different materials produce quasi-particles with different parameters, and both heterostructures and alloys allow the engineering of particular characteristics such as spin-orbit coupling, effective mass, and electron magnetic moment.

7.1 g-factor Engineering with Single Quantum Wells: Composition and Thickness

Because different bulk materials possess different effective g-factors for electrons in the conduction band, changing the material or material composition is a method for changing the g-factor. Alloys of two or more elements can be further tuned by varying the composition ratios of one element to another. Figure 7.1 illustrates the dependence of the g-factor on the composition of quantum well structures composed of ternary alloys of Indium, Gallium, Arsenic, and Phosphorus.

Instead of changing the composition of a single piece of material, the g-factor of a heterostructure can be determined by changing the amount or shape of the material. When electrons are confined to a quantum well of finite depth, as in figure 7.2, their wavefunctions penetrate into the barrier material. Since the barrier material generally has a different effective electron g-factor than the quantum well itself, the overlap of the electron with the two regions results in an effective g-factor which lies somewhere between the two. In particular, a layer of semiconductor (ex: InAsP) embedded in an insulating barrier (ex: InP) will have variable g-factor with respect to the thickness of the semiconductor layer. As the thickness changes, the degree of wavefunction overlap with the barrier also changes. This dependence on quantum well width is also illustrated in figure 7.1.

The engineering of g-factor in single quantum wells is therefore possible at design time, but it would be ideal if the system could be fine tuned in-situ to maintain particular values (such as zero). This is possible through the use of electric fields.

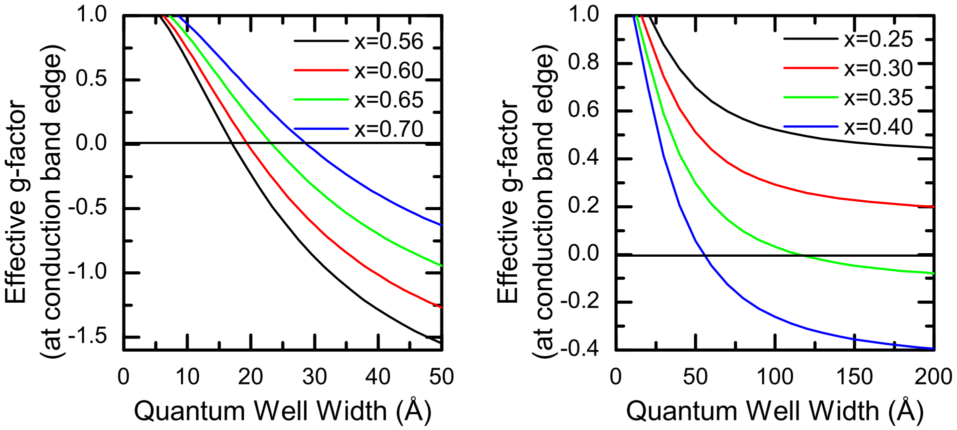

(a) $In_{1-x}Ga_xAs$ (b) $InAs_xP_{1-x}$

Figure 7.1: Simulated variation of effective electron g-factor with quantum well thickness for two ternary alloys, based on simulation codes developed at the National Research Council by Geoff Aers.

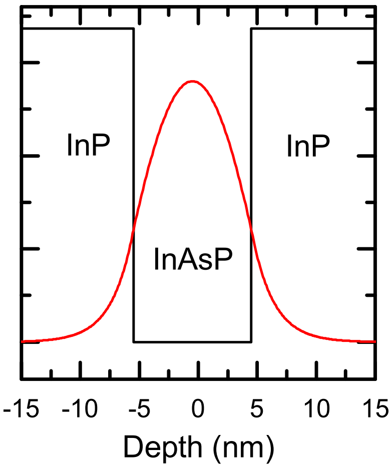

Figure 7.2: Ground-state electron wavefunction of a quantum well (here, for example purposes, InAsP in InP). The effective g-factor of the electron receives contributions from the well and the barrier, depending on the extent of the wavefunction's overlap with each.

7.2 g-factor Engineering with Double Quantum Wells: Electric Field Effects

Samples grown by epitaxial processes offer great flexibility. Material composition can be varied continuously through the structure, resulting in a slanted quantum well, Double Quantum Well (DQW), or DQW with a different composition in each well. All of these cases are interesting for promoting wavefunction penetration into the barrier material.

However, it is under the influence of an electric field that these techniques achieve their full potential. We have run simulations to solve for the ground state wave-function of a DQW with arbitrary composition, according to models of material parameters developed previously at NRC. In a DQW structure where each well has a different composition, the effect of an electric field is to tune the balance of occupation of one well or the other by raising the electric potential drop across the DQW structure. This has the effect of forcing the electron to take on more of the character of one well at a particular field, and of the other at the opposite field. This enables not only control of the g-factor, but dynamic control of the g-factor at will. If quantum dots can be engineered which are compatible with this technique, gate-controlled fine-tuning of their g-factors may be possible in an experimental setting. This may become the basis for full Bell measurement and photon to spin conversion, discussed in sections 5 and 6.

Figures 7.3a and 7.3b present plots of the ground and excited state wavefunctions of a DQW as a function of perpendicular electric field, as computed in simulation. Figure 7.3, meanwhile, is a plot of the g-factor of the two wavefunctions as a function of that same electric field. For this design, which makes use of two quantum wells of different composition and width, the g-factor can be dynamically tuned over a range of values including positive and negative values using realistic electric fields from a global gate.

In addition to allowing fine-tuning to the zero g-factor regime, which is particularly relevant to section 5, this technique could allow quantum dots in an ensemble to be made dynamically addressable. This means that any set of quantum dot spin qubits could be brought in or out of resonance with a waveguide, cavity, or oscillating electrical/magnetic field as needed. This is an attractive property from the point of view of dynamically coupling and decoupling distant spin qubits in a quantum processor.

Obviously, for this application, noise would be introduced into the g-factor by the electrical noise in the controlling field. Electrical noise already exists in spin qubits which are defined by electrostatic gates, so one must compare the first derivatives of the relevant hamiltonian components to see if this noise is important.

The magnitude of the electrically-induced noise in the Zeeman term should be, in a linear approximation, $\mu_B B \frac{dg}{dE} * \Delta E$, where ΔE is the noise in the applied voltage E. Given the situation of figure 7.3, one expects the noise in the Zeeman term to peak at about $100\,\mathrm{neV\,mV^{-1}}$ across the quantum well for a 1 T applied voltage when the g-factor changes most quickly. If the noise in the applied voltage is less than $100\,\mathrm{\mu V}$, the noise in the Zeeman term is less than $10\,\mathrm{neV}$.

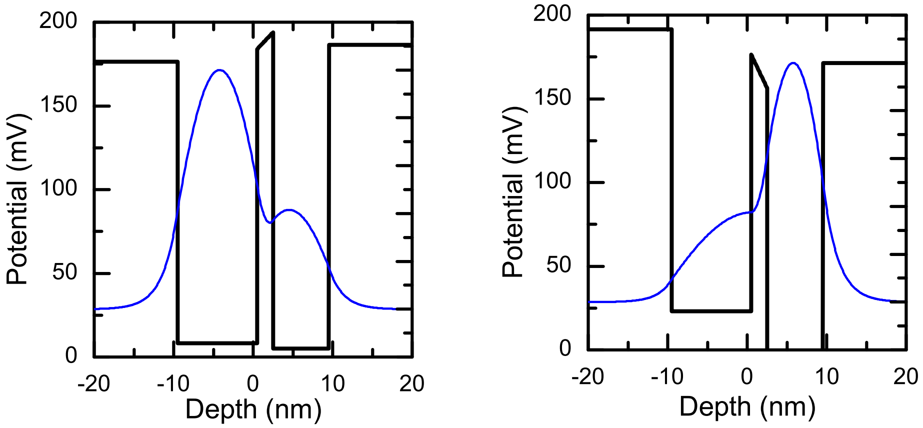

(a) With the left quantum well lowered by 10 mV*, the electron mostly resides in the left well.*

(b) With the left quantum well raised by 20 mV*, the electron mostly resides in the right well.*

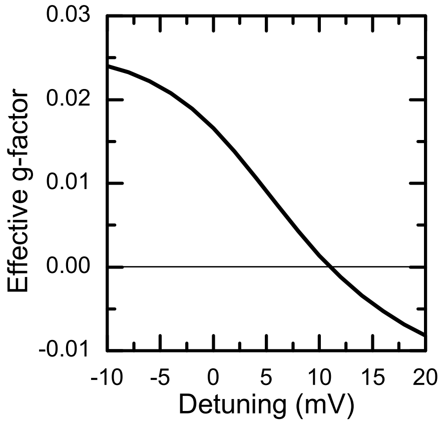

(c) Effective ground state g-factor with respect to the mismatch, controlled by the bias voltage, between left and right quantum well energy. A positive value indicates a raising of the left well potential.

Figure 7.3: Simulation of ground state eigenfunctions and effective g-factors in a double $InAs_xP_{1-x}$ *quantum well with the following parameters: two quantum wells of width* 10(7) nm *and composition* $x = 0.35(0.38)$ *for the left (right) well respectively, separated by a* 1 nm *InP barrier. A variable electric field detunes the quantum well energies with respect to one another. For the purpose of the simulation, the electric field is not screened by the barrier material, leaving the precise origins of the electric field out of the model.*

7.3 Summary

The effective g-factor in a quantum well is dependent on several controllable factors, including the width and composition of the quantum well. In particular, the g-factor of electrons in a double quantum well, where the two quantum wells have different compositions, can in principle be fine tuned with an applied electric field by pushing electrons from one well to the other. The fact that InP and InAs have bulk g-factors that differ in sign enables to preparation of a zero g-factor quantum dot sample. Electron spins in such a material would be subject to only very small Zeeman perturbations.

- Experiments could be conducted in a regime where the electron magnetic moment is smaller or comparable in magnitude, relative to nuclear magnetic moments.
- Spin qubits in the small g-factor regime would be less strongly influenced by the nuclear spin bath, which often limits experiments with spin qubits in quantum dots[12].
- Coherent transfer of quantum information from a single photon into a single electron is possible in this regime (section 6).
- Non-destructive Bell measurement can be performed in the small g-factor regime by making use of the degeneracy of the spin triplet and the entangled ground state, in the g=0 regime (section 5).

The last two consequences are certainly important from the perspective of quantum repeater technology, as we have seen in previous sections, which is why this work focused on the InAsP material system and evaluation of quantum dot fabrication techniques with g-factor engineering in mind. The next section will discuss a class of nanowire devices which were intended for service as scalable optically active spin qubit registers, in which we have formed quantum dots.

Chapter 8

CBE Nanotemplated Nanowire Technology

At the National Research Council, an initiative was commenced to form quantum dots in InGaAs and InAsP nanowires[50]. These two materials were chosen for their large (InGaAs) and small (InAsP) electron g-factors, respectively. The goal of the project was to develop a scalable means to fabricate arrays of optically active quantum dots for use in quantum information processors.

For reasons which will be discussed, the composition and width of the quantum well embedded in a CBE templated nanowire ridge varies with the shape of the template given a fixed growth sequence. This offers a means to create an array of devices with differing g-factors by manipulating the geometric parameters of the devices at design time.

One advantage of nanowire structures, and the principal motivation for their study, is that they require electrostatic confinement only in one dimension. Numerous successes in spin qubit experiments have so far emerged from studying lateral devices fabricated from GaAs/AlGaAs 2DEG structures, but the number of electrostatic gates required is a source of practical difficulty. It is particularly difficult to scale such two-dimensional structures.

8.1 Fabrication Process

The fabrication of nanowire ridges on an InP substrate is performed in the following steps:

1. A SiO_2 layer is deposited on an InP substrate and patterned with rectangular openings by electron beam lithography, combined with a wet etch. Typically, many long, thin rectangular windows with different widths are etched to maximize the probability that a device is produced which possesses suitable characteristics.

2. A trapezoidal ridge of InP is grown in the template by Chemical Beam Epitaxy (CBE). The ridge side-walls follow the 011 crystal plane of the InP.

3. CBE continues, and a Si doped InP layer is deposited.

4. A buffer layer of InP and the conductive $In_xAs_{1-x}P$ or $In_xGa_{1-x}As$ layer are deposited. Carriers from the silicon donors populate the quantum well created by the ternary alloy.

5. An InP cap layer is deposited, and the CBE portion of the process is now complete.

6. Ohmic contacts are formed by annealing an alloy of Au and Ge at either end of the ridge. These are used to supply current for transport experiments.

7. Electrostatic gates, composed of nickel and gold, are deposited on the surface of the InP ridge.

Ridges grow from the InP base and taper along the 011 facet of the crystal. The ridge therefore generally resembles a trapezoidal prism as shown in figure 8.1a. The diffusion length for the deposited material is long on the side facets, and short on the top face. Therefore, material tends to settle on the top face when available, causing the ridge to grow upwards rather than swell in all directions equally.

As growth continues, the top face continues to shrink until it vanishes completely (figure 8.1b). Beyond this point, material begins to accumulate on the side-walls to form an encapsulating layer.

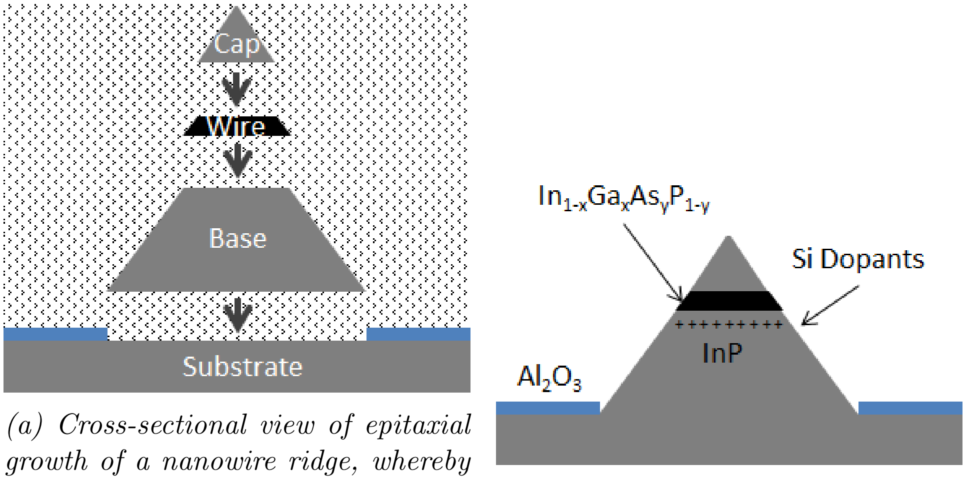

(a) Cross-sectional view of epitaxial growth of a nanowire ridge, whereby three layers of material grow in the presence of a chemical beam of variable composition. The base, wire, and cap are grown in that order within the lithographically defined trench.

(b) The finished nanowire ridge. If growth is allowed to continue, the exposed sides of the structure will swell with InP.

Figure 8.1: Stages of nanowire ridge growth by chemical beam epitaxy.

8.2 Cap Layer Measurement

In order to measure the size of the cap layer, an experiment was conducted on an array of ridges grown with varying base widths. The apparent width of the resulting devices was measured from SEM images.

The difference between the apparent width and the design width is due to the presence of the overgrown cap layer. Figure 8.2 shows the geometric relationship between the cap layer and the original base width, while 8.3 presents the apparent widths from the SEM images.

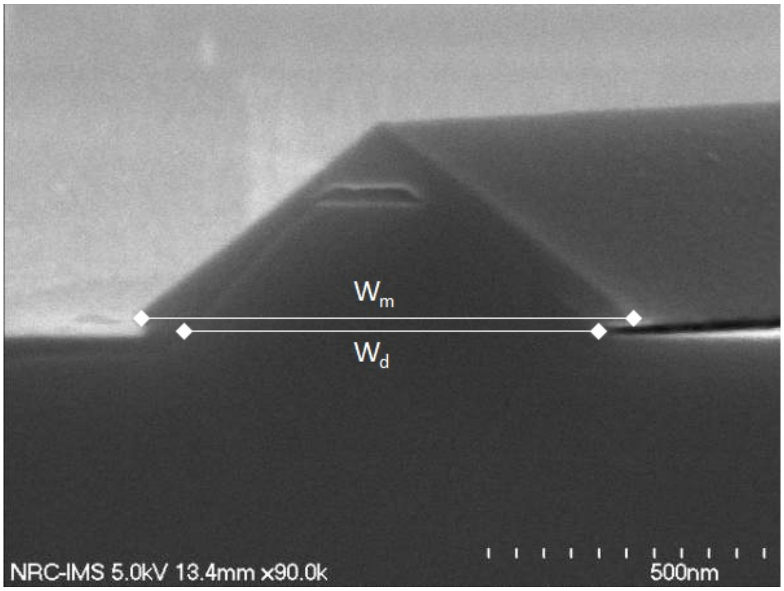

Figure 8.2: The difference between the measured base width (W_m) and the designed base width (W_d) is $\Delta W = W_m - W_d$. The thickness of the cap layer (t_{cap}) is not simply the difference between the two, but rather the distance between the sidewall planes. It can be estimated by $t_{cap} = \frac{W_m - W_d}{2\sqrt{2}}$.

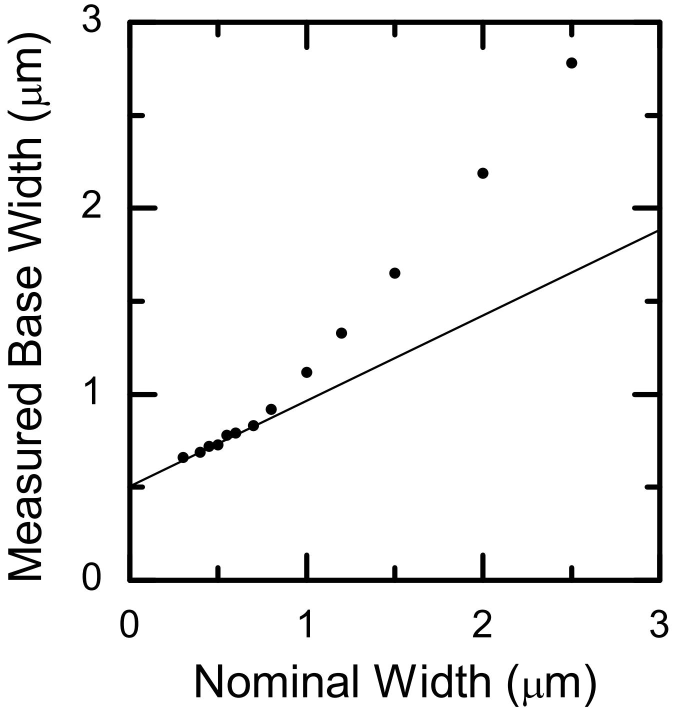

Figure 8.3: Real base widths for ridges fabricated with different design base widths, imaged by SEM microscopy. The relationship between the measured base width and designed base width changes abruptly at a design base width of 750 nm. For smaller ridges, the rate of change of measured width with respect to designed width is halved. This indicates that these ridges have grown widthwise beyond their design width. This is expected for narrow (and therefore short) ridges, whose cross-sections are triangular rather than trapezoidal.

8.3 Gate Fabrication Outcomes

In order to form quantum dots in ridge nanowires, electrostatic gates are required to modulate the potential. These are fabricated by depositing metal, usually gold, onto the ridge surface as in figure 8.4a.

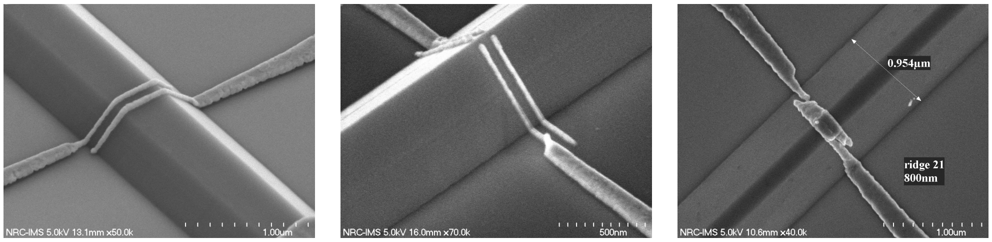

(a) Apparently successful gate fabrication. *(b) Gate broken at the peak of the ridge.* *(c) Two gates fused together.*

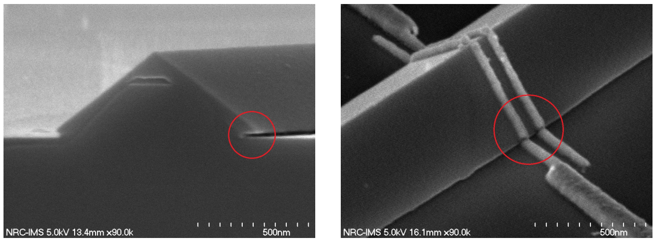

(d) Gap between ridge sidewall and substrate. *(e) Gate broken at the base of ridge due to gap.*

Figure 8.4: SEM images of the most commonly observed damage to gates.

Problems were detected with the fabrication of gates. In particular, since the gates must be made very thin for the required precision, gates are very sensitive to breakage during deposition and photoresist removal. While this can be counteracted somewhat by self-adhesion of the gold, if the gates are deposited on the sharp peak of a completed ridge a succeptability to breakage has been observed as in figure 8.4b.

Gates can also suffer from breakage at the base of the structure, where the InP cap layer can extend over the photoresist layer. A gap is therefore created where there is a step between the ridge edge and the InP substrate after removing the oxide mask. See figures 8.4d and 8.4e, where the gate discontinuity is evident at the ridge edge.

Testing of fabricated gate characteristics was first performed at room temperature, using a probe station. The gates are expected to form Schottky barriers between themeselves and the nanowire semiconducting material embedded in the ridges. At room temperature, the corresponding I-V characteristics of a Schottky barrier are therefore expected from functional gates. If current does not flow in at least one direction, or if current flows ohmically, it means the gate does not work as expected and is probably broken (in the former case) or fused to the nanowire (in the latter case). Furthermore, attempts to pass small currents between gates can reveal gates which are fused together (figure 8.4c).

The often repeated experimental procedure to assess the gates of each ridge was to ground one ohmic contact and apply varying voltages up to hundreds of mili-volts of forward and reverse bias. Current, which was limited to nano-amps, was measured. The typical Schottky I-V characteristic was often observed, and the characteristic resistance ($R_0 = \frac{dV(I=0)}{dI}$) was calculated.

In some cases, the gate to ground I-V relationship was completely ohmic over the observed range. In those cases, the resistance indicated the cause. Resistances of many giga-ohms, comparable to the substrate resistivity over such distances, indicate that the gate is probably broken either at the base of the ridge or before reaching the ridge at all. Resistance values in the kilo-ohm range, comparable to the resistance of the nanowire, indicate a short between the gate and the nanowire. Shorts between gate and nanowire were relatively uncommon, occuring in less than 5% of samples.

Shorts between gates were identified by attempting to pass current ($< 1nA$) between gates. At least one batch was plagued with many fused gates, but this was not common in other batches.

Breakage in a gate at the peak is more difficult to detect at room temperature, since the Schottky barrier should still exist. All things being equal, the characteristic resistance of the Schottky barrier should be higher in that case, since the contact between the gate and the ridge is less by a factor of two. However, the characteristic resistance fluctuated somewhat wildly between gates (depending on the quality of Schottky barriers) that were apparently quite similar under SEM imaging. It is therefore difficult to be confident about the cause of such a fluctuation.

In principle, many of these problems could be detected by direct SEM imaging of the samples before cooling. Unfortunately, SEM imaging influences the concentration and mobility of the sample through exposure to high-energy electrons. This degrades the quality of the 2DEG. Because of this, samples intended for cooling were screened primarily through the probe station.

Incidences of breakage were commonly identified at room temperature. It was found that breakage consistently occurs in narrow ridges within a batch, but not in wide ridges. Based on the IV characteristic, hundreds of pairs of gates on hundreds of devices were evaluated. In a particular set of 21 devices, the 11 devices with base widths evenly spanning 150 nm to 550 nm had no functioning gates. The three devices with base widths 590 nm, 630 nm, and 670 nm had functioning gates one one side. The functioning gate was on the same side in all three cases. Finally, the 6 devices 710 nm wide and wider had two functioning gates. This example was typical, and indicated both that the total yield of narrow devices is low, and that the outcome of manufacturing any device is very deterministic.

As the ridge becomes narrow, the proportion of material that goes to growing the cap layer rather than completing the ridge increases. It seems that the larger cap layer is to blame, because narrow ridges have more pronounced caps and peaks, while sufficiently wide ridges have no peak and no cap. The gap between the ridge sidewall and the substrate, which results from an over-grown cap layer, can cause gate breakage through the "mushroom" effect (see figure 8.4e). The peak of a ridge, as shown in figure 8.4b, can also cause gate breakage.

8.4 Electrical Characteristics

Arrays of gated ridges produced by this process were iteratively tested at room temperature to probe their electrical characteristics. Although there are limits to what can be learned at room temperature about a quantum device designed to be operated at sub-Kelvin termperatures, information can be gleaned, and used to generate useful feedback.

For instance, the nanowires should be conductive at room temperature. The ohmic conductivity of each ridge was measured to ascertain whether the ohmic contacts and nanowire had formed properly. Up to 10 micro-volts were applied accross the two ohmic contacts. Current was limited to a few nano-amps, and measured to yield a resistance value.

It was found as expected that the conductivity of each ridge varied with the base width and therefore the width of the nanowire. For sufficiently narrow ridges, the nanowire was expected to form not on the top face of the trapezoidal ridge during growth, but on the sidewalls as in figure 8.6c. In this case, the electrical characteristics of this material were expected to be dramatically different, and this was in fact the case. Conductivity dropped dramatically for narrow ridge structures as shown in figure 8.5.

Ultimately, the ridges must be conductive in order that we be able to perform transport measurements such as Coulomb blockade and Coulomb diamonds. Additionally, the width of the nanowire should be minimal so as to be compatible with few-electron confinement for spin qubit applications. This means that optimal ridges which are near the narrow end but which remain conductive are the most interesting for fabrication of QD structures for quantum information processing experiments.

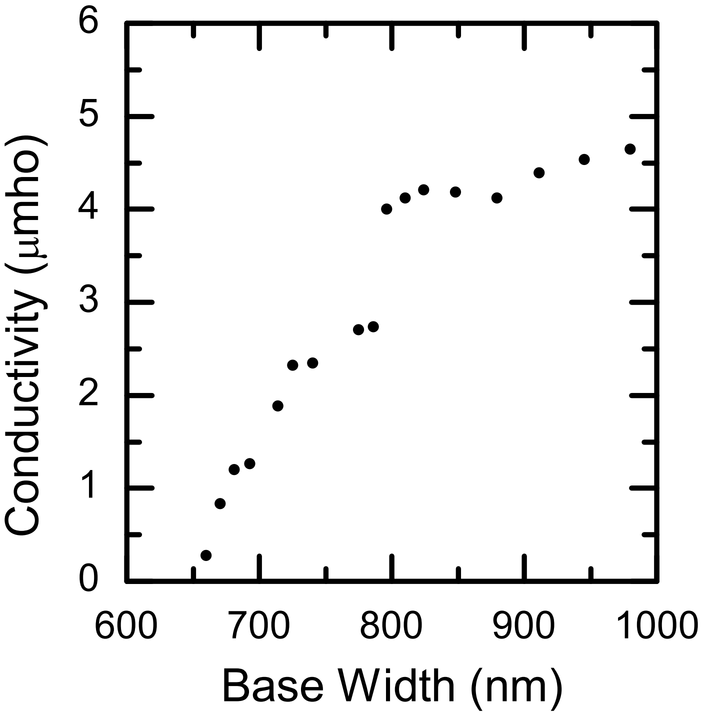

Figure 8.5: Low temperature ridge conductivity measurements for different base widths, at 4 K*. The base width was inferred from the design width and interpolation of the data in figure 8.3. One naively expects a linear relationship between the conductivity and the width of a resistor. The variable height of the wire with respect to base width will confound this trend, and this is caused by material deposited on the sidewalls concentrating at the smaller top face of the trapezoidal ridge during growth.*

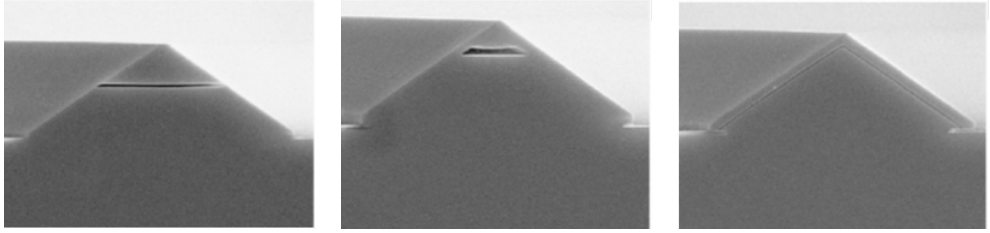

(a) A two-dimensional wire results when a layer of nanowire material is deposited in a ridge that is far from complete.

(b) If nanowire deposition begins when the ridge is nearly complete, the material will concentrate at the peak and result in a more 3 dimensional wire.

(c) A particularly narrow, and therefore short ridge becomes triangular before the nanowire material is deposited. The result is a disordered, nonconductive nanowire.

Figure 8.6: Cross-sectional SEM images of ridges of different widths grown in parallel, showing several outcomes achievable by controlling the ridge base width. Devices are cleaved along the [100] plane and the nanowire is selectively etched away, creating a visible cavity.

8.5 Summary

The fabrication of electrically conductive nanowires in ridge structures for quantum dots is possible. Difficulties lie mostly in the fabrication of gates, which tend to break in various places, including the peak and the base of the ridge, when the ridge is not a trapezoid and has a pronounced cap layer. However, thanks to close collaboration with technologists, the growth process has been continuously modified to increase yields of ridge devices without these properties.

At present, the yield of narrow devices with two or more functioning gates has been low, about 10%. However, the proposed optimization to the fabrication process has the potential to increase yields. A few-electron quantum dot was formed in this type of device, however, and the experiment is described in section 12. The next section will describe experimental methods used in all of the remaining sections of this thesis, which consist of low-temperature electronic measurements on semiconductor samples. Specifically, the formation of quantum dots in InGaAs and InAsP structures, and the probing of scattering processes in a high-mobility 2DEG.

Chapter 9

Experimental Apparatus and Techniques

9.1 Room Temperature Characterization

To perform room temperature electrical characterization of ridge samples and gates, a Micromanipulator model 7000-LTE probe station with Agilent 4155C semiconductor parameter analyzer was used for two-point measurement. Unless stated otherwise voltage was applied and current was measured and limited by the analyzer.

9.2 Cryogenics

All other experiments were performed at low temperatures using an Oxford Instruments 3He variable temperature cryostat with split coil 5T magnet. The holding time, at the base temperature of about 250mK, was more than 24 hours. Cryostat wiring consisted of fine copper loom and room temperature RC filters to ensure low noise measurements. The sample socket allowed for > 90 degrees of rotation to enable free circular control of the static magnetic field. The sample mounting allowed for measurements in parallel or perpendicular magnetic field, tilted in-situ.

When microwave excitations were required, a 1mm antenna was mounted on the sample holder and connected to one of the cryostat's high frequency transmission lines.

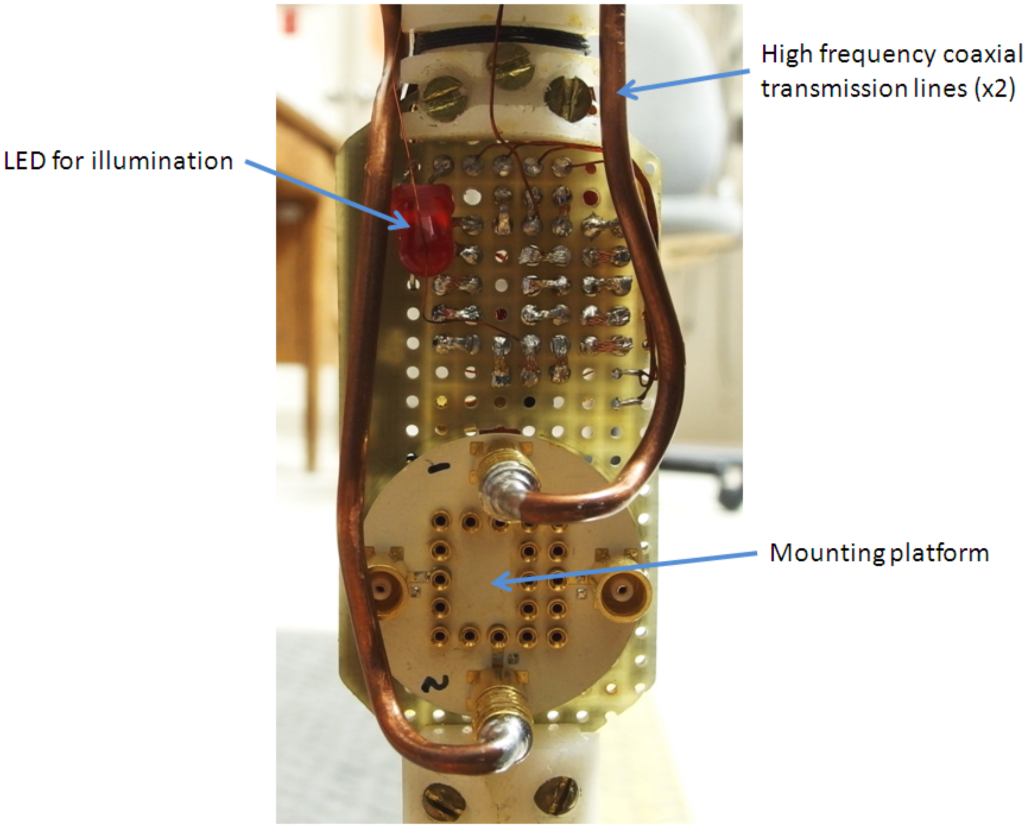

Figure 9.1: Cryostat sample socket

9.3 Electronics

An AVS-47 low noise temperature analogue resistance bridge was used to measure four-point resistance with AC voltage excitations always below the thermal energy k_BT, and typically about $10\mu V$. Refer to figure 9.2a.

An SRS-830 digital signal processing lock-in amplifier was used for two-point measurements to reduce noise when the current through the sample was less than could be detected by the AVS bridge ($> 1M\Omega$). In this case, an Ithaco 1211 current preamplifier was used before the lock in amplifier. These measurements followed the circuit in figure 9.2b.

Gate voltages were applied by several IOtech DAC488HR/4 digital to analogue converters.

All measurement devices listed above output voltages representing measured values. These voltages were finally digitized by Agilent 3458A digital multi-meters.

Microwaves, when required, were produced by an Anritsu 69377B synthesized signal generator.

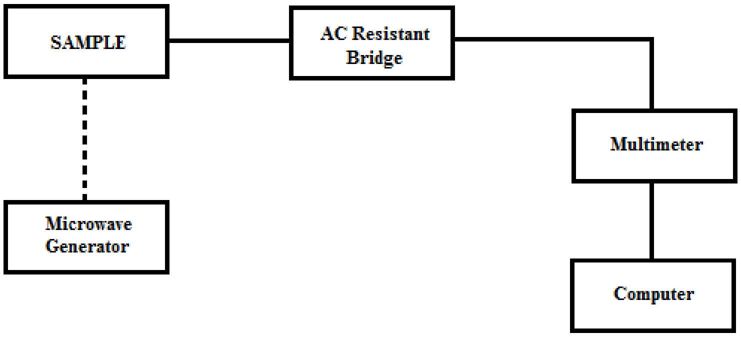

(a) For low resistance ($< 1M\Omega$) measurements, a 4-point resistance bridge was used. For measuring Microwave Induced Resistivity Oscillations, a source of microwaves was also used.

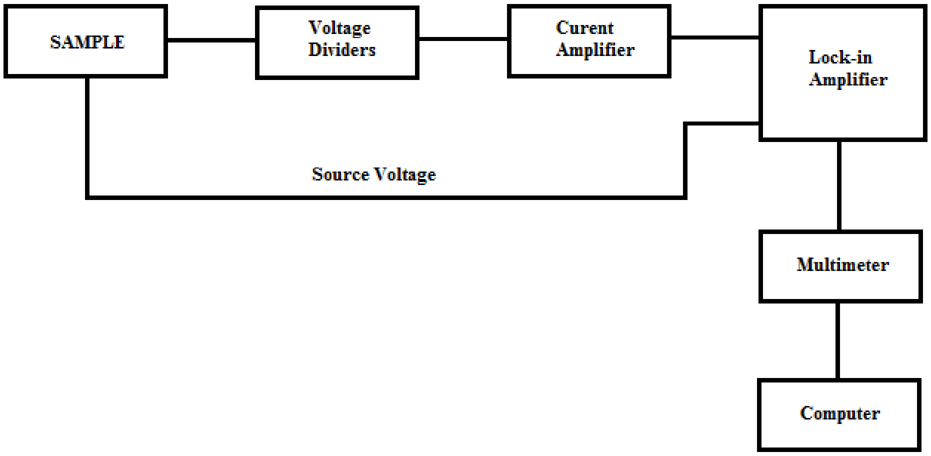

(b) For high resistance measurements, such as quantum dot transport, a current preamplifier and lock-in techniques were employed.

Figure 9.2: Measurement configurations employed for low-temperature experiments.

9.4 Software

For the purposes of efficient and automated control of instruments, original software was written and modified by the author in both the Labview and Python programming languages, including a modular automated instrument controller suite which can explore an experimental parameter space and is expandable by plugins to support additional equipment.

The modular instrument control program controls generic instrument objects, which each expose multiple channel objects to the controller.

Channel objects represent inputs and outputs of devices. They can be inputs, outputs, or both. Channel values can be changed automatically, as opposed to plugin and device settings (which are only manually configurable). Examples of output channels might be: amplitude, frequency, and phase of a sine wave output, the set point and sweep rate of a superconducting magnet power supply, or one or more shape parameters of a waveform from an arbitrary waveform generator. Examples of input channels might be current and voltage values, temperature, or the amplitude and phase of the input signal to a lock-in amplifier.

The instrument controller can deal with each channel in an abstract way, since the code which actually triggers measurement and adjustment of device state is hidden from the controller in the form of a plugin. This allows the experimenter to explore the space of possible experimental conditions by repeatedly sweeping a set of channels, for example gate voltage, and step some other channel in between sweeps, for example magnetic field, without writing a new script to control the automation.

Chapter 10

Forming a GaAs Double Quantum Dot

Experiments with electrostatically defined lateral quantum dots in GaAs/AlGaAs are common, and techniques are established for dealing with this material system. As an exercise, measurements were performed on such a double quantum dot. The steps were documented here, and the process and data will be useful to compare with section 11 to help explain the observations contained therein.

To begin, a GaAs/AlGaAs 2DEG is patterned with electrostatic gates in the device geometry of figure 10.1.

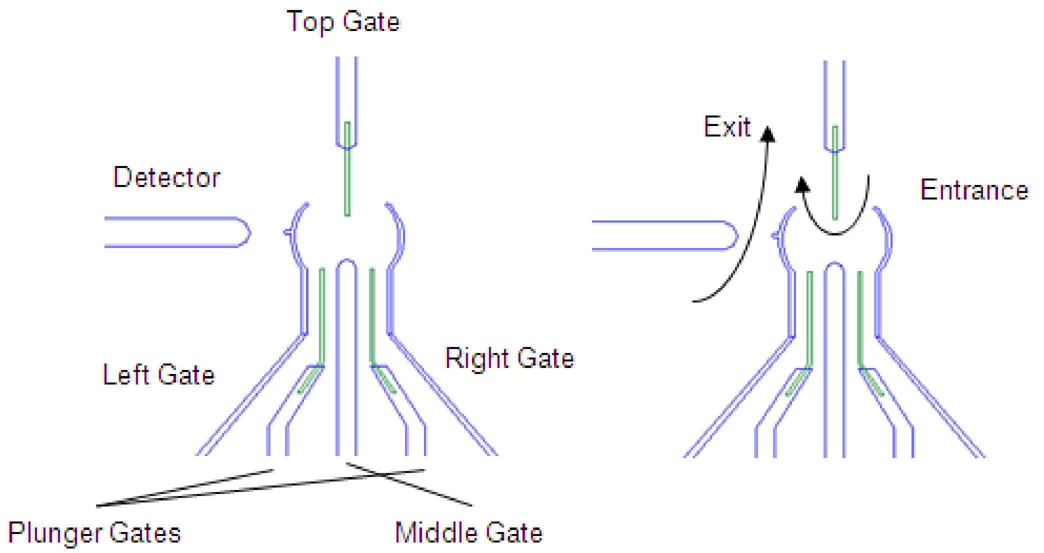

Figure 10.1: Lateral double quantum dot template and intended current flow through the energized device. Current may flow through the quantum dot by quantum tunnelling, and a separate current may flow through the QPC for indirect charge detection.

10.1 Single Gate Tests

The initial measurement confirms that each gate has a depleting effect on the 2DEG. The main gates will here be called the left, top, and right gates in accordance with figure 10.1. As each gate is energized, the section of 2DEG under that gate is expected to smoothly become an insulator, raising the resistance of the sample.

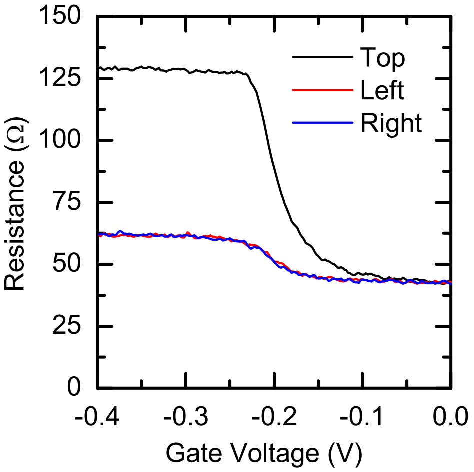

Figure 10.2: Single gate depletion curves at 1.5 K*. At the depletion threshold, in this case approximately* $-0.2\,\mathrm{V}$*, the area under the gate becomes an insulator. The sample resistance therefore increases as current is redirected.*

10.2 Entrance and Exit QPCs

Once each gate is independently tested, gates are energized in pairs to create QPCs. The intent is to measure QPC characteristics and the maximum negative voltage at which pairs of gates will admit current between them. Figure 10.3 is an example such a measurement, showing both QPCs pinching off at about -0.7V. Since the pinch-off voltage (-0.7 V) is lower than the depletion voltage for each gate (-0.2 V), we can be confident that a QPC is actually being formed. If the pinch-off and depletion voltages are the same, this is called pinch-off at depletion. The likely cause is too little space between the two gates of the QPC, so that a barrier forms at depletion rather than a channel which can be constricted to form a contact.

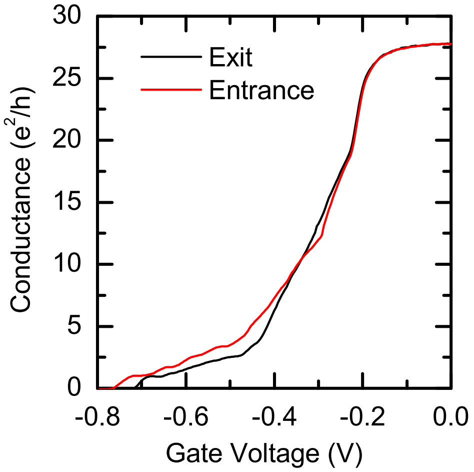

Figure 10.3: QPC conductance curves for the entrance and exit QPCs at 1.5 K*. The "pinch-off" point, where the conductance drops to zero, is roughly* −0.7 V *for both QPCs. Depletion of each individual gate occurs at* −0.2 V*.*

10.3 Barrier Balance and Coulomb Blockade

The next step is to form the quantum dot by energizing all of the gates. The initial voltages are chosen to be greater than the depletion thresholds for each gate, and such that the entrance and exit barriers are closed. The left and right gate voltages can then be varied to open the QPCs slightly and hopefully observe Coulomb blockade oscillations in the conductivity of the sample as in figure 10.4. This way, the point where both QPCs just pinch off can be measured and the symmetry of the entrance and exit tunnelling barriers can be evaluated.

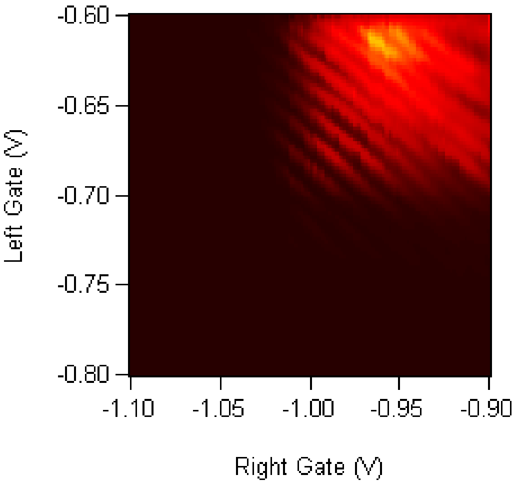

Figure 10.4: Current through the quantum dot for varied left and right gate voltages at some fixed negative gate voltage on the other gates. The appearance of Coulomb blockade peaks indicates the formation of a dot, while the diagonal orientation indicates the position relative to the left and right gates. In this case, the dot appears equidistant from both based on the slope of the addition lines. The threshold at which current is completely suppressed are not equal between the two gates, indicating asymmetry in the tunnelling barriers which couple the dot to each lead.

10.4 Double quantum dot transport and charge detection

With further adjustment of the other gates, the quantum dot in this particular device can be split to form a double quantum dot. In particular, a more positive (yet absolutely negative) voltage on each of the two small plunger gates and a more negative voltage on the middle gate (see figure 10.1) can force electrons to occupy two separate smaller dots rather than one large dot. In this regime, transport experiments become more difficult and charge detection becomes useful because quantum dots which are not directly coupled to both leads will pass current only at the so-called triple points, as discussed in section 3.

GaAs devices have been and are a popular choice for spin qubit experiments due to the well-tested nature of the platform, and it is a useful test-bed for quantum information technologies. For example, we participated in an

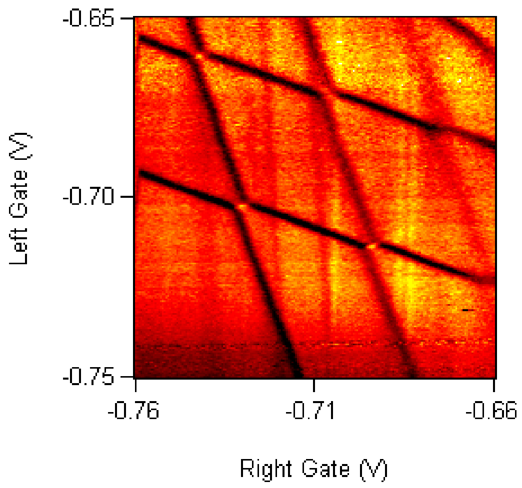

Figure 10.5: Horizontally differentiated current through a charge detection QPC, comprising the charge stability diagram of a fully formed double quantum dot (recall section 3.6, where the stability diagram was introduced).

experiment with a triple quantum dot device in which enhanced spin to charge conversion was observed through the use of an excited state as an intermediate which featured more pronounced charge deformation, translating into more visibility due to increased action by the electron charge on the QPC[55]. Many concepts, including that technique and the techniques we have illustrated here, can in principle be translated into other platforms. For example, in the next section, experimental characterization of the InAsP material fabricated at NRC will be presented, following this technique for creating quantum dots.

Chapter 11

InAsP Material Characterization

In principle, the InAsP material has several advantages over GaAs for hybrid photon/spin qubit applications, some of which were discussed in previous theoretical review section. In this section, techniques commonly used to form and study GaAs quantum dots for spin qubit applications were applied to InAsP-based devices. The goal was to form an electrically controllable few-electron quantum dot in this material.

11.1 Characterization of Planar Material

Fabrication of InAsP devices is not yet routine in the NRC nano fabrication lab, and characterization of the products was called for. Of particular interest was an electrical probe of the low-temperature carrier concentration and mobility, as well as responsiveness to light and an inspection for any undesirable conduction pathways between fabricated test gates and the 2DEG.

Carrier concentration and mobility were measured using standard techniques based on the observation of the Hall effect in a static magnetic field applied perpendicular to the plane of the 2DEG, and again after a brief illumination with red light from an LED. The sample more than doubled its carrier concentration after illumination to $1.7 \times 10^{12}/\mathrm{cm}^2$ and increased its mobility to a maximum of $2.86 \times 10^5 \mathrm{cm}^2/V \cdot s$, which indicates reasonable quality.

No conduction was observed between the test gates and the 2DEG, though

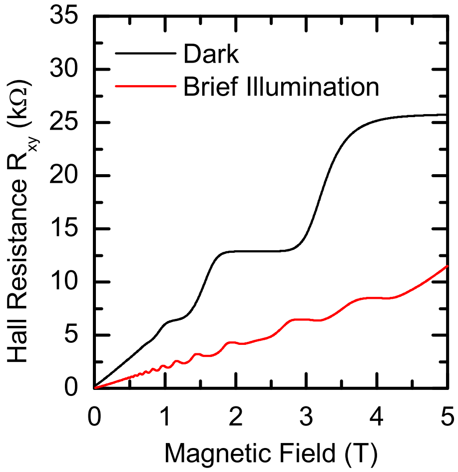

Figure 11.1: 1 Kelvin characterization of a particular InAsP 2DEG sample before (and after) a brief 1 second illumination with a red LED. From the theory of the Hall effect we know that the average slope of this curve equals $\frac{1}{e \cdot n}$, *from which we can calculate that* $n = 6.76(17.2) \times 10^{11}/cm^2$ *is the carrier concentration. By definition, electron mobility is* $\mu = \frac{1}{e\rho n} = 1.14(2.86) \times 10^5 cm^2/V \cdot s$. *This indicates a material of reasonable quality.*

they were observed to have a gating effect on the device.

11.2 Quantum Dots in an InAsP Ridge Structre

Nanowire ridge structures were fabricated using InAsP as the nanowire material. In order to evaluate the system for quantum dot formation and eliminate the difficulties discussed in section 8 with gate breakage, ridges with bases 4 μm wide were initially used. The gate structure was intended to form lateral quantum dots much as they would be formed in a 2DEG, since the wide but thin nanowire resembled a typical 2DEG. This would make the initial quantum dot devices more comparable to split-gate structures in GaAs, which are successful and well understood.

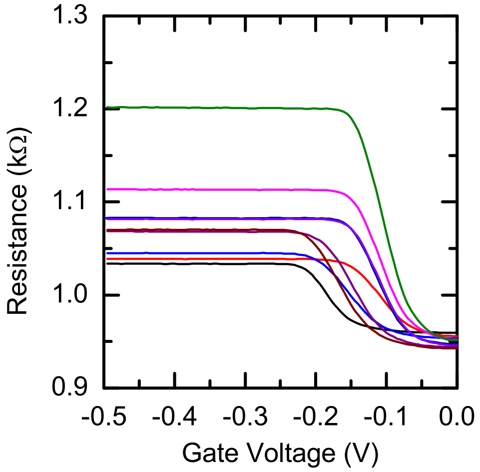

Figure 11.2: Resistance measurements as a function of gate voltage for several gates. Carrier depletion under the gates causes a change in resistance, as expected.

Gates were tested, and depletion was found to occur at about -0.15 V for all gates (see figure 11.2). Attempts to form QPCs and quantum dots in the chosen sample revealed the existence of unexpected conductance fluctuations. Figure 11.4 shows transport measurements where current fluctuations are clearly visible with respect to the voltages on each gate. Two sets of oscillations are visible, and depend only on the voltage of one gate (the left or the right). A third set is clearly visible, but they oscillate (slowly) with

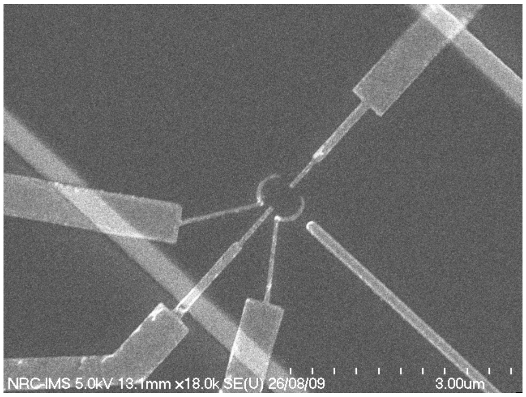

Figure 11.3: Scanning electrom microscope image of the wide InAsP ridge device with lateral gate pattern and QPC.

the sum of the left and right gate voltages and (quickly) with the middle gate voltage. See figure 11.4.

These measurements alone were insufficient to determine the origin of these fluctuations, but a hypothesis was suggested that incidental quantum dots were forming under the gates and that the fluctuations were the result of tunnelling through these dots (see figure 11.4). If this is correct, a treatment would be to increase the width of the gates to ensure that tunnelling cannot occur through these dots.

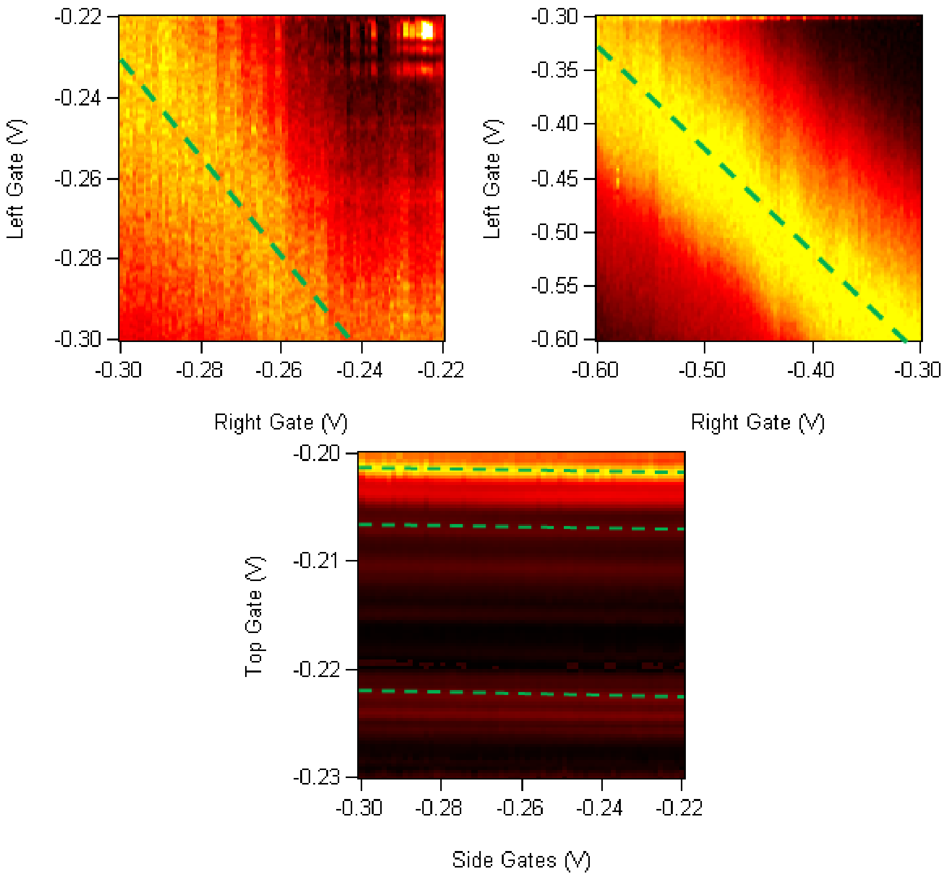

Figure 11.4: Current fluctuations were observed in this device, consisting of gates patterned on an InAsP ridge. Three distinct groups of fluctuations are evident. One set of fluctuations depends strongly on the left gate voltage, another on the right gate voltage, and a third depends equally on both gates (green dashed line, top right). This is consistent with quantum dots forming under the left, right, and top gates respectively.

11.3 Planar Tests

To confirm this hypothesis, planar InAsP heterostructures were grown and a series of different QPCs were fabricated on the sample surface for convenient testing. Each QPC featured a different spacing between the two metallic gates. With ohmic contacts on either side of the sample length-wise, a voltage bias accross the sample permitted current to flow through all of the QPCs in series. By energizing only one QPC at a time, the electrical characteristics of each could be examined separately.

It was expected that gate depletion would cause a sharp increase in the measured four-wire resistance of the sample as the gates were energized. Following this, as voltage became more negative, the resistance was expected to either form QPC conductance plateaus or, due to finite temperature, simply increase sharply at some critical gate voltage. The different spacings in each QPC were expected to translate into a different critical voltage. The intention with this experiment was to calibrate the widths of QPCs in later quantum dot devices. Two important effects were observed over the course of these measurements.

First, the QPCs followed the same depletion pattern in defiance of the expectation that each would have a different threshold voltage and that the differences in the gap between the gates varied substantially: 150 nm to 250 nm. This can be seen in figure 11.5.

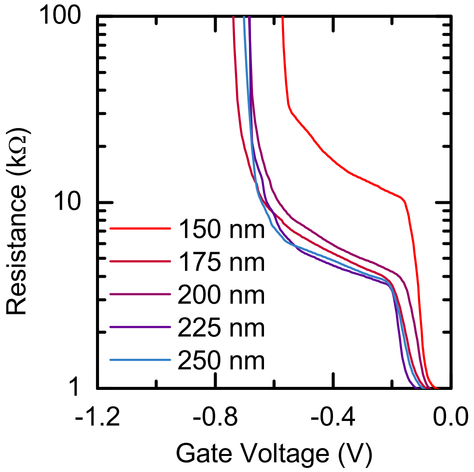

Figure 11.5: 4-wire resistance measurements of QPC depletion at 1 Kelvin. Pinch off occurs after depletion for all QPCs, but there is no difference in the pinch-off voltage depending on QPC width.

Second, Coulomb blockade-like peaks were observed in the transport current as a function of gate voltages. Conductance peaks are not expected in ideal QPC structures, yet they are clearly visible in figure 11.6.

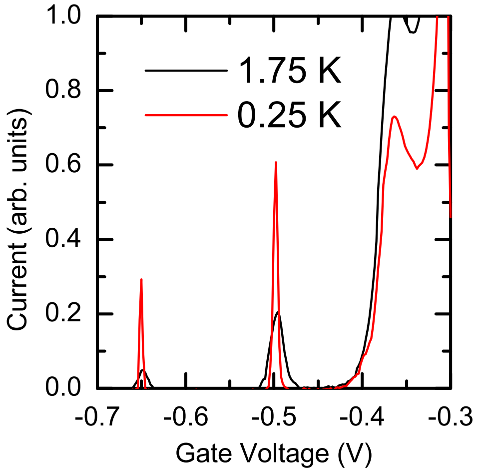

Figure 11.6: Direct current measurements reveal Coulomb blockade peaks in the QPC conductance curve, shown here at 1.75 Kelvin and 250 mK. Their observation lends credence to the hypothesis that the conductance fluctuations in the ridge samples were in fact caused by quantum dots formed under the gates.

Transport measurements as a function of both gates revealed the quantum dots were capacitively coupled to both gates (figure 11.7).

To estimate the charging energy of these incidental dots, a variation of the Coulomb diamond experiment was performed. A small AC voltage was added to the constant DC bias voltage accross the QPC, and the AC component of the current through the device was measured. Instead of measuring Coulomb blockade peaks, the result was a measurement of the absolute differential conductivity as a function of the bias voltage. Instead of widening into conductivity plateaus, Coulomb blockade peaks split into two distinct peaks separated by factor proportional to the DC bias. This occurs because in this scheme the AC component is proportional to the differential of the current with respect to the DC bias voltage, rather than the DC bias itself.

Several different transport diagrams were made with various DC bias values. When the DC bias in volts matched the capacitive displacement of a single addition line or the displacement between two addition lines, the bias voltage was equal to the single-dot charging energy or the inter-dot charging energy due to the capacitive coupling. The charging energy was

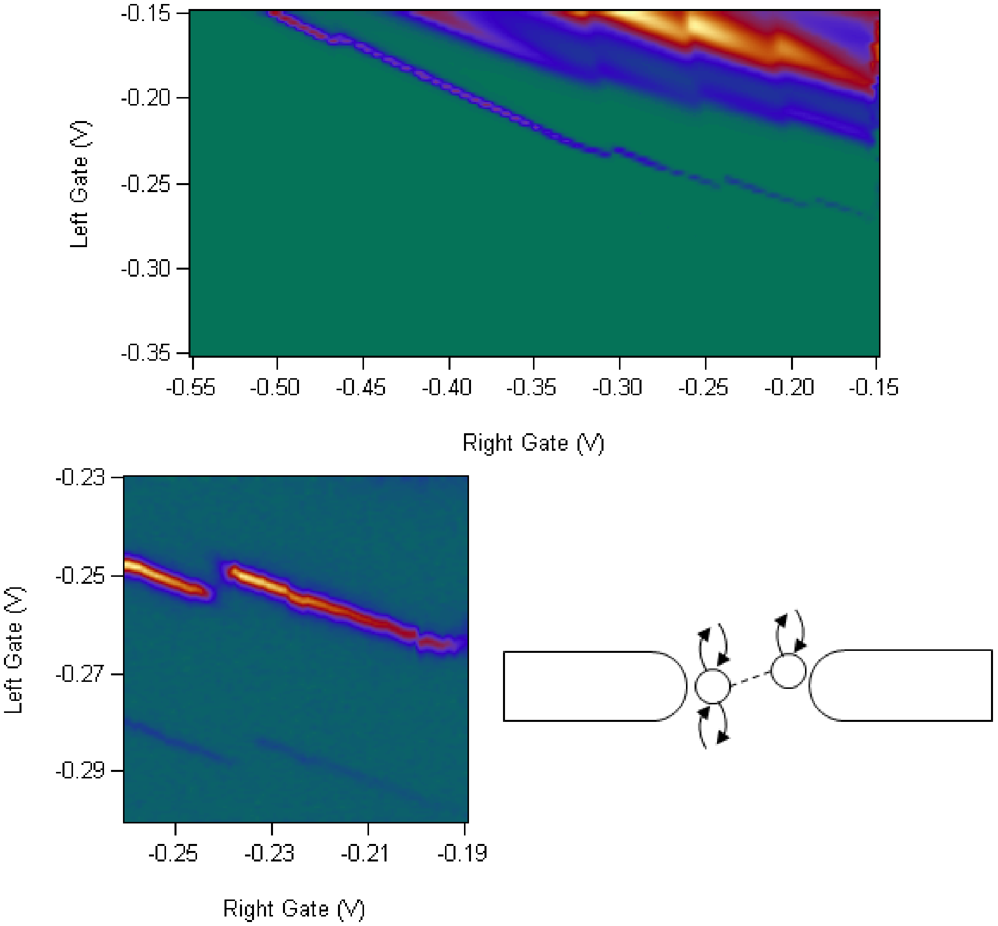

Figure 11.7: Direct current measurements as a function of QPC gate voltages. Coulomb blockade appears dependent on both gates equally, suggesting a dot physically centered between the gates. "Jumps" in the addition lines are consistent with capactive coupling to a second dot through which transport does not occur, possibly due to asymmetric tunnelling barriers, but which is also coupled to both gates.

estimated with this method to be 1.5 meV, and the capacitance of the dot is 1.07×10^{-16} F. Assuming disk-shaped dots, this corresponds to a typical dot radius of 125 nm, according to the self-capacitance formula for a disk: $C = 8\epsilon_{InAsP} r$ (where $\epsilon_{InAsP} \approx 12\epsilon_0$).

Potential fluctuations of similar size have been observed in InGaAs 2DEGs

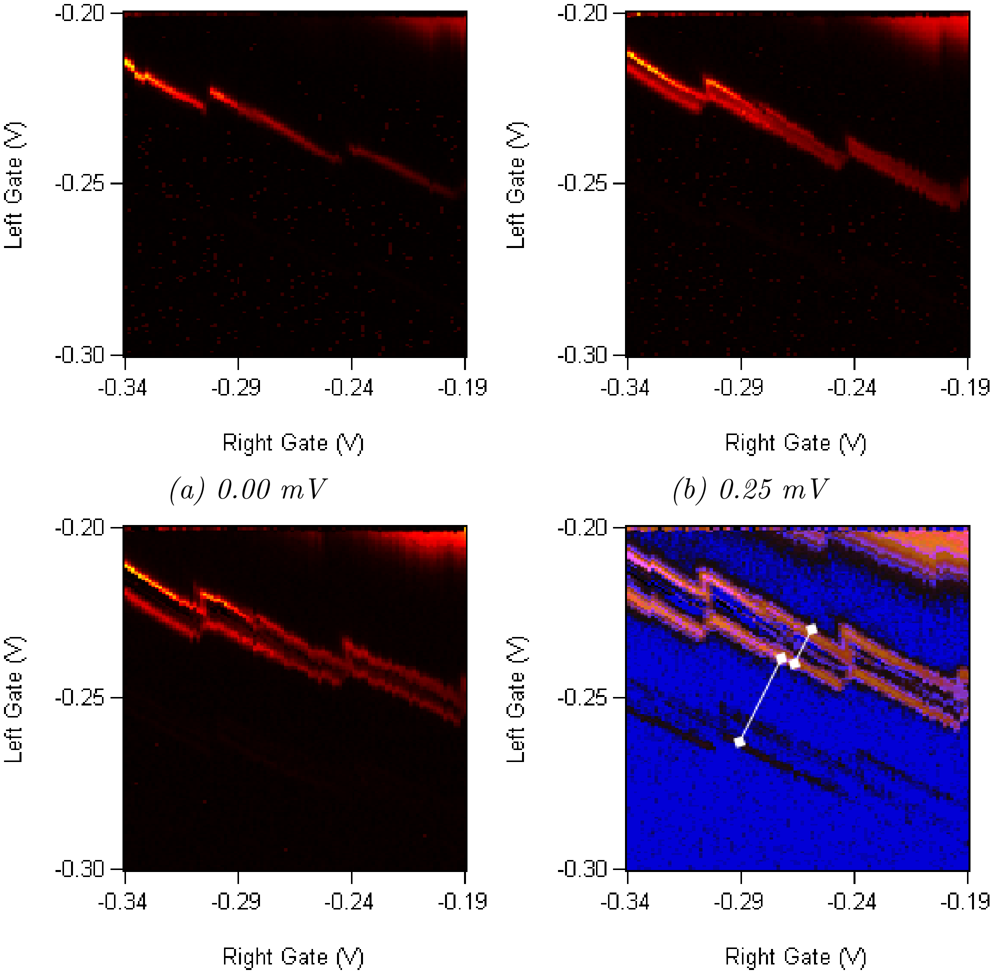

(a) *0.00 mV*

(b) *0.25 mV*

(c) *0.50 mV*

(d) *0.75 mV*

Figure 11.8: Increasing the DC bias voltage across the QPC splits the charge addition lines. At 0.5 mV*, the DC bias splits the lines by exactly as much as the capacitive coupling between the two dots, providing an estimated capacitive energy between them of* 0.5 meV*. The charging energy of the primary dot can be estimated by comparing the inter-dot capacitive jump of 0.5 eV with the perpendicular distance between the two addition lines, for an estimated charging energy of about* 1.5 meV*.*

using a technique called Scanning Gate Microscopy (SGM) [1], and were attributed to disorder in the quantum well material. Scanning Gate Microscopy is the technique of positioning a charged scanning tunnelling microscope tip above a QPC to detect the influence of the charge on the total current through the QPC. The results in the next section challenge that conclusion and suggest an alternative explanation.

11.4 Effects of Surface Oxide

In an effort to determine the nature of the potential fluctuations which produce the observed incidental quantum dots, a second set of QPCs were fabricated with an additional 21.5 nm Al_2O_3 layer between the gates and the 2DEG, to function as a dielectric. Significant changes in device behaviour were observed.

Without oxide, QPCs of various widths achieved pinch-off at the same voltage. This is in stark contrast with theoretical predictions, which suggest that wider QPCs should pinch off at larger voltages. In the samples with oxide, the expected trend was observed (figure 11.9).

QPCs in the sample with oxide pinched off at much more negative voltages: at -0.8 V or more rather than a constant -0.2 V. To some extent this was expected, since the additional di-electric layer reduced the capacitance between the gates and 2DEG. However, theoretical calculations insection 11.5 will show that the magnitude of the change well exceeds predictions.

QPCs with oxide did not exhibit evidence of incidental quantum dots, except occasionally for very wide qpcs.

The 2DEG electron mobility of the oxidated sample was measured to be $\mu = 1.63 \times 10^5 \text{cm}^2/V \cdot s$, compared with the un-oxidated but otherwise identical sample with $\mu = 1.08 \times 10^5 \text{cm}^2/V \cdot s$. The concentrations of the two samples ($n = 2.52$ and $2.56 \times 10^{11}/\text{cm}^2$) compared well. Figure 11.10 shows some of the Shubnikov-de Haas oscillations from which these values were derived.

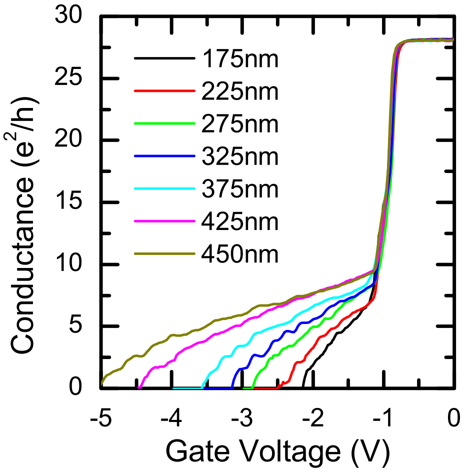

Figure 11.9: QPC conductance curves for QPCs of various widths in a sample with an oxide layer. Note the much higher depletion voltage, compared to figure 11.5, and the dependence of the depletion curve on the width of the QPC. The originally expected behaviour is restored: wider QPCs pinch off at more negative voltages.

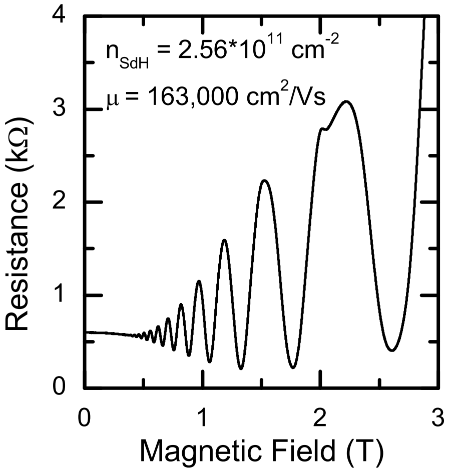

Figure 11.10: Resistance and of the Hall bar sample with the QD (all gates set to 0V) as a function of the magnetic field. Good quality Shubnikov-de Haas oscillations are revealed and used as a standard tool to gain information about the electron mobility and concentration.

11.5 Theory: Surface charge screening

Several clues presented themselves over the course of these measurements. The addition of an oxide layer yielded:

1. A higher electron mobility for the same carrier concentration
2. More negative gate depletion voltage (-0.8 V vs -0.15 V)
3. Expected trend in the magnitude of the QPC pinch-off voltage from narrow to wide QPCs, as is more typically observed in high quality GaAs/AlGaAs QPC structures, for example.
4. Few or no incidental quantum dots in each QPC tested.

A model was suggested that the cause of the potential fluctuations which are responsible for the formation of the incidental quantum dots and which limit the mobility of these samples are in fact caused by disorder not in the 2DEG itself, but in the interface layer between the InP and oxide or InP and atmosphere, as the case may be. In particular, the presence of a large number of trapped charges at the surface interface provides an explanation of all four of these observations, as we shall see.

Figure 11.11 shows the design of the samples, including the gate electrodes and (optional) oxide layer. With the 2DEG grounded and the gate attached to a constant voltage source V, the gate depletion experiment can be treated like a parallel plate capacitor with an offset charge at V=0. To remove the intrinsic charge (i.e. to deplete the electron charges under the gates), a particular voltage V_{dep} must be applied. Based on an approximate dielectric constant of $\epsilon = 12\epsilon_0$ for InP and a design width of 70 nm for the InP layer between the gates and 2DEG, as well as the measured value of -0.15 V for the depletion voltage on the oxide-free sample, the carrier concentration of the 2DEG is predicted to be:

$$n = \frac{\epsilon \cdot V}{d \cdot e} \tag{11.1}$$

$$n = \frac{12\epsilon_0 \cdot 0.15V}{70nm \cdot 1.602 \times 10^{-19}C} \tag{11.2}$$

$$n = 1.42 \times 10^{11}/cm^2 \tag{11.3}$$

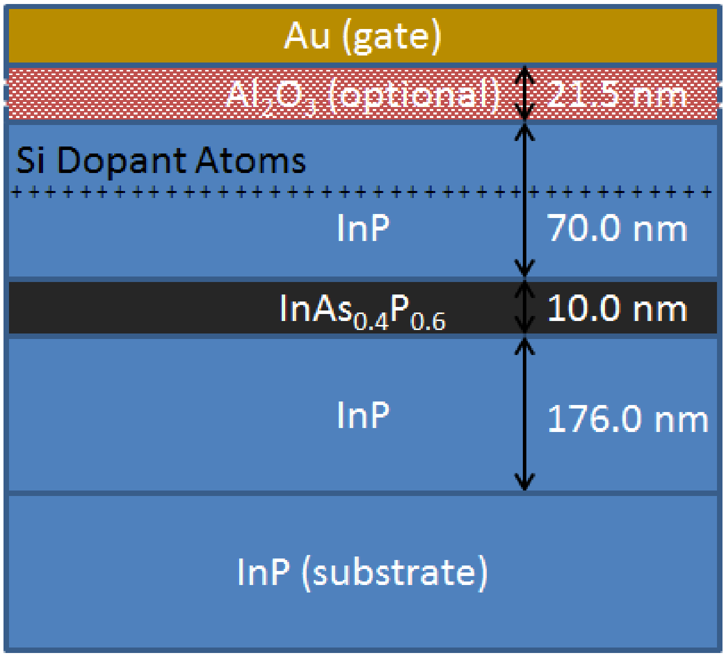

Figure 11.11: Sample composition as a function of depth. The 21.5 nm oxide layer was present only in the second sample.

This is the correct order of magnitude, and it was expected to be somewhat smaller than the measured value because depletion corresponds to the point where electron mobility, as a function of charge density, is nearly zero. This will occur before all charges have been removed[54].

With the addition of an oxide layer, the gate depletion voltage is expected to increase due to the now thicker capacitor. The 21.5 nm of Al_2O_3, with approximate dielectric constant $\epsilon = 9\epsilon_0$ modifies the capacitance per unit area of the total system, as well as the depletion voltage:

$$c = \epsilon_0 \left(\frac{21.5\text{nm}}{9} + \frac{70\text{nm}}{12} \right)^{-1} \tag{11.4}$$

$$c = 1.2 \times 10^{-7} F/cm^2 \tag{11.5}$$

$$V = -n(1.602 \times 10^{-19} C)/1.2 \times 10^{-3} F/cm^2 \tag{11.6}$$

$$V = -0.19V \tag{11.7}$$

There is a substantial difference between the predicted value of -0.19 V, for the second sample, and the measured value of -0.8 V. However, the presence of trapped electrons in the surface layer has not been accounted for in the above estimation. Some charge density n_{trap} located at the boundary between oxide and InP must be neutralized. At depletion, V = -0.8 V, but the voltage across the InP must be approximately 0.15 V as measured previously in the oxide-free sample. The remaining 0.65 V is the voltage drop across the oxide, and depletes the extra charge n_{trap}. The charge density of the traps can therefore be estimated as:

$$n_{trap} = \frac{\epsilon \cdot V}{d \cdot e} \tag{11.8}$$

$$n_{trap} = \frac{9\epsilon_0 \cdot 0.66V}{21.5nm \cdot 1.602 \times 10^{-19}} \tag{11.9}$$

$$n_{trap} = 1.52 \times 10^{12}/cm^2 \tag{11.10}$$

This trap density corresponds to an average of one trap per 65 nm^2. This is an interesting technological finding to be taken into account during the fabrication process. However, since it is still possible to form QPCs with no unwanted incidental quantum dots under the gates, it should also be possible to form electrostatically defined quantum dots.

In the next section, we will examine a quantum dot of this type formed and probed electrically in a nanowire sample, in the few-electron regime.

11.6 Summary

InAsP nanowire samples were fabricated with electrostatic gates, with the intention of forming quantum dots. Instead, it was found that few-electron quantum dots could be formed using only one gate, instead of the expected minimum of two gates. This can be explained by the presence of potential fluctuations under the gates, which are able to support bound states. A double fluctuation quantum dot was formed, where two quantum dots were at least capacitively coupled, suggesting that some of these dots are able to form in close proximity to one another. The origin of these potential fluctuations was modelled as trapped charges at the interface between the InAsP and the atmosphere or oxide (depending on whether the sample has an oxide layer). The addition of a layer of aluminum oxide reduces the number of quantum dots of this type observed in QPCs.

Chapter 12

Quantum Dot Formed in InGaAs Nanowire Ridge

In addition to InAsP nanowires embedded in InP ridges, InGaAs nanowires were grown by the same method. Interest in the InGaAs material predated interest in InAsP within the group at NRC, mostly because this material is optically active in the Telecom optical fiber range (about 1.55µm), and the larger electron g-factor is preferable for some spin-qubit applications. As part of pursuing scalable linear quantum dot arrays, many devices were manufactured.

Due to gate fabrication difficulties outlined in section 8, only a few devices were tested which functioned well at low temperatures. However, experiments have revealed that even the partially functional devices are compatible with few-electron confinement due to the presence, as in the InAsP samples from the previous section, of a non-uniform background potential.

A device was selected as a candidate for low-temperature experimentation. As part of single-gate tests performed at 250 mK, current was found to pass through the device, with gates energized past depletion, in a manner consistent with Coulomb blockade.

The ridge which was studied was fabricated with a base width of 460nm. A triangular nanowire approximately 40nm tall, and 80nm wide was formed, which extended along the entire length of the ridge (10 microns). Two gates were placed 100 nm apart along the ridge, with the intention of using them to electrostatically define a quantum dot (see figure 12.1).

12.1 Single Gate Tests

Before single gate tests were performed, the voltages on both gates were swept simultaneously, so as to eliminate the possibility of current passing between the two gates and damaging them. In this case the device showed signs of pinch-off when both gates were swept, with zero current occurring at approximately -1 V.

Single gate tests were performed, with careful monitoring of leakage current from the gates to the 2DEG and to each other. No leakage current was detected, and it was certainly less than 100 pA. However, only one gate, arbitrarily identified here as the “left gate”, achieved pinch off before -2 V. The right gate did affect the resistance of the sample, indicating a possible break at the apex of the ridge, resulting in a half functional gate (see figure 8.4b for an example).

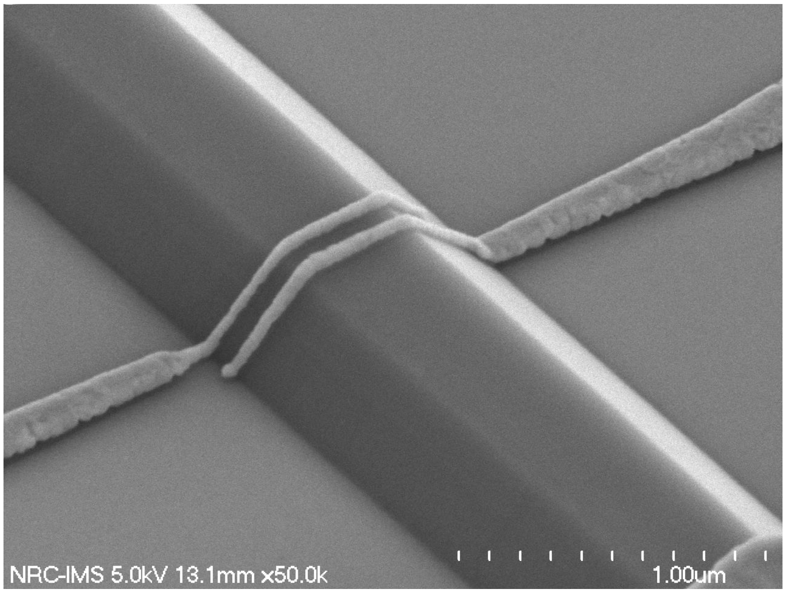

Figure 12.1: SEM image of semiconductor ridge with an embedded nanowire (not visible).

12.2 Charge Stability and Coulomb Diamond Measurements

Coulomb blockade peaks were observed once the gates were energized. A charge stability diagram (figure 12.2a) confirmed that these Coulomb blockade peaks were most sensitive to the gate which showed the pinch-off effects and suggests the formation of quantum dots under or near a single gate. Few to many quantum seem to form, particularly when the gate voltage is more positive. As the voltage on the left gate becomes more negative, the density of peaks decreases. A final peak is eventually observed, which may correspond to the last electron in the last dot.

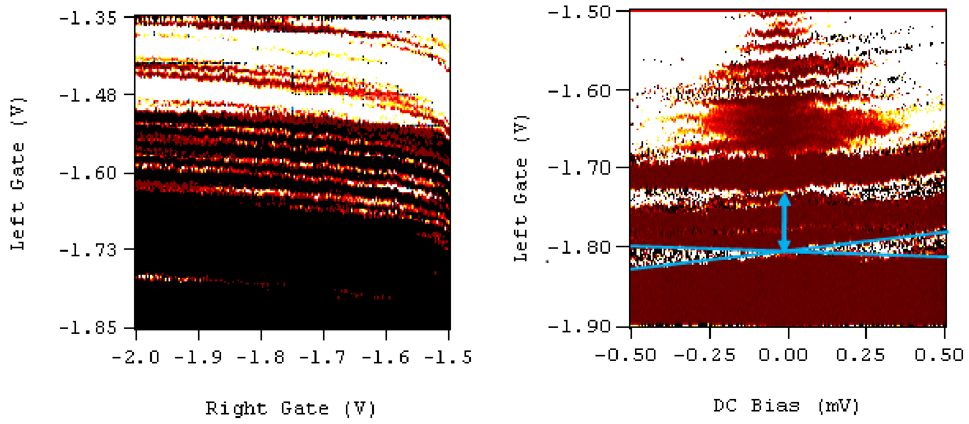

(a) Charge stability diagram. Both gates are past depletion, but only one is near pinch off (the left gate). The frequency and intensity of the peaks depends only on the voltage on the left gate, though the peaks do shift somewhat as the right gate voltage is swept.

(b) Coulomb diamond measurement of the addition energy, approximately 1.9 meV.

Figure 12.2: Coulomb blockade in quantum dot formed in a ridge nanowire.

The observation of Coulomb blockade peaks was unexpected, given that one of the two gates was not able to fully deplete the 2DEG underneath it. This indicates that there is likely only one functional gate able to raise and control a barrier above the fermi level. Typically, such as in GaAs/InGaAs, this is not be enough to define a quantum dot. However, in light of the similar observations in many-gated InAsP samples in the previous section, this may be explained by the presence of potential fluctuations under the gates.

Supposing that a potential fluctuation were to exist in the depletion region under the gate, that fluctuation might support electronic bound states. While the barrier might be wide enough to prevent direct tunnelling from one side to the other, the charge states in the fluctuation could, in principle, support resonant tunnelling as an electrostatically defined quantum dot does. Resonant tunnelling would be maximal for fluctuations which are directly underneath the gate, since that ensures the two tunnelling barriers are symmetric and that the limiting tunnelling rate, which could be either one, is maximized. This scenario is sketched out in figure 12.3, which illustrates the case of an incidental quantum dot with asymmetric barriers.

Fluctuation quantum dots have been identified previously in InGaAs [23], though the measurements presented in this section are original and confirm the fluctuation model.

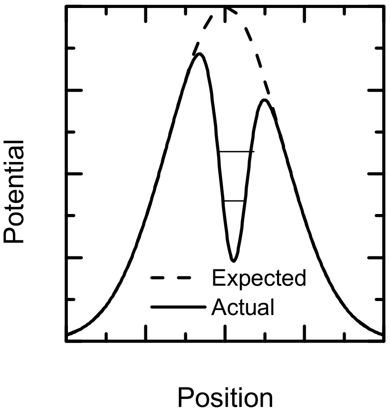

Figure 12.3: Sketch of an example potential along the nanowire which might be produced by a single gate (dashed line) and the same plus an incidental fluctuation (solid line) as a function of position along the length of the nanowire ridge. Two bound states of well-defined energy exist (represented by horizontal lines in the potential well) in this scenario. Despite only one gate and only one expected tunnelling barrier, a quantum dot with two barriers to two leads can form, and Coulomb blockade peaks can be observed.

In order to help prove that fluctuation quantum dots are the origin of these observations, Coulomb diamond measurements were performed and the addition energy for the last visible electron charging event was measured. Figure 12.2b shows the data. The charging energy was measured to be 1.9 meV. This corresponds to an approximate dot radius of 150 nm, assuming that the addition energy is equal to the charging energy and that the quantum dot is a disk capacitor (in accordance with the model discussed in section 3).

12.3 Summary

The estimated size of the quantum dot, 100 nm, is comparable to the expected size of the depletion region under the 50 nm wide gates of the device. The measured charging energy is comparable to the value for the planar InAsP quantum dot examined in section 11, suggesting that these dots arise from a similar mechanism that is not strongly dependent on the composition of the nanowire. The origin of these non-uniform potential flucutations more than 2 meV deep and capable of supporting multiple bound states is not precisely clear, though it appears that they are present in two different material systems: planar InAsP/InP and nanotemplated InGaAs/InP nanowire ridges. If these incidental dots are not desired, wider electrostatic gates may in principle suppress tunnelling underneath them by widening the tunnelling barriers for each incidental quantum dot. This adjustment has not been tested at time of writing, however new samples with wider gates are under fabrication at time of writing.

Chapter 13

Role of in-plane Magnetic Fields in Scattering Processes of Planar Structures

Lateral quantum dots in quantum well structures are typically subjected to large in-plane magnetic fields to provide sufficient spin splitting for spin qubits ($g\mu_B > k_BT$, where μ_B is the Bohr magneton). In particular, for single spin qubits, large fields are employed to increase the rate and quality of initialization. In zero g-factor dots for photon to spin conversion, large fields will be employed to split the light hole states for the spin to photon conversion method in section 6. In asymmetric g-factor quantum dots, the small g-factor difference in a double dot must be somewhat amplified by a large field for Bell measurement as per the protocol discussed in section 5. These facts point to the importance of large in-plane magnetic fields applied to 2DEGs in order to operate spin qubits for quantum infomation applications.

The orbital component of the dynamics of a 2DEG with zero thickness are expected to be insensitive to the in-plane magnetic field due to the strong confinement in the z direction. In reality, however, no 2DEG is truly infinitesimally thin. Therefore, magnetic fields may modify the 2DEG properties and influence the dynamics of quantum dots made from it.

To study such effects, we chose a Hall bar sample made from high-mobility GaAs/AlGaAs 2DEG. In this sample, we have measured a significant increase in the single particle scattering rate (τ_q) for electrons in the 2DEG when a magnetic field is applied in the plane of the 2DEG. These measurements were conducted by making use of the sensitivity of Microwave Induced Resistivity Oscillations (MIRO) to the quantum lifetime (τ_q) of Landau levels. This increase has not yet been explained theoretically, but it may be due to the non-ideal nature of the 2DEG, since no such change has been predicted to occur in an infinitesimally thin 2DEG.

13.1 MIRO Phenomenology

MIRO are oscillations in the resistivity of a high mobility 2DEG which can occur when microwave radiation is incident on the sample[17]. The presence of a large perpendicular magnetic field and an electric field capable of producing a current are also required. The microwave energy is converted into an electromotive force. The force is proportional to the voltage applied to the sample, manifesting as a change in the apparent resistivity. The effect occurs only in the presence of a magnetic field perpendicular to the plane of the sample, and the magnitude and sign of the resistivity change depends on the magnitude of this field in an oscillatory manner. The mechanisms that lead to this effect will be discussed in the following sections.

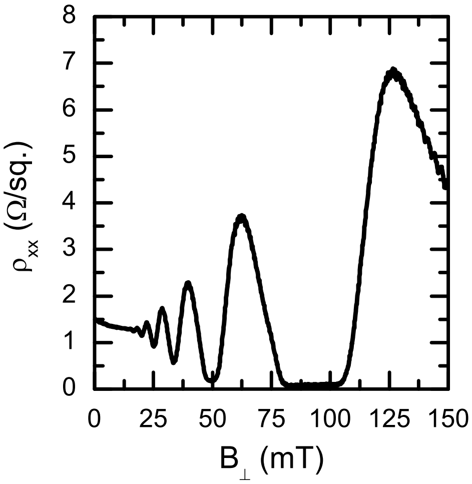

Figure 13.1: Microwave Induced Resistivity Oscillations, at $T = 260\,\mathrm{mK}$*, with micrwave radiation applied at 48.4 GHz. The applied magnetic field,* $B_\perp$*, is normal to the plane of the 2DEG. Note the zero-resistance plateau centered about 90 mT.*

MIRO amplitude can exceed the base resistance at zero magnetic field (R_0) and the magnetoresistance of the 2DEG, leading to dips in resistivity where it approaches zero total resistance. The existence of these Zero Resistance States (ZRS) has motivated much of the work in the field[44]. Measurements of MIRO, including observations of ZRS, are presented in figure 13.1.

13.2 Displacement Mechanism

One of the mechanisms which is thought to cause MIRO is known as the displacement mechanism. In can be understood to be the indirect excitation of electrons in a partially filled Landau level to a higher Landau level. These indirect transitions, illustrated in figure 13.2d, require spatial displacement to match the energy of the initial electron-photon system to the final excited electron state. Spatial displacement of electrons may be accomplished by scattering through disorder. Displacement of many electrons in a sufficiently intense MW field results in a component of current forward or against the electric field applied to the sample[17].

These microwave-induced currents oscillate as a function of the applied MW frequency with a period equal to the cyclotron frequency $\omega_c = \frac{qB_\perp}{m^*}$, and can act with or against the external current induced by the applied electric field. The resistivity changes as a function of the field because the spacing of the Landau levels changes with field magnitude. If instead microwave frequency is held constant and the perpendicular magnetic field is swept, the oscillations appear periodic with respect to $1/\omega_c$ (or $1/B\perp$).

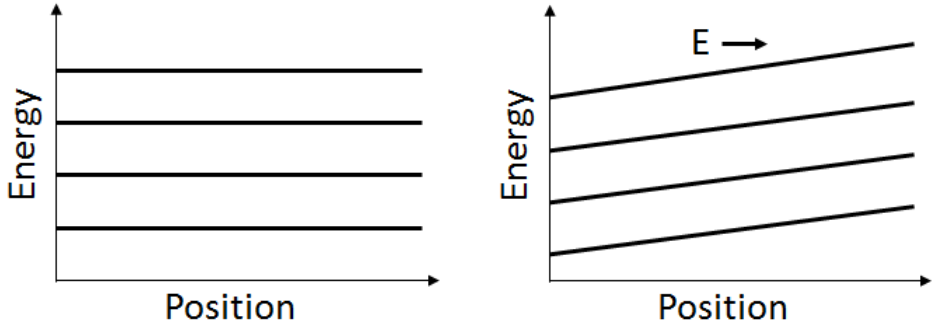

(a) The application of a large perpendicular magnetic field induces Landau quantization: $E = \hbar\omega_c(n + \frac{1}{2})$.

(b) An electric field applied accross the sample in the 'x' direction tilts the Landau levels as a function of position along the electric field axis.

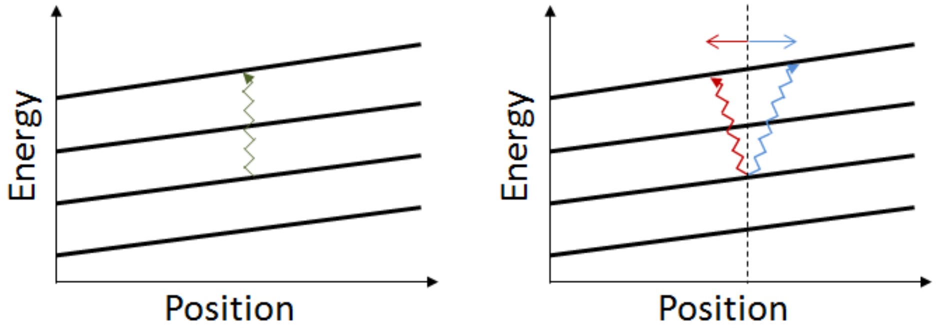

(c) A microwave photon can excite an electron to a higher Landau level, though this direct transition imparts no momentum.

(d) Indirect transitions are possible for off-resonant photons as long as the electron is spatially displaced to a position where it can occupy a Landau level. These displacements create components of current with or against the electric field, depending on the frequency of the radiation.

Figure 13.2: *Illustration of the displacement mechanism.*

13.3 Non-equilibrium Density of States Mechanism

MW radiation can also induce a non-equilibrium distribution of electrons among and within the Landau levels. This oscillatory electron distribution manifests itself as a change in conductivity[16]. The overall effect is similar, has the same relationship to the cyclotron frequency, and is identically dependent on the shape parameters of the Landau levels, the principle one being τ_q, the single particle scattering time.

In the regime where MIRO amplitude is not saturated and is linearly dependent on the amplitude of MW radiation, and also where the Landau levels are overlapping, the MIRO photoresistance takes the form:

$$\delta\rho \propto \epsilon\lambda^2 \sin(2\pi\epsilon) \tag{13.1}$$

where $\epsilon = \omega/\omega_c$, and $\omega = 2\pi f$ is the angular frequency of the MW radiation. In this equation the damping factor $\lambda = \exp(-\frac{\epsilon}{2f\tau_q})$ depends only on the single particle scattering time. Whereas the base resistivity is dependent on the transport lifetime, MIRO depend only on the width of the landau levels. This is because the shorter the lifetime, the more overlap between levels and the more uniform the density of states. This is also why only the perpendicular component of the magnetic field are relevant to the theory of their operation for a thin 2DEG: Landau quantization is unaffected by the in-plane component of the field.

13.4 Conflicting Observations of Field Dependent Scattering

By equation 13.1, only the single particle scattering time and the plane-perpendicular component of magnetic field are relevant to the shape of MIRO. Although many details determine the constant of proportionality that has been omitted, these two parameters are the only variables which determine the relative change of resistivity with respect to $B_\perp$.

In practice, some experiments[60] have shown damping due to the action of an in-plane magnetic field in addition to the perpendicular field, with in-plane fields of about 1 T. Others have demonstrated a lack of damping for yet larger values of in-plane field[43], up to 1.2 T. This controversy respresents a lack of understanding either of MIRO or of the behaviour of the 2DEG itself in the presence of in plane magnetic fields.

Other studies have since revealed that MIRO are not the only effect which are sensitive to this parallel field damping. Hall field Induced Resisitivity Oscillations, or HIRO, have been found to be similarly damped[28].

In order to attempt to model the phenomenon, we have sought to use MIRO as a probe of the quantum lifetime τ_q. We have found that indeed the damping effect is consistent with a change in the overall lifetime due to the parallel field. This observation is consistent with the observations made using HIRO in [28] except that MIRO are sensitive only to the lifetime, which suggests that a change in the shape of the Landau levels or scattering processes is the root cause.

13.5 Experimental Methodology

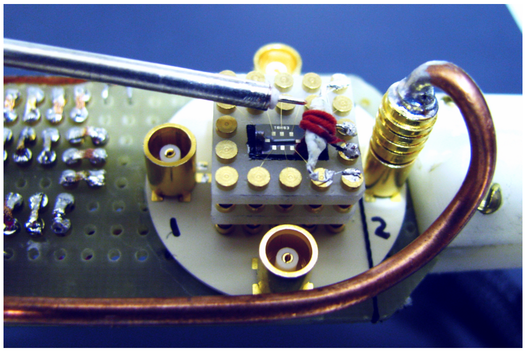

Figure 13.3: High mobility 2DEG sample mounted in the cryostat sample socket. Note the MW antenna whose orientation is fixed with respect to the sample even as the mount rotates as a whole in the cryostat.

A rectangular section of ultra high mobility 2DEG was mounted in a He3 cryostat with a base temperature of approximately 260mK. A linear 2.5mm MW antenna was positioned just above the sample, running parallel to the plane of the sample. Figure 13.3 shows the exact setup. The section of 2DEG was 3 times longer than it was wide, and at all times current was passed along its length. The cryostat was equipped with a 5 T split coil superconducting electromagnet, and the entire mounting assembly, antenna, and vacuum can can be made to rotate in the bore of the electromagnet such that the apparent direction of the magnetic field changes, while the electromagnetic configuration of the assembly remains constant.

At a temperature of 2 K, mobility and concentration were measured through the quantum Hall effect using standard techniques. After a brief illumination, a mobility of 13.8×10^6 $cm^2/(V\cdot s)$ was obtained along with a carrier concentration of $3.4\times10^{11}/cm^2$.

MW were generated by transmitting electrical signals to the antenna at tunable frequency and power, using an Anritsu 69377B microwave generator with a few mW of output power. Any microwave power quantities quoted here are measured in decibels and reflect power at the generator output, before further attenuation in coaxial cables and before antenna efficiency, which vary with frequency.

With the sample oriented perpendicular to the bore of the electromagnet, the magnetic field was swept over a variety of ranges in both polarities to confirm that, indeed, the effect was symmetric in magnetic field. In order to introduce an in-plane field component, the sample was tilted by an angle θ from the perpendicular orientation. The Hall resistance, R_{xy}, in this tilted orientation was compared to its maximal value at zero tilt. This comparison served as a precise measurement of the perpendicular field component and as a precise measure of the tilt angle since $\theta = \cos^{-1}(R_{xx}/R_{xx}(\theta = 0))$.

13.6 Field Dependent Scattering Observations

The observation of MIRO was made at the cryostat base temperature of 260mK while increasing the MW power. Figure 13.4a shows that MIRO amplitude increases linearly in the MW power (measured in dB), consistent with the linear power regime.

A temperature dependence was also completed, showing that at temperatures higher than 750 µK MIRO begin to fade, but that near the base temperature of 260 µK the amplitude is roughly independent of temperature. Figure 13.4b demonstrates that the MIRO should be insensitive to minor heating effects and that the amplitude of MIRO is in fact that the mobility of this sample at the base temperature in our cryostat is not limited by temperature, but by the scattering processes in the sample.

Finally, the parallel field component was introduced by running a series of sweeps of magnetic field at different values of tilt. Immediately, the effect became apparent. For small fields, of order 0.5 T, the amplitude of the lowest order MIRO oscillations visible decreased (figure 13.4c).

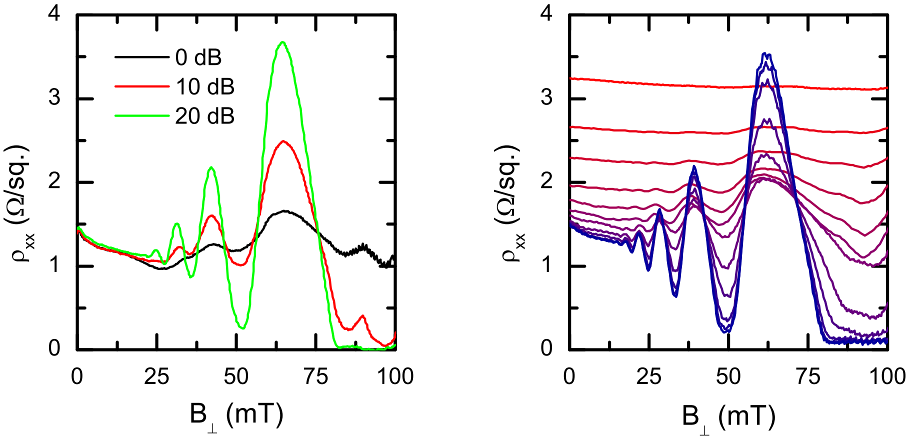

(a) MIRO traces vs. perpendicular component of magnetic field for different microwave powers. Power measured in arbitrary units.

(b) MIRO dependence on temperature. At high temperatures (red, 4 Kelvin), the effect is not visible. Towards lower temperatures (blue, 750mK), the effect saturates and becomes insensitive to temperature.

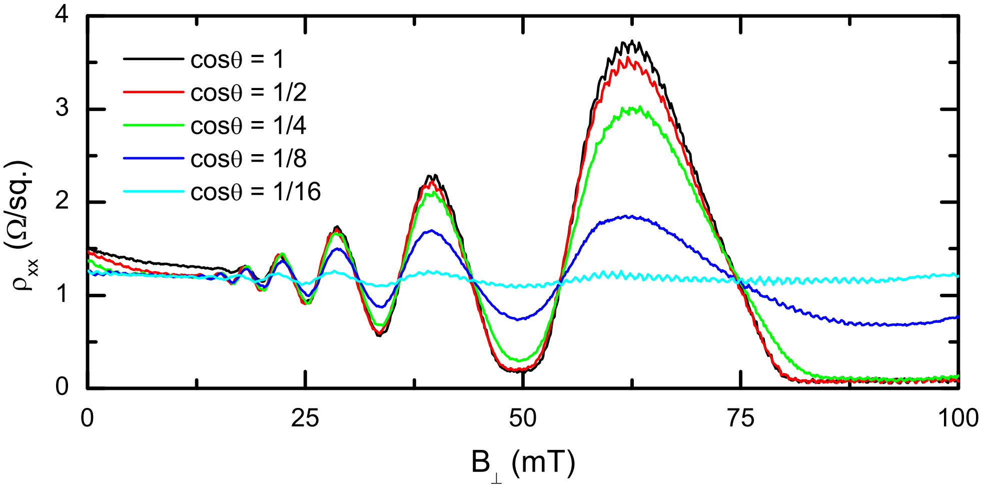

(c) MIRO dependence on tilt angle. Note that low order oscillations (at larger field) are damped at smaller tilt angles than higher order oscillations.

Figure 13.4: MIRO oscillations under varying conditions, with a fixed microwave frequency of 48.4 GHz.

13.7 Discussion

It was hypothesized that the observed amplitude reduction as a function of tilt was caused by a change in τ_q. The simplest model is that an additional component to the scattering rate is introduced:

$$\frac{1}{\tau_q} = \frac{1}{\tau_{q0}} + \delta\frac{1}{\tau_q} \tag{13.2}$$

With that assumption in mind, equation 13.1 yields:

$$\delta\rho(\theta) \propto \epsilon\lambda^2 \sin(2\pi\epsilon) * \exp(-\frac{\epsilon}{f}\delta(\frac{1}{\tau_q})) \tag{13.3}$$

$$A/A_0 \equiv \frac{\delta\rho(\theta)}{\delta\rho(0)} = \exp(-\frac{\epsilon}{f}\delta(\frac{1}{\tau_q})) \tag{13.4}$$

So, the attenuation factor due to the parallel field component should be exponential in the increase in the scattering rate.

Measurements of oscillation amplitude were taken for various tilt angles, for several oscillation orders. The amplitude damping factor A/A_0 was extracted for the minima and maxima of the MIRO oscillations and plotted against $1/\epsilon$ (which is proportional to $\propto B_{||}$) for various tilt angles. Assuming that $\delta(\frac{1}{\tau_q})$ is quadratic in $B_{||}$, A/A_0 can be expressed in several different ways:

$$A/A_0 \equiv \exp(-\frac{\beta(\theta)}{\epsilon}) \equiv \exp(-\frac{\alpha\tan^2(\theta)}{\epsilon}) \equiv \exp(-\frac{\epsilon\gamma B_{||}^2}{f}) \tag{13.5}$$

The fitting parameter β is simple to extract for a set of amplitudes at a given tilt angle. From a series of β values at different tilt angles, α can then be extracted from a fit to the relationship $\beta = \alpha\tan^2\theta$. Figure 13.5 illustrates this analysis. The experimental data is consistent with the quadratic assumption over many orders of magnitude of $\tan^2\theta$.

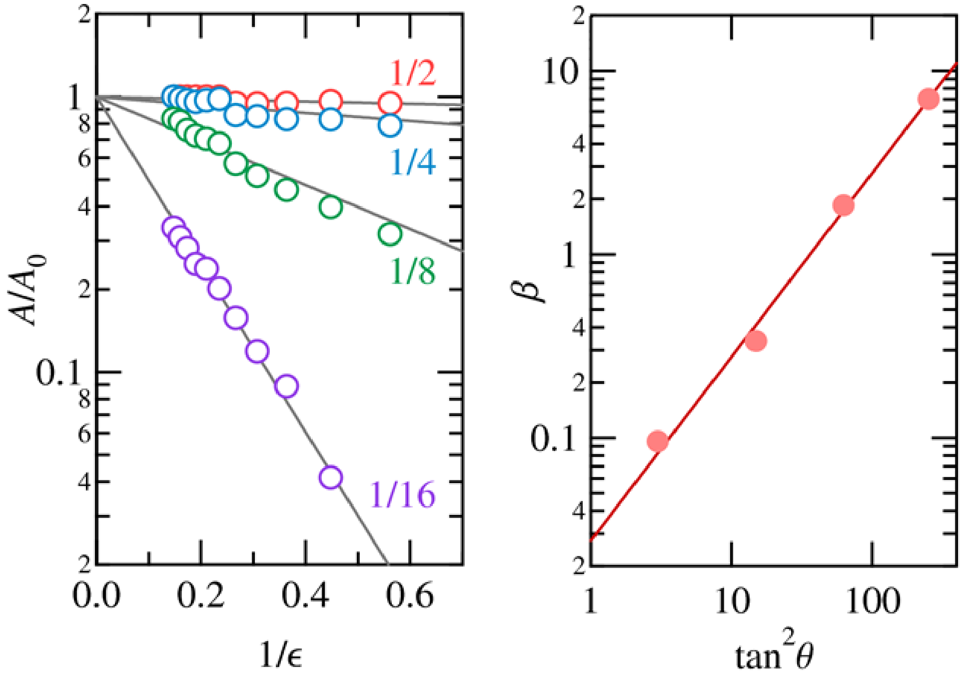

(a) Fit of the normalized oscillation amplitude A/A_0 to determine β for each tilt angle.

(b) Fitting the function $\beta(\theta)$ optained from the previous fits to determine $\alpha = 0.028$ in equation 13.5.

Figure 13.5: Fits to equation 13.5, which assumes an increase in scattering rate which is quadratic in $B_{||}$.

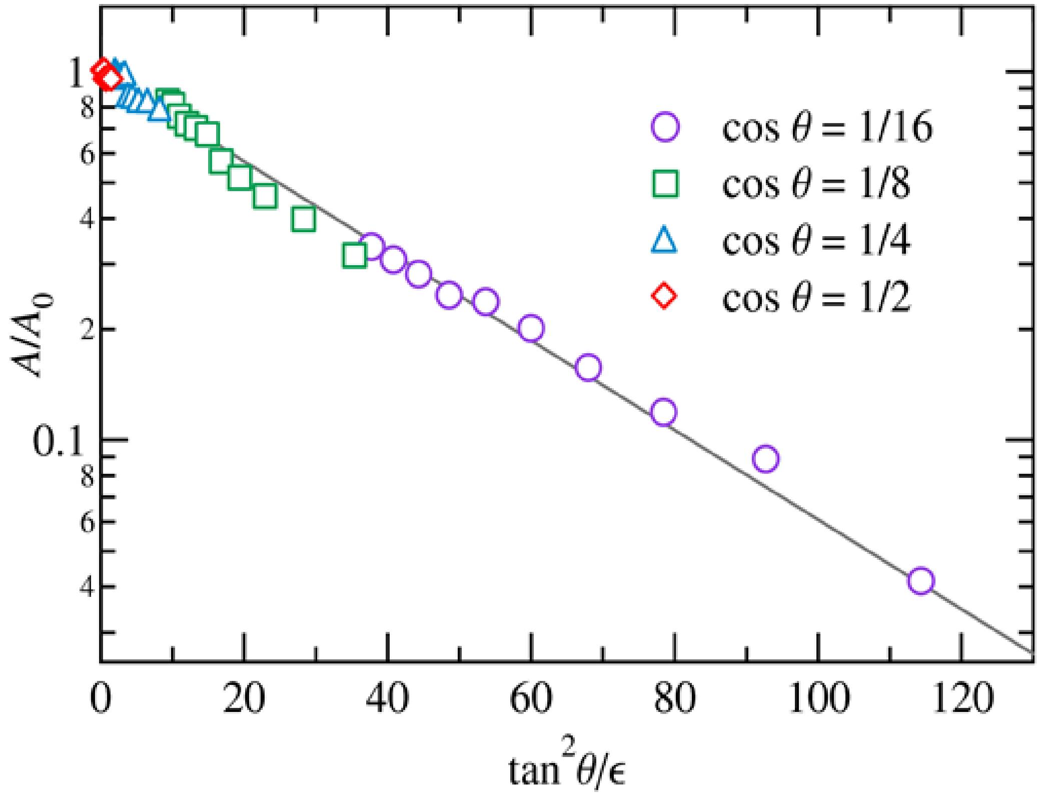

Figure 13.6: An alternate fitting method, whereby amplitude data from all tilt angles collapse onto one line, which is fit to find $\gamma = 1.0 \times 10^{11}\mathrm{s}^{-1}\,\mathrm{T}^2$.

13.8 Summary

It was found that Microwave Induced Resistivity Oscillations (MIRO) are indeed damped by the application of large parallel magnetic fields. Damping is consistent with an increase in the single particle scattering rate τ_q, which is the quantum lifetime of the Landau levels and may indicate a change in the scattering processes at work in the 2DEG. In this case, an in-plane magnetic field of order 0.7 T was enough to halve the scattering time.

The explanation in terms of a change in τ_q is consistent with a study of Hall Induced Resistivity Oscillations (HIRO)[28]. This suggests that the observations really are caused by a change in τ_q, and not a MIRO or HIRO-specific mechanism that has yet to be identified.

The extra scattering rate introduced by the parallel field is proportional to the square of that field component. In this sample, the extra scattering rate became dominant at just 0.7 T and continued to grow in good agreement with the quadratic law up to nearly 5 T, the critical field of the superconducting magnet that was used in this experiment.

The apparent disagreement between studies [60] and [43] may be explained by a degree of variability in this critical field value between different samples. This result shows the importance of large parallel field effect on quantum scattering times, which should be kept in mind when designing quantum dot-based spin qubit devices.

Chapter 14

Conclusions

In order to construct low-loss quantum communication channels with reasonably high throughput over long distances, a technology such as the quantum repeater is needed. The utility of such a device is clear, as it would enable physically secure communication free from the eavesdropping. We have demonstrated via performance modelling that for the purposes of constructing quantum communication links on a global scale, hybrid photon and matter qubit devices such as spin/photon devices offer superior throughput as a function of total link distance. In principle, spin qubit devices can store quantum information from incoming photons, act as a heralded quantum memory, and additionally perform full Bell measurement, something not possible with linear optical devices. We have seen also that the success probability of Bell measurement is the dominant factor in the throughput of a long-distance quantum repeater chain, and so maximizing this probability is key.

g-factor engineering of spin qubits is necessary for the photon to spin qubit conversion schemes or the Bell measurement schemes illustrated in sections 6 and 5. Conceptual techniques for the manipulation of quantum well g-factor, as well as theoretical calculations of effective electron g-factor in a double quantum well as a function of electric field applied by a global gate, were presented in section 7. For the double InAsP quantum well, a sign change can be, in principle, induced in-situ by dynamically tuning this electric field for particular quantum well compositions, thicknesses, and spacings, including the one presented in section 7. Since the near-zero g-factor regime is necessary for both the Bell measurement and photon to spin conversion techniques presented here, this is an encouraging prediction for further work in this vein.

Samples prepared by CBE nanotemplated nanowire fabrication technology were investigated, first by determining the limiting factors to device yield and then by attempting to form a few-electron quantum dot. It was found that the electrostatic gates frequently suffer from breakage at the apex and base of the ridge devices for different reasons, but that both causes stem from the over-growth of the cap layer. To correct the problem, measures were suggested which may improve the yield by reducing the size of the cap.

Attempts to form few-electron quantum dots in an InGaAs ridge nanowire were successful despite some device damage, presumably for the same reason that planar and ridge-based InAsP quantum dots formed under and between gates. Evidence was presented to support the conclusion that a non-uniform random potential is created in the 2DEG by charge traps near the interface between the epitaxial surface of the sample and the insulating oxide (if present). A similar random potential was imaged previously via Scanning Gate Microscopy (SGM)[1], and these fluctuations evidently can result in the formation of quantum dots.

Finally, large (few Tesla) magnetic fields applied in the plane of a high-mobility GaAs/AlGaAs heterostructure was found to dramatically increase single-particle scattering. The scattering rate, as probed by Microwave Induced Resistivity Oscillations (MIRO), doubled at 0.7 T and continued to increase according to a quadratic power law in the in-plane component of the field. Since fields in excess of 1 T and frequently as high as 5 T are routinely applied in spin qubit experiments, and since yet larger magnetic fields may be required if g-factor engineering is employed to reduce the electron g-factor to near zero, this is worth considering and making the effort to understand in the future.

This work was completed with a view towards realizing a scalable quantum repeater. Full Bell measurement of spin qubits and coherent conversion of photon information to spin information have both yet to be demonstrated, and engineering the g-factor conditions necessary to prove these concepts is the next logical step of this research.

Appendices

Appendix A

Quantum Repeater Models: Optical and Solid State Schemes

In section 2, two performance models for two hypothetical quantum repeaters were presented: an all-optical model with no heralded memory, and a hybrid spin-photon model with heralded memory. The optical repeater's transmission rate was given by equation 2.2, which included the unspecified function $F(N, L/L_0, I)$. Similarly, the hybrid model's transmission rate (equation 2.3) was given in terms of $G(E_i, N, L/L_0, I)$. The calculation of each of these functions is the subject of this appendix.

Recall the meanings of the symbols in question:

E_i :Efficiency of memory (input)
L :Length of an individual repeater link
L_0 :Quantum channel's characteristic absorption length
N :The number of direct entanglement distribution links (each of length L)
I :Number of round-trip communications allowed per memory coherence time

Note also that only G depends on E_i. This is because the E_i dependence in the optical case is a simple exponential decay with increasing N, and thus has been factored out of the function F.

The quantum repeater chain is assumed to consist of N links of length L, and as many BSM and Bell emitter nodes as necessary for the particular repeater model in question. The entire repeater chain is modeled as a Markov state machine consisting of those N links, each of which (at a given time) is either *ready* or *waiting*. The number of links (N) defines the machine, and the number of *ready* links (Nr) defines the state of the machine. The complimentary number of *waiting* links (N−Nr) is also useful.

A Python program was written which calculates, plots, and outputs the transmission rate (a fraction of the emitter generation rate, which is an unknown variable not related to the choice of quantum memory or Bell measurement platform). The program calculates a Markov state propagation matrix, and repeatedly propagates that state I times (I is assumed to be intelligently chosen small enough that errors are sufficiently unlikely and yet the ultimate likelyhood of successfully establishing all N links is sufficiently high. I have assumed an I value (for both repeater models, in the interest of fairness) of 50. The code is included below. Python 2.7 is required, as well as matplotlib (for plotting, optionally) and numerical python (numpy). The python(x,y) distribution includes all of these tools, and can be found here at time of writing: `https://code.google.com/p/pythonxy/`.

```
import numpy as np
# [Remove to skip plotting]
import matplotlib.pyplot as plt

from scipy.misc import comb

def attn(dB, L): return 10**(-dB/10.0*L)

## From a number of waiting links (N),
## what are the odds of reaching the new
## number of waiting links (n) given an
## individual link success probability (P)?
def nofN(P, n, N):
    if n > N: return 0.0
    return comb(N, n) * (1-P)**n * P**(N-n)

## Build the Markov matrix that propagates a
## machine of N links and individual probability
## P forward one iteration.
def markov(P, N):
```

```
    # A minor time-saving technique that
    # remembers the last result if there
    # was one, and just returns that when
    # appropriate.
    if markov.last[0] == P \
      and markov.last[1] == N:
        return markov.last[2]

    # Computer the elements of the matrix
    M = np.zeros( (N+1, N+1) )
    for i in range(N+1):
        for j in range(N+1):
            M[i, j] = nofN(P, i, j)
    return M
# Initialize the static variable 'last'
# in the functor 'markov()'.
markov.last = (0.0, 0, np.zeros( (1, 1) ))

## Computes the transmission rate for
## a set of parameters and a supplied
## helper function rate_h, which depends
## on the model.
def rate(dB, X, BSM, eff, I, c, rate_h):
    # The function dynamically optimizes
    # N to ensure the transmission rate
    # is as high as possible.
    Y = np.zeros(len(X))
    N = 1
    for i, x in enumerate(X):
        low  = rate_h(dB, x, BSM, eff, N,   I)
        high = rate_h(dB, x, BSM, eff, N+1, I)
        # Make sure there are never more than 30 links.
        while low < high and N < 30:
            N += 1
            low  = rate_h(dB, x, BSM, eff, N,   I)
            high = rate_h(dB, x, BSM, eff, N+1, I)
            print "D={},␣trying␣N={}".format(x, N)
        Y[i] = low
```

```
    plt.plot(X, Y, c) # [Remove to skip plotting]
    return (X, Y)

# 1: All-Optical model parameters
conditions = [
    # (link attenuation [dB], BSM prob,
    # memory input*output efficiency)
    (0.2, 0.5, 0.5*0.5, 'k'),
    (0.2, 0.5, 0.9*0.9, 'g'),
    (0.2, 0.5, 1.0, 'b'),
]

## The all-optical helper function, F.
def rate_F(dB, D, BSM, eff, N, I):
    L = D/N
    P = attn(dB, L)
    M = markov(P, N)
    i = 0
    # Initialize the state vector. Set the
    # initial probability for the starting
    # state to 1.
    state = np.zeros(N+1)
    state[-1] = 1.0
    # Repeatedly propagate the state vector
    # by the Markov matrix the allowed number
    # of times (I).
    for i in range(I):
        state = M.dot(state)
    return eff**N * BSM**N * state[0]

# Calculate and plot the results as a function
# of total distance, using matplotlib (optional).
X = np.linspace(0.0, 2000.0, 200)
Y = [0]*len(conditions)
for i, c in enumerate(conditions):
    X, Y[i] = \
      rate(c[0], X, c[1], c[2], 50, c[3], rate_F)
plt.yscale('log') # [Remove to skip plotting]
```

```
plt.show() # [Remove to skip plotting]

# File output, one data point per line.
file = open('optical', 'w')
for p in zip(X, *Y):
    tmp = ["{}".format(i) for i in p]
    tmp = ",".join(tmp) + "\n"
    file.write(tmp)
file.close()

# 2: Hybrid Scheme parameters

conditions = [
    # (link attenuation [dB], BSM prob,
    # memory input*output efficiency)
    (0.2, 0.5, 0.5, 'k'),
    (0.2, 1.0, 0.5, 'r'),
    (0.2, 0.5, 0.9, 'g'),
    (0.2, 0.5, 1.0, 'b'),
]

## The hybrid helper function, G.
def rate_G(dB, D, BSM, eff, N, I):
    L = D/(2*N)
    P = attn(dB, L) * eff
    M = markov(P, 2*N)
    i = 0
    state = np.zeros(2*N+1)
    state[-1] = 1.0
    for i in range(I):
        state = M.dot(state)
    return BSM**N * state[0]

# Calculate and plot the results as a function
# of total distance, using matplotlib (optional).
X = np.linspace(0.0, 2000.0, 200)
Y = [0]*len(conditions)
for i, c in enumerate(conditions):
```

```
    X, Y[i] = \
        rate(c[0], X, c[1], c[2], 50, c[3], rate_G)
plt.yscale('log') # [Remove to skip plotting]
plt.show() # [Remove to skip plotting]

# File output, one data point per line.
file = open('hybrid', 'w')
for p in zip(X, *Y):
    tmp = ["{}".format(i) for i in p]
    tmp = ",".join(tmp) + "\n"
    file.write(tmp)
file.close()
```

Appendix B

Singlet Rotational Invariance

Suppose U is a unitary transformation of a single qubit. In terms of the computational basis states $|0>$ and $|1>$, its operation generally has the form:

$$\begin{aligned} U|0> &= \alpha|0> + \beta|1> \\ U|1> &= -\beta^*|0> + \alpha^*|1> \end{aligned}$$

where α and β are complex numbers. This is true because any unitary U is equivalent to a basis change, and thus two states which were orthogonal before must be orthogonal after the action of U.

Consider the operation of U on the spin singlet:

$$\begin{aligned} (U \otimes U)(|01> - |10>) &= (\alpha|0> + \beta|1>)(-\beta^*|0> + \alpha^*|1>) - (-\beta^*|0> + \alpha^*|1>)(\alpha|0> + \beta|1>) \\ &= -\alpha\beta^*|00> + \beta\alpha^*|11> - |\beta|^2|10> + |\alpha|^2|01> \\ &+ \beta\alpha^*|00> - \alpha\beta^*|11> - |\alpha|^2|10> + |\beta|^2|01> \\ &= |01> - |10> \end{aligned}$$

Therefore, any unitary operator U applied to both qubits $(U \otimes U)$ does not change the state.

Furthermore, since a change to a new orthonormal basis can be expressed as a unitary change of basis operator U such that $|0'> = U|0>$ and $|1'> = U|1>$ and $|0'>$, $|1'>$ are the new basis vectors, the spin singlet appears identically in any orthonormal basis (i.e. $|01> - |10> = |0'1'> - |1'0'>$).

Finally, if either qubit is projected into any state by a projective measurement (suppose the projected state is $|0'\rangle$), the other qubit must be left in the orthogonal state $|1'\rangle$.

Appendix C

Distilling Secrets and Amplifying Privacy

Two algorithms will be presented below, each correcting the problem of either an eavesdropper having gleaned partial information about a shared key or errors having crept into the keys during the process of sharing them.

Central to both algorithms is the notion of a pairwise shuffle. That is an operation which randomly exchanges the ith bit of two strings with the same random bit in both strings. Therefore, identical strings will become shuffled, but still identical. 010001, 010001 could become 101000, 101000, for example.

C.1 Simple Error Correction

Suppose Alice and Bob have a pair of keys that they believe to be nearly identical, but which may contain errors. In order to correct errors, one inefficient but easy to understand method is to divide the keys into equal substrings, perform parity checks on the substrings, then discard substrings which do not have equal parity in both keys. This certainly deals with cases where there is at most one error per substring. The procedure can then be repeated to further increase confidence, shuffling the keys before each repetition to ensure than two errors are unlikely to appear in the same substring more than once, thus escaping detection. In this way, Alice and Bob can use two long error-prone keys to generate a shorter shared key in which they have much higher confidence. Measuring the parity of each substring and discussing it publicly gives Eve information, however, which must be corrected if privacy is to be preserved.

	Alice	Bob	
Example:	01000**1**	01000**0**	There is one error.
	010|**001**	010|**000**	Erroneous substring identified.
	010	010	The substring is discarded.

C.2 Simple Privacy Distillation

Eve, a third malicious party, may be assumed to have some information about the keys at the beginning, perhaps in the form of knowing the values of some of the bits, or she may learn from public discussion during error correction. To correct this, Alice and Bob can subdivide each key into two equal-length strings (discarding the extra bit if applicable). They can then XOR one substring with the other. To predict the outcome of the XOR, Eve must know the values of both bits. She therefore loses information very quickly if she did not already know the values of most of the bits (as Alice and Bob do). Alice and Bob can shuffle their keys and repeat this (very inefficient, but illustrative) procedure, each time halving the length of their key but drastically increasing their confidence in its secrecy.

	Alice	Bob	
Example:	**0**100**0**1	**0**100**0**1	Eve knows the values of two bits.
	010 ⊕ 0**0**1	**0**10 ⊕ 0**0**1	XOR operation performed.
	011	011	Two shorter, random keys result.

These two algorithms are terribly inefficient, but serve to illustrate the concept. For a more efficient algorithm which can deal with an adept eavesdropper who has access to unlimited computing power and has the ability to manipulate the private communication channel, consult [4].

Bibliography

[1] Aoki, N., da Cunha, C. R., Akis, R., Ferry, D. K., and Ochiai, Y. (2014). Scanning gate imaging of a disordered quantum point contact. Journal of Physics: Condensed Matter, 26(19):193202.

[2] Bell, J. S. (1964). On the einstein podolski rosen paradox. Physics, 1:195.

[3] Bennett, C. H., Brassard, G., Crépeau, C., Jozsa, R., Peres, A., and Wootters, W. K. (1993). Teleporting an unknown quantum state via dual classical and einstein-podolsky-rosen channels. Phys. Rev. Lett., 70:1895.

[4] Bennett, C. H., Brassard, G., and Robert, J.-M. (1988). Privacy amplification by public discussion. SIAM J. Comput., 17(2):210.

[5] Bogan, A., Hatke, A. T., Studenikin, S. A., Sachrajda, A., Zudov, M. A., Pfeiffer, L. N., and West, K. W. (2012). Microwave-induced resistance oscillations in tilted magnetic fields. Phys. Rev. B, 86:235305.

[6] Bogan, A., Hatke, A. T., Studenikin, S. A., Sachrajda, A., Zudov, M. A., Pfeiffer, L. N., and West, K. W. (2013). Effect of an in-plane magnetic field on microwave photoresistance and shubnikov-de haas effect in high-mobility gaas/algaas quantum wells. Journal of Physics: Conference Series, 456(1):012004.

[7] Bradbury, F. R., Takita, M., Gurrieri, T. M., Wilkel, K. J., Eng, K., Carroll, M. S., and Lyon, S. A. (2011). Efficient clocked electron transfer on superfluid helium. Phys. Rev. Lett., 107:266803.

[8] Briegel, H.-J., Dür, W., Cirac, J. I., and Zoller, P. (1998). Quantum repeaters: The role of imperfect local operations in quantum communication. Phys. Rev. Lett., 81:5932.

[9] Busl, M., Granger, G., Gaudreau, L., Snchez, R., Kam, A., Pioro-Ladrire, M., Studenikin, S. A., Zawadzki, P., Wasilewski, Z. R., Sachrajda, A. S., and Platero, G. (2013). Bipolar spin blockade and coherent state superpositions in a triple quantum dot. Nature Nanotechnology, 8(4):261.

[10] Chau, H. F. (2002). Practical scheme to share a secret key through a quantum channel with a 27.6Phys. Rev. A, 66:060302.

[11] Ciorga, M., Sachrajda, A. S., Hawrylak, P., Gould, C., Zawadzki, P., Jullian, S., Feng, Y., and Wasilewski, Z. (2000). Addition spectrum of a lateral dot from coulomb and spin-blockade spectroscopy. Phys. Rev. B, 61:R16315.

[12] Coish, W. A. and Loss, D. (2005). Singlet-triplet decoherence due to nuclear spins in a double quantum dot. Phys. Rev. B, 72:125337.

[13] Cova, S., Ghioni, M., Lacaita, A., Samori, C., and Zappa, F. (1996). Avalanche photodiodes and quenching circuits for single-photon detection. Appl. Opt., 35(12):1956.

[14] Dawson, C. M. and Nielsen, M. A. (2005). The solovay-kitaev algorithm. arXiv:quant-ph/0505030. arXiv: quant-ph/0505030.

[15] DiVincenzo, D. P. and IBM (2000). The physical implementation of quantum computation. arXiv:quant-ph/0002077. arXiv: quant-ph/0002077.

[16] Dmitriev, I. A., Vavilov, M. G., Aleiner, I. L., Mirlin, A. D., and Polyakov, D. G. (2005). Theory of microwave-induced oscillations in the magnetoconductivity of a two-dimensional electron gas. Physical Review B, 71(11):115316.

[17] Durst, A. C., Sachdev, S., Read, N., and Girvin, S. M. (2003). Radiation-induced magnetoresistance oscillations in a 2D electron gas. Physica E: Low-dimensional Systems and Nanostructures, 20(12):117.

[18] Ekert, A. K. (1991). Quantum cryptography based on bells theorem. Phys. Rev. Lett., 67:661.

[19] Engel, H.-A., Kouwenhoven, L., Loss, D., and Marcus, C. (2005). Controlling spin qubits in quantum dots. In Everitt, H., editor, Experimental Aspects of Quantum Computing, pages 115–132. Springer US.

[20] Fujita, T., Kiyama, H., Morimoto, K., Teraoka, S., Allison, G., Ludwig, A., Wieck, A. D., Oiwa, A., and Tarucha, S. (2013). Nondestructive real-time measurement of charge and spin dynamics of photoelectrons in a double quantum dot. Phys. Rev. Lett., 110:266803.

[21] Gaudreau, L., Studenikin, S. A., Sachrajda, A. S., Zawadzki, P., Kam, A., Lapointe, J., Korkusinski, M., and Hawrylak, P. (2006). Stability diagram of a few-electron triple dot. Phys. Rev. Lett., 97:036807.

[22] Gobby, C., Yuan, Z. L., and Shields, A. J. (2004). Quantum key distribution over 122 km of standard telecom fiber. Applied Physics Letters, 84(19):3762.

[23] Granger, G., Studenikin, S. A., Kam, A., Sachrajda, A. S., and Poole, P. J. (2011). Few-electron quantum dots in ingaas quantum wells: Role of fluctuations. Applied Physics Letters, 98(13).

[24] Grice, W. P. (2011). Arbitrarily complete bell-state measurement using only linear optical elements. Phys. Rev. A, 84:042331.

[25] Griffiths, D. (2005). Introduction to Quantum Mechanics. Pearson international edition. Pearson Prentice Hall.

[26] Hanson, R., Kouwenhoven, L. P., Petta, J. R., Tarucha, S., and Vandersypen, L. M. K. (2007). Spins in few-electron quantum dots. Rev. Mod. Phys., 79:1217.

[27] Hanson, R., Witkamp, B., Vandersypen, L. M. K., van Beveren, L. H. W., Elzerman, J. M., and Kouwenhoven, L. P. (2003). Zeeman energy and spin relaxation in a one-electron quantum dot. Phys. Rev. Lett., 91:196802.

[28] Hatke, A. T., Zudov, M. A., Pfeiffer, L. N., and West, K. W. (2011). Resistance oscillations induced by the hall field in tilted magnetic fields. Phys. Rev. B, 83:081301.

[29] Heiss, M., Fontana, Y., Gustafsson, A., Wst, G., Magen, C., ORegan, D. D., Luo, J. W., Ketterer, B., Conesa-Boj, S., Kuhlmann, A. V., Houel, J., Russo-Averchi, E., Morante, J. R., Cantoni, M., Marzari, N., Arbiol, J.,

Zunger, A., Warburton, R. J., and Fontcuberta i Morral, A. (2013). Self-assembled quantum dots in a nanowire system for quantum photonics. Nature Materials, 12(5):439.

[30] Hermelin, S., Takada, S., Yamamoto, M., Tarucha, S., Wieck, A. D., Saminadayar, L., Buerle, C., and Meunier, T. (2011). Electrons surfing on a sound wave as a platform for quantum optics with flying electrons. Nature, 477(7365):435.

[31] Hodelin, J. F., Khoury, G., and Bouwmeester, D. (2006). Optimal generation of pulsed entangled photon pairs. Phys. Rev. A, 74:013802.

[32] Hodges, J. S., Pappas, S. P., Weinstein, Y., and Gilbert, G. (2012). Polarization/time-bin basis conversion of entangled photons. In 2012 Conference on Lasers and Electro-Optics (CLEO), page 1.

[33] Kok, P., Munro, W. J., Nemoto, K., Ralph, T. C., Dowling, J. P., and Milburn, G. J. (2007). Linear optical quantum computing with photonic qubits. Rev. Mod. Phys., 79:135.

[34] Kosaka, H. (2011). Photon-to-electron quantum information transfer. Journal of Applied Physics, 109(10).

[35] Kosaka, H., Inagaki, T., Rikitake, Y., Imamura, H., Mitsumori, Y., and Edamatsu, K. (2009). Spin state tomography of optically injected electrons in a semiconductor. Nature, 457(7230):702.

[36] Kouwenhoven, L., Marcus, C., McEuen, P., Tarucha, S., Westervelt, R., and Wingreen, N. (1997). Mesoscopic Electron Transport. Plenum, New York.

[37] Kouwenhoven, L. P., Austing, D. G., and Tarucha, S. (2001). Few-electron quantum dots. Reports on Progress in Physics, 64(6):701.

[38] Kwiat, P. G., Mattle, K., Weinfurter, H., Zeilinger, A., Sergienko, A. V., and Shih, Y. (1995). New high-intensity source of polarization-entangled photon pairs. Phys. Rev. Lett., 75:4337.

[39] Li, R., Hudson, F. E., Dzurak, A. S., and Hamilton, A. R. (2013). Single hole transport in a silicon metal-oxide-semiconductor quantum dot. Applied Physics Letters, 103(16).

[40] Lütkenhaus, N., Calsamiglia, J., and Suominen, K.-A. (1999). Bell measurements for teleportation. Phys. Rev. A, 59:3295.

[41] Ma, X.-S., Herbst, T., Scheidl, T., Wang, D., Kropatschek, S., Naylor, W., Wittmann, B., Mech, A., Kofler, J., Anisimova, E., Makarov, V., Jennewein, T., Ursin, R., and Zeilinger, A. (2012a). Quantum teleportation over 143 kilometres using active feed-forward. Nature, 489(7415):269.

[42] Ma, X.-S., Herbst, T., Scheidl, T., Wang, D., Kropatschek, S., Naylor, W., Wittmann, B., Mech, A., Kofler, J., Anisimova, E., Makarov, V., Jennewein, T., Ursin, R., and Zeilinger, A. (2012b). Quantum teleportation over 143 kilometres using active feed-forward. Nature, 489(7415):269.

[43] Mani, R. G. (2005). Radiation-induced oscillatory magnetoresistance in a tilted magnetic field in gaas/al$_x$ga$_{1-x}$as devices. Phys. Rev. B, 72:075327.

[44] Mani, R. G., Smet, J. H., von Klitzing, K., Narayanamurti, V., Johnson, W. B., and Umansky, V. (2002). Zero-resistance states induced by electromagnetic-wave excitation in GaAs/AlGaAs heterostructures. Nature, 420(6916):646.

[45] Marcikic, I., de Riedmatten, H., Tittel, W., Scarani, V., Zbinden, H., and Gisin, N. (2002). Time-bin entangled qubits for quantum communication created by femtosecond pulses. Phys. Rev. A, 66:062308.

[46] Medford, J., Beil, J., Taylor, J. M., Rashba, E. I., Lu, H., Gossard, A. C., and Marcus, C. M. (2013). The resonant exchange qubit. Physical Review Letters, 111(5). arXiv:1304.3413.

[47] Natarajan, C. M., Tanner, M. G., and Hadfield, R. H. (2012). Superconducting nanowire single-photon detectors: physics and applications. Superconductor Science and Technology, 25(6):063001.

[48] Nowack, K. C., Koppens, F. H. L., Nazarov, Y. V., and Vandersypen, L. M. K. (2007). Coherent control of a single electron spin with electric fields. Science, 318(5855):1430.

[49] Petersson, K. D., McFaul, L. W., Schroer, M. D., Jung, M., Taylor, J. M., Houck, A. A., and Petta, J. R. (2012). Circuit quantum electrodynamics with a spin qubit. arXiv:1205.6767.

[50] Poole, P., Aers, G., Kam, A., Dalacu, D., Studenikin, S., and Williams, R. (2008). Selective growth of inp/ingaas <010> ridges: Physical and optical characterization. Journal of Crystal Growth, 310(6):1069.

[51] Saeedi, K., Simmons, S., Salvail, J. Z., Dluhy, P., Riemann, H., Abrosimov, N. V., Becker, P., Pohl, H.-J., Morton, J. J. L., and Thewalt, M. L. W. (2013). Room-temperature quantum bit storage exceeding 39 minutes using ionized donors in silicon-28. Science, 342(6160):830.

[52] Simon, C., Afzelius, M., Appel, J., Boyer de la Giroday, A., Dewhurst, S. J., Gisin, N., Hu, C. Y., Jelezko, F., Krll, S., Mller, J. H., Nunn, J., Polzik, E. S., Rarity, J. G., De Riedmatten, H., Rosenfeld, W., Shields, A. J., Skld, N., Stevenson, R. M., Thew, R., Walmsley, I. A., Weber, M. C., Weinfurter, H., Wrachtrup, J., and Young, R. J. (2010). Quantum memories. The European Physical Journal D, 58(1):1–22.

[53] Sinclair, N., Saglamyurek, E., Mallahzadeh, H., Slater, J. A., George, M., Ricken, R., Hedges, M. P., Oblak, D., Simon, C., Sohler, W., and Tittel, W. (2013). Spectral multiplexing for scalable quantum photonics using an atomic frequency comb quantum memory and feed-forward control. arXiv:1309.3202. arXiv: 1309.3202.

[54] Studenikin, S. A., Coleridge, P. T., Ahmed, N., Poole, P. J., and Sachrajda, A. (2003). Experimental study of weak antilocalization effects in a high-mobility $in_x ga_{1-x}$As/InP quantum well. Phys. Rev. B, 68:035317.

[55] Studenikin, S. A., Thorgrimson, J., Aers, G. C., Kam, A., Zawadzki, P., Wasilewski, Z. R., Bogan, A., and Sachrajda, A. S. (2012). Enhanced charge detection of spin qubit readout via an intermediate state. Applied Physics Letters, 101(23).

[56] Takahashi, S., Deacon, R. S., Oiwa, A., Shibata, K., Hirakawa, K., and Tarucha, S. (2013). Electrically tunable three-dimensional g-factor anisotropy in single inas self-assembled quantum dots. Phys. Rev. B, 87:161302.

[57] van der Wiel, W. G., De Franceschi, S., Elzerman, J. M., Fujisawa, T., Tarucha, S., and Kouwenhoven, L. P. (2002). Electron transport through double quantum dots. Rev. Mod. Phys., 75:1.

[58] Warburton, R. J. (2013). Single spins in self-assembled quantum dots. Nature Materials, 12(6):483.

[59] Wootters, W. K. and Zurek, W. H. (1982). A single quantum cannot be cloned. Nature, 299:802.

[60] Yang, C. L., Du, R. R., Pfeiffer, L. N., and West, K. W. (2006). Influence of a parallel magnetic field on the microwave photoconductivity in a high-mobility two-dimensional electron system. Phys. Rev. B, 74:045315.

[61] Yokoshi, N., Imamura, H., and Kosaka, H. (2010). Proposal of a full bell state analyzer for spin qubits in a double quantum dot. Phys. Rev. B, 81:161305.

[62] Yuan, Z.-S., Chen, Y.-A., Zhao, B., Chen, S., Schmiedmayer, J., and Pan, J.-W. (2008a). Experimental demonstration of a BDCZ quantum repeater node. Nature, 454:1098.

[63] Yuan, Z.-S., Chen, Y.-A., Zhao, B., Chen, S., Schmiedmayer, J., and Pan, J.-W. (2008b). Experimental demonstration of a BDCZ quantum repeater node. Nature, 454(7208):1098.

[64] Yugova, I. A., Greilich, A., Yakovlev, D. R., Kiselev, A. A., Bayer, M., Petrov, V. V., Dolgikh, Y. K., Reuter, D., and Wieck, A. D. (2007). Universal behavior of the electron g factor in GaAs/Al$_x$Ga$_{1-x}$As quantum wells. Phys. Rev. B, 75:245302.

[65] Zaidi, H. A. and van Loock, P. (2013). Beating the one-half limit of ancilla-free linear optics bell measurements. arXiv:1301.2749. Phys. Rev. Lett. 110, 260501 (2013).

[66] Żukowski, M., Zeilinger, A., Horne, M. A., and Ekert, A. K. (1993). event-ready-detectors bell experiment via entanglement swapping. Phys. Rev. Lett., 71:4287.